Master thesis and internship[BR]- Master's thesis : Numerical simulations of non-destructive testing procedure by shearography and thermography[BR]- Integration internship

Auteur : Saint-Mard, Nicolas
Promoteur(s) : Noels, Ludovic
Faculté : Faculté des Sciences appliquées
Diplôme : Master en ingénieur civil en aérospatiale, à finalité spécialisée en "aerospace engineering"
Année académique : 2020-2021
URI/URL : http://hdl.handle.net/2268.2/11520

**University of Liège -
School of Engineering
and Computer Science**

Numerical simulations of non-destructive testing procedure by shearography and thermography

SAINT-MARD Nicolas

Master's thesis carried out to obtain the degree of Master of Science in aerospace Engineering by SAINT-MARD Nicolas

Internship supervisor: HOFFAIT Sébastien
Academic supervisor: NOELS Ludovic
External supervisor: GEORGES Marc (CSL)

V₂i

OPTRION
Non-Destructive Testing Solution
for Composite Materials and Structures
SHEAROGRAPHY NDT SYSTEMS

Liège Belgium - Academic year 2020-2021

Acknowledgment

Abstract

The intrinsic structure of composites can lead to defects decreasing their reliability and their in-mission security. Numerical simulations aiming to improve and support defect detection are envisaged in this work. More precisely, shearography and thermography as non-destructive detection methods are being modeled here. Two defect types are considered: delamination and porosity. Detection is investigated with external thermal excitation, leading to thermal and mechanical analysis in simulations.

Firstly, an overview of composites, their defects and non-destructive techniques is addressed. Secondly, prerequisites for simulations like governing equations and assumptions made, the heater characterization, and the numerical scheme used for the transient thermal problem resolution are exposed. Then, defect numerical models are constructed and studied. Delamination and porosity are the two types of defects considered. Numerical models for the delamination covered true delamination and artificial delamination like the physic insert and flat bottom hole models. The porosity model is represented by a few flat bottom holes localized in a small region. Finally, an experimental approach compared with numerical results is used as a validation method.

Different delamination models are developed and they show pretty well concordances between them, except for the Teflon layer (type of physic insert) model for which the mechanical response was not expected or at least, suggests a further study to determine its validity. The porosity model showed difficulties in this kind of defect detection. Finally, the experimental approach enabled to see that numerical and experimental results were similar but that some efforts on parameter updating remain to be made. Mainly the characterization of the lamp that irradiates a highly non-homogeneous flux.

Contents

Nomenclature

Abbreviations

CCD	Charge-coupled device
CFRP	Carbon fibres reinforced polymer
CLT	Classical laminate theory
CMOS	Complementary metal-oxide-semiconductor
CNR	Contrast to noise ratio
CPU	Central processing unit
DFT	Discrete Fourier transform
EOF	Empirical orthogonal function
FBH	Flat bottom hole
NDT	Non-destructive testing
PPT	Pulsed phase thermography
PTFE	polytetrafluoroethylene
SVD	Singular value decomposition
UD	Unidimensional fibres arrangement

Symbols

α	Thermal expansion coefficient	[K^{-1}]
α_t	Thermal diffusivity	[m^2/s]
$\boldsymbol{e}_x$	Unit vector in "x" direction	
$\boldsymbol{e}_y$	Unit vector in "y" direction	
$\boldsymbol{e}_z$	Unit vector in "z" direction	
$\boldsymbol{k}_s$	Sensitivity vector	
δx	Shearing in "x" direction	[m]
Δ	Light relative phase change	[rad]
Δ_x	Light relative phase change for a shear in "x" direction	[rad]
ϵ	Emissivity	[-]
λ	Wavelength	[m]

μ	Contrast	
μ	Dynamic viscosity	[N s/m^2]
ν	Poisson's coefficient	[-]
ϕ	Light relative phase	[rad]
ψ	Fibre orientation	[°]
ρ	Density	[kg/m^3]
$\sigma_{\text{S-B}}$	Stefon-Boltzmann constant	[W/(m^2 K^4)]
σ_{ij}	Stress tensor components	[Mpa]
θ	Light field phase	[rad]
ε_{ij}	Deformation tensor components	[-]
a	Light field amplitude	
c_p	Specific heat capacity	[J/(kg K)]
C_{ijkl}	Stiffness tensor components	[Mpa]
D	Flexural stiffness	[kg·m^2/s^2]
dt	Time step	[s]
E	Light field	
E	Young modulus	[Mpa]
E_b	Black body emissive power	[W/m^2]
f	Frequency	[Hz]
F_{ij}	View factor	[-]
G	Shear modulus	[Mpa]
g	gravitational constant	[m/s^2]
G_{r_L}	Grashof number	[-]
h	Convection coefficient	[W/(m^2 K)]
h_r	Radiation coefficient	[W/(m^2 K)]
I	Light intensity	
I_0	Light average intensity	
K	Bulk modulus	[Mpa]
k	Thermal conductivity	[W/ (m K)]

k'	Thermal gluing	[W/(m^2 K)]	t_d	Defect depth	[m or mm]
k_f	Fluid thermal conductivity	[W/ (m K)]	t_M	Mechanical characteristic time	[s]
Nu	Nusselt number	[-]	t_M	Mechanical problem characteristic time	[s]
p	Pressure	[Pa]	t_T	Thermal problem characteristic time	[s]
P_h	Heater electric power	[W]	u	Displacement in "x" direction	[m]
Pr	Prandtl number	[-]	u_{ij}	Displacement vector components	[m]
q''	Heat flux	[W/m^2]	V	Volume	[m^3]
R	Ideal gas constant	[J/(kg K)]	v	Displacement in "y" direction	[m]
Ra	Rayleigh number	[-]	w	Displacement in "z" direction	[m]
S	Surface area	[m^2]	C	Thermal contrast	[°C]
T	Temperature	[K]	TPE	Total potential energy	[J]

1 _____ Introduction

In the aerospace engineering industry, not only the use but also the need for composite materials is constantly increasing. More and more, lighter and more resistant composites are developed and replace metallic materials that are still massively used in the aerospace sector. Composites are a combination of two or more materials in view of obtaining a material with better properties. It makes them very promising materials for the development of new applications and missions. By contrast, manufacturing processes enabling the fabrication of these composite materials may introduce defects. In addition, the intrinsic nature of composites might also lead to the formation of defects during their service life, defects that do not exist in metals, for instance.

In the scope of material engineering, ensuring good reliability and durability throughout the materials service life is essential. It follows that the characterization and the detection of defects that may affect the composites' structure become imperative. To this purpose, destructive and non-destructive tests are lead by manufacturers to ensure the good quality of the end product. Improvement of defect detection is the aim of this work. More particularly, improvement of two non-destructive methods that are shearography and thermography.

Shearography is a laser interferometry technique for surface deformation measurements. On the other side, thermography is a technique based on infrared image acquisition of a heated object surface. In both techniques, the object is thermally stimulated with an external heater. Their non-contact and full-field measurement capabilities are used for non-destructive defect detection ([1] and [2]). In practice, to improve the measurement, numerical simulations aiming to reproduce the tests made in labs are conducted. Usually, improvement of experimental methods is made by studying experimentally known and straightforward cases. Numerical studies may bring a new tool to the understanding of these cases. The final purpose is to create models serving as a basis for experimental detecting improvement. In the end, the construction of reliable models will allow the defect detection prediction. This work is part of the work context realized at Optrion (a subsidiary company of V2i), such as the development of shearo and thermo camera, "LDCOMP" research project, etc.

At first, a review of composite materials and the principle of non-destructive techniques covered in this work will be discussed. Then, prerequisites to numerical simulations like governing equations, external factors estimation and numerical tools will be developed. Next, numerical models representing two often encountered defects such as delamination and porosity will be examined under different conditions. Results will be discussed and the difference between models and conditions will be highlighted, especially for the delamination models, where different models

are investigated: true delamination, physic insert and flat bottom hole. Regarding the porosity model, one model only will be constructed and different heating conditions will be studied and compared. Finally, the experimental approach will be envisaged not only as a validation of simulations but particularly as a resource for numerical models improvement. The numerical simulations and experimental results have to be analyzed in parallel. This is the combination of both that enables the construction of reliable numerical models to, in the end, be able to improve non-destructive tests.

The outcomes obtained at the end of the work show that numerical models are quite representative of what is observed experimentally. However, the physical insert as a delamination model shows unexpected behavior in shearography and would need a more thorough study. Furthermore, an effort on estimation and characterization of some external parameters, mainly the flux distribution emitted by the heater, is still to be done.

Works investigating numerical models for delamination models have already been realized in [3], [4] and [5]. Models of the true delamination, the physic inset and the flat bottom hole are studied. Results obtained in this work are similar to the ones in this work. They show pretty close results for the physic insert model, which opens a reflection process on this model.

2 Composites, defects & detection review

Non-destructive testing (NDT) techniques are more and more used in many industries as the need for defect detection in composite materials constantly increases. Mainly in the aerospace field, the use of composites such as Carbon fibres reinforced polymer (CFRP) has increased a lot since 2010 [6]. This type of material is subjected to the apparition of defects (that do not exist in metallic materials, for instance), leading to a significant performance decrease. Identification of defects is, therefore, the stake of NDT. Among all of the NDT techniques, this work focuses on imaging ones, more precisely shearography and thermography. Depending on the defect, one or another technique will be preferred. The ultrasound method is by far the most used non-destructive inspection because it is very sensitive to delamination, debond and porosity defects which are the main defects in composites. However, ultrasound techniques are out-of-scope of this work. A review of the composite materials and the defects that may occur is carried out before explaining the two non-destructive testing techniques, which are shearography and thermography.

1 Composites materials

Information given in this section is based on [6], [7], [8], [9], [10] and [11].

Nowadays, composite materials are found in many different domains from sports to automotive, space or again aeronautic fields. A composite material is basically any combination of two or more materials, although it refers to a matrix reinforced with fibres in engineering. For instance, in nature, bones and wood are natural composites, but it will refer to fibres embedded in a matrix when talking of composites in this report. Fundamentally, the matrix plays three roles: it holds and protects fibres, and transmits loads to them while fibres sustain mechanical loads.

Composites are generally light and exhibit excellent mechanical properties. Furthermore, they might be resistant to corrosion, show excellent fatigue resistance and some other advantages. Industrially, they are used where specific applications cannot be achieved with classic materials. Typically, when weight, stiffness and strength optimization are required, which is very often the case in aeronautic and space fields. On the other hand, costs (manufacturing, maintenance, repair, etc.) are usually high, they are brittle and damage issues may appear. Because of their brittleness and damage issues, security could be a drawback compared, for example to aluminum alloys.

1.1 Matrix

The three main classes of the matrix are polymeric, metallic and ceramic. Epoxy resin, a polymer matrix, is probably the most frequent matrix for composites in engineering. However, metallic (for instance, aluminum or magnesium) and ceramic (such as glass, carbon or silicon) are

also present in the industry. In a polymer matrix, thermoset resins (epoxy, etc.) and thermoplastic polymers (PVC, etc.) are encountered. Thermoset resins cure with heat, meaning that once heated, they cannot come back to a more viscous state, while thermoplastic polymers see their viscosity decrease with heat.

As already said, the matrix is a support for reinforcements fibres. It keeps fibres aligned and bonds them together (it acts like an adhesive). On top of that, the matrix generally has a low density and exhibits good shear properties. The matrix stabilizes buckling modes because fibres are relatively long to some extent and then easily subjected to buckling. It also helps the composite withstand compression as fibres have very low compression modulus (just like strings). Therefore keeping them aligned and oriented increases the compression resistance.

1.2   Fibres

Like the matrix, fibres can be classified into three main families: polymeric, metallic and ceramic[1]. In aerospace engineering, glass, aramid and carbon fibres are the most encountered fibres. When high service temperatures are faced, boron fibres can also be frequent. Besides, fibres can be continuous (very long), long or short and arrange in many ways. Different lengths of fibres provide different properties.

- **Continuous fibres** have a very high length over diameter ratio (as well as a strength to weight ratio).

- **Long fibres** are typically fibres with a length of the order of magnitude from some centimeters to some decimeters.

- fibres are called **Short fibres** when their length is about a few millimeters

Fibres arrangements are diverse and lead to varying properties. Some of these arrangements are shown in Fig. 2.1. In the scope of this report, mainly UD and woven fabric will be considered. A complete description of advanced fibres structures may be found in [8] for the reader who would like more information.

1.3   Structural arrangement

Matrix and fibres are the base constituents of composites. They can be arranged in different ways to build full structural laminates. The two main ways are called the laminate and sandwich structures. More often, laminate composite structures are available for testing but sandwich structures are sometimes tested too. Nevertheless, both of them are described even though simulations in this work will only cover laminate models.

---

[1]Natural fibres also exist but are not considered here.

(a) Unidimensional (UD) [12]

(b) Bi-directional or woven fabric [13]

(c) Multi-directional or braided fibres [6]

(d) Random or discontinuous fibres [6]
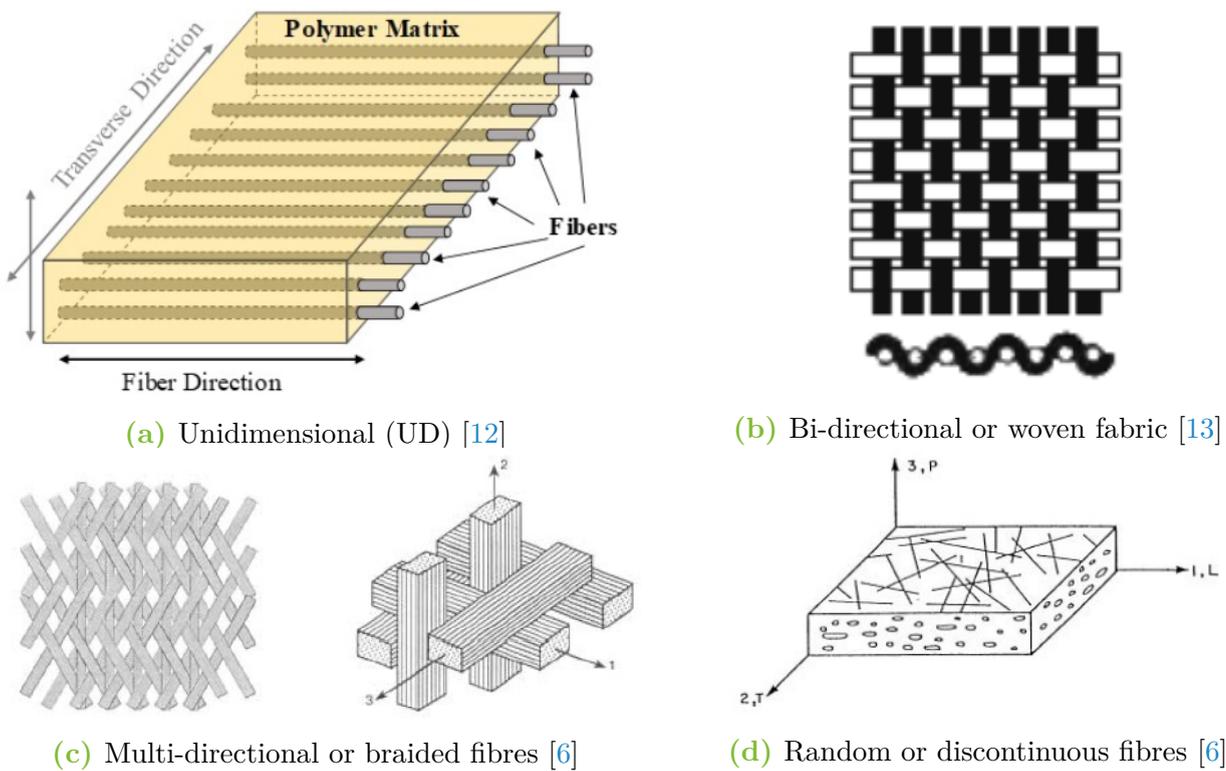
Figure 2.1: fibres arrangement.

1. **Laminates composite** is a structure where a flat arrangement of fibres (usually UD or woven architecture) and matrix, called plies, are stacked to form a complete laminate. In the case of a UD ply, fibres are all aligned in the same direction and properties are considered orthotropic. Properties in fibres direction are higher than in the transverse directions (there are two transverse directions as fibres are all aligned in one direction). With woven fabric, a ply contains fibres in two directions and so, have only one transverse direction. Afterward, plies with different fibre orientations are stacked in order to compose the laminate. An example of stacking, accounting for UD plies, is provided in Fig. 2.2. The stacking sequence is given by the succession of orientations from the bottom to the top plies. For instance, the sequence [0/90] represents a laminate with the bottom ply containing fibers at 0° and the top ply fibres at 90°. When a sequence is repeated, an index is added such as $[0/90]_2$ represents a laminate with 0,90,0,90° plies (still bottom to top). For symmetric case, the subscript "s" is used: $[0/90]_s$ stands for a sequence of 0,90,90,0° plies.

Due to the different fibre orientations, coupling modes appear in laminates. Some coupling effects might be avoided with specific stacking sequences.

    i **Symmetric laminates** (i.e. symmetric stacking sequence) will automatically lead to cancellation of in- and out-of-plane effects. For instance, between tension and bending effects or tension and torsion.

    ii **Balanced laminates** avoid coupling between tension and shear modes. In fact, this

is the definition of balanced laminate and different stacking sequences may lead to it. Firstly, a symmetric stacking sequence leads to a balanced laminate. Secondly, any sequence containing only plies at 0 and 90 degrees. Thirdly, if the sequence contains the same proportion of plies at $\pm\psi$. Additional plies at 0 and 90°may be in the sequence. In fact, they do not impact the balance of the laminates.
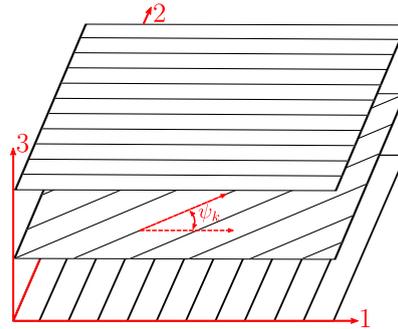
Figure 2.2: Schematic of plies stacking with different orientations considering UD fibres.

2. **Sandwich composites**: are obtained by combining two thin and strong skins with thick and light core materials as illustrated in Fig. 2.3. Faces are typically high-strength composites and the common core are honeycomb structures, foam and wood. In aerospace engineering, honeycomb is manufactured with aluminum and Nomex (a kind of aramid). Sandwich structures are lighter and present higher bending stiffness than laminates composites. They are also less expensive, thermal insulators and finally enable vibrations damping. By contrast this kind of structure is less resistant in traction or compression and is more adapted for impact applications (L. Noels, private communication, June 2021). More information on the material used in different parts of the structures and the manufacturing processes are developed in [11].
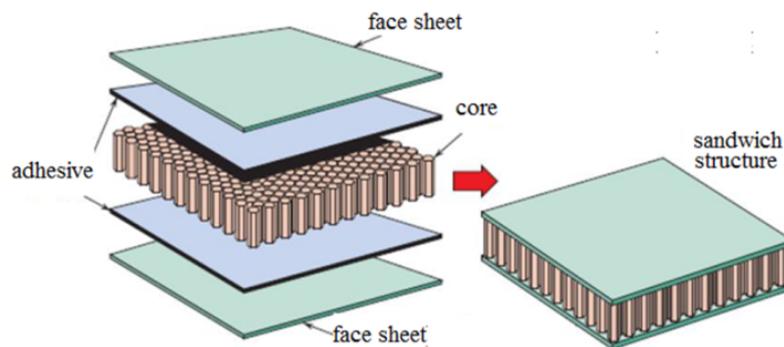
Figure 2.3: Example of a sandwich structure with the core in honeycomb (taken from [14]).

2 Defects in composites

Works in [15] and [16] form the basis for this section.

Mainly, defects may appear in two ways, either during the manufacturing process or in the material's service life. For instance, porosity and debond occur during the manufacturing process, while delimitation refers to the separation of composites layers due to loading during the service life. In fact, debond and delamination are comparable because for both, the problem occurs at the inter-laminar level (at the interface of two plies). Note that in sandwich structures, debond occurs not at the interface of plies but at the interface between the adhesive layer and the skin layer or between core and adhesive. Some defects like fibres misalignment and waviness may arise following the manufacturing process, however, these defects are not examined here. Bad cure parameters may lead to the formation of porosity and in practice, it is almost inevitable. Delamination, debond and porosity are the defects treated in this work. They can decrease the material performance that is the reason why their detection is crucial.

2.1 Delamination and debond

Among mechanical failures, delamination and debond are the most observed failure modes in composites. On the one hand, both terms refer to a defect at the layer interfaces. On the other hand, their origin and their intrinsic nature are not the same. The term delamination applies to a separation of layers in laminates under influence of loading during the service life as shown in Fig. 2.4. Typically, delamination may emerge after impacts. Whereas, debond is an unintentional separation in the adhesive linking to plies occurring during the manufacturing process. Fig. 2.5 provides an illustration of a debond defect.
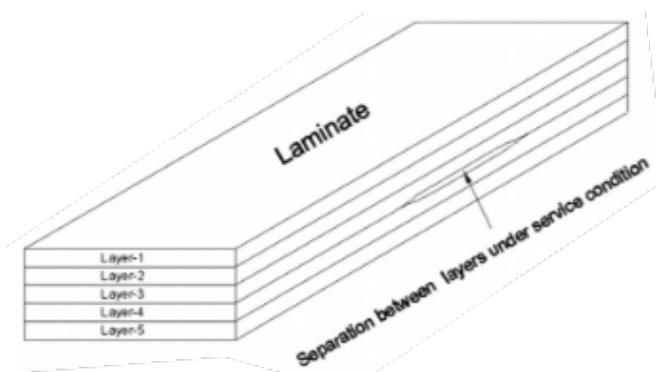
Figure 2.4: Delamination [15].
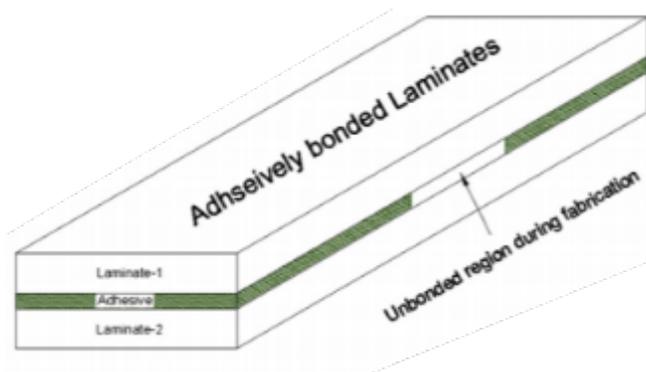
Figure 2.5: Debond [15].

2.2 Porosity

Porosity (small voids in the material) is the most common defect found in composites and occurs during the manufacturing process. Achieving zero porosity is very difficult, however, some fabrication processes are better than others (not described here). Cure parameters such as duration, temperature, pressure, or vacuum bleeding of resin are factors impacting the amount of porosity. An example of porosity within the composite is shown in Fig. 2.6.
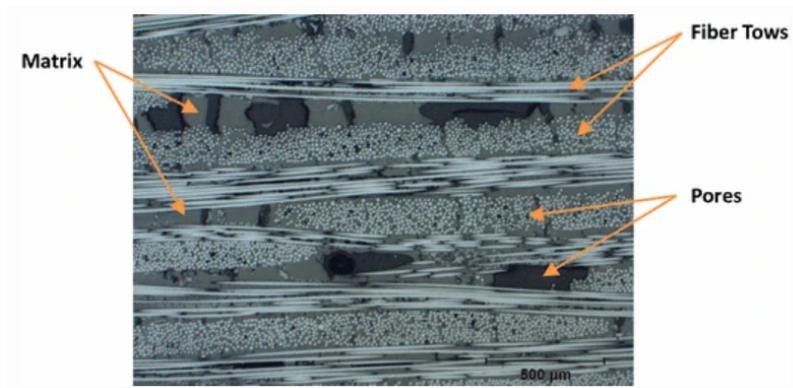
Figure 2.6: Picture of porosity in composites taken from [17].

As porosity may significantly affect material properties, detecting techniques are developed in the industry. The ultrasound method is very effective in detecting porosity inside laminates, but this work focuses on infrared thermography and shearography. In fact, only thermography will be used for porosity, shearography is usually bad adapted ([18]).

2.3 NDT techniques, an intuitive comprehension

Before going into the techniques addressed in this report, comprehension of the physical effect involved in the techniques must be achieved.

Whether in thermography or in shearography, the tested composite (also called sample or object) will be submitted to a thermal excitation via an infra-red lamp. Locally, a defect will change the thermal conductivity of the material. Indeed, delamination, debond or porosity are discontinuities in the material. Imagine an air layer inside a material, the air has different properties than the composites. When the object is heated, the temperature diffuses by conduction through the thickness. When the temperature gradient reaches the defect, the thermal flux is blocked and the temperature will accumulate above the defect. Inspecting the surface with a thermal camera could reveal a hot zone above the defect and thus lead to defect detection.

In shearography, the temperature is not inspected but this effect of higher temperature will lead to locally higher deformation. It is illustrated in Fig. 2.7, where the deformation occurs in the z direction. It will be seen in the next section that shearography is in a certain way sensitive to displacement along z and can then lead to defect detection. Note that this behavior of deformation can be reached with other external simulations like making the void, mechanical loads, etc. but these are not considered here.

The position of the defect is very impacting as if the defect is far from the surface, the localized effect of higher temperature decreases. The size is another impacting factor, especially in shearography. For instance, porosity is more challenging to detect in shearography because of the small size of pores. In comparison, delamination may lead to a bigger defect size.
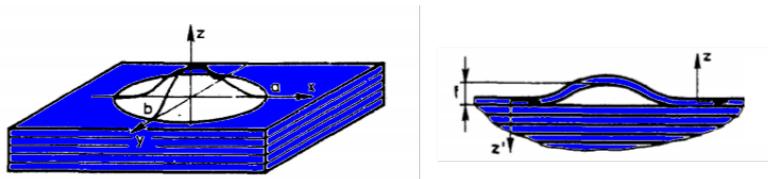
Figure 2.7: Defect deformation due to thermal loads. The image at the right is a cutting view of the left image. (from [19])

3 Shearography

Using coherent light (lasers), this optical method is often used to detect delamination or debond. Indeed, it provides knowledge on displacement variations. It has been seen that out-of-plane displacements are the main concern (see section 2.3) when identifying delamination and that shearography is very sensitive to their variation. Shearography takes advantage of speckle pattern (see section 3.1) to highlight the change in displacements by making the speckles interfere with their copy beforehand sheared by an optical device (i.g. Michelson interferometer).

3.1 Speckles applied to shearography

Before explaining the principle of shearography in the next section, it is necessary to understand what a speckle pattern is and how it is formed.

Speckles are the result of observing the reflection of coherent light on an optically rough surface[2], an example of a speckle pattern is shown in Fig. 2.8. In practice in shearography, the observation is done using an image sensor such as a charge-coupled device (CCD) or a complementary metal-oxide-semiconductor (CMOS) sensor. The image sensor records the illumination intensity, I, that it perceives and displays a gray pixel. Depending on the intensity, the pixel is black for the smallest intensities and white for the highest ones. The intensity varies on the image plane (i.e. plane where the image is recorded) due to the interference of the scattering of the coherent light on the rough surface, leading to a speckle pattern (Fig. 2.8).

This specific feature is used in shearography but a raw speckle pattern does not provide any information. The next sections will treat how this feature is managed to obtain key information.

3.2 Principle

To obtain out-of-plane displacement derivative from speckles some treatment may be needed. The link is not straightforward, so the process is described step by step based on Fig. 2.9. For convenience and simplicity, the procedure is only explained and represented using two reference points on the object (points 1 and 2 in Fig. 2.9).

---

[2]A surface for which the variations of the surface's relief are of the order of the light wavelength [20].
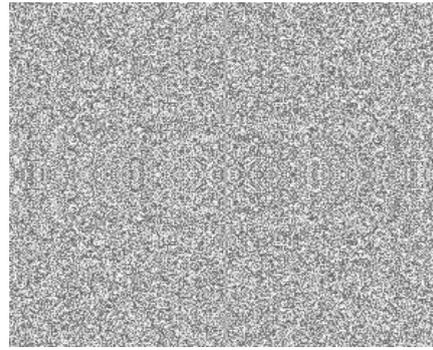
Figure 2.8: Typical speckle pattern of a plate illuminated by coherent light (generated randomly in `Matlab`).
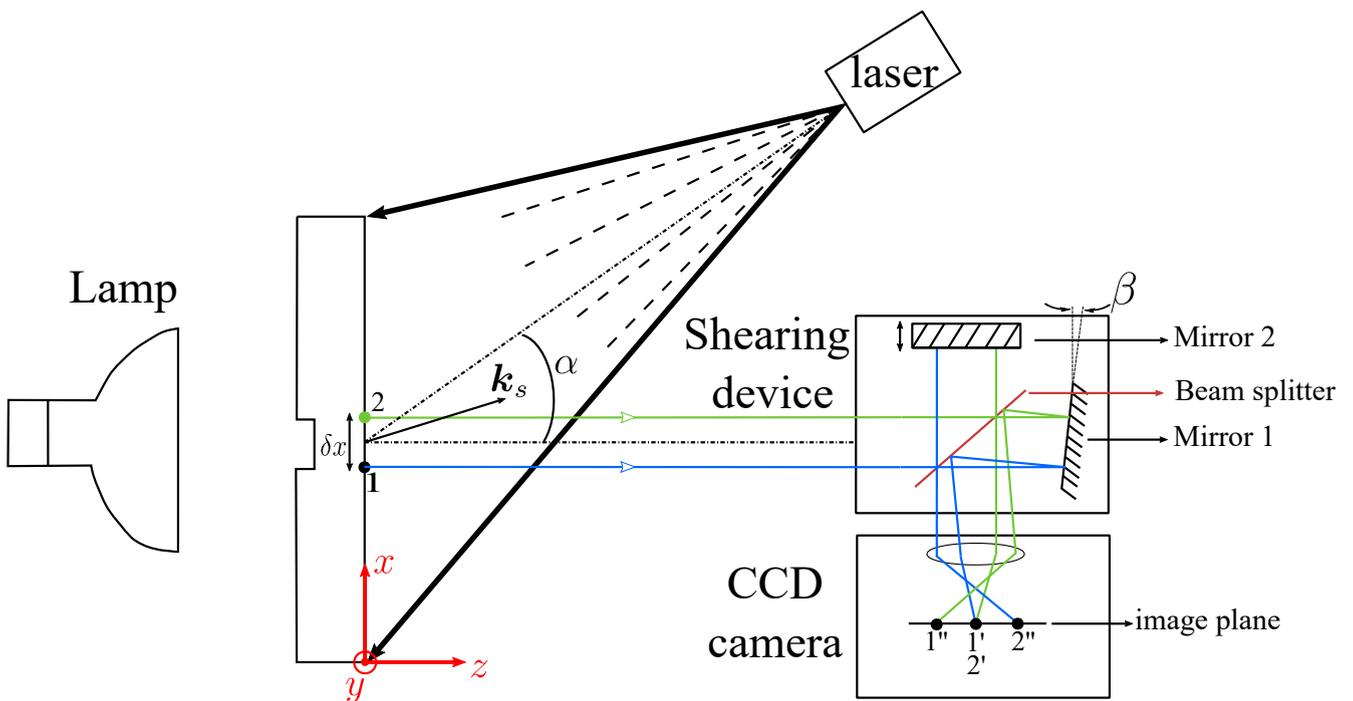
Figure 2.9: Schematic of a shearographic set-up. The shearing device is schematically represented by a Michelson interferometer [3].

3.2.1 Step 1: unstressed object

This step is used as a reference during which the object is at rest without any external excitation being applied.

The object is illuminated by a laser light that is reflected by this object. The light passes through the shearing device and is then focused on the image plane of the CCD camera. The light from a point on the object is mapped onto two points on the image plane thanks to the shearing device[3]. It is illustrated in Fig. 2.9, where, point 1 is mapped onto points 1′ and 1″, and point 2

---

[3] The shearing device principle is not described in detail as it is not the main concern. However, note that in Fig. 2.9, the represented shearing device is a Michelson interferometer although other shearing devices exist. When using a Michelson interferometer, one of the mirrors should be tilted with a slight angle (β in Fig. 2.9) to produce a shear.

is mapped onto points $2'$ and $2''$ on the image plane. By extending this mapping to all points of the object, it comes that the speckle pattern seen in section 3.1 is actually interfering with itself but shifted in space. This shift is called the shear and is represented by δx on the object plane and $\delta x'$ on the image plane[4]. This concept is illustrated in Fig. 2.10 where the shear can clearly be seen, such a figure is called a **shearogram**.
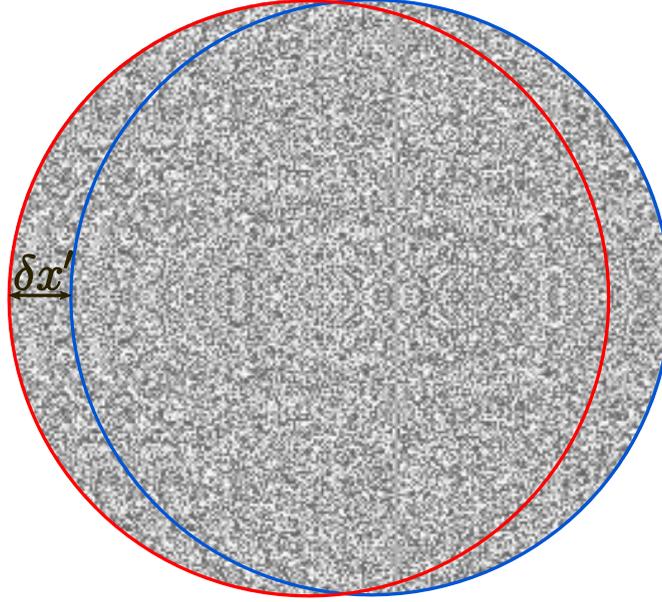
Figure 2.10: Shearogram with shear visualisation (generated randomly in `Matlab`).

According to [21] and [22], the wave fronts of the rays from point 1 and 2 are represented by their respective light field E_1 and E_2 having the following expression,

$$E_1(x,y) = a_1 \cdot e^{i\theta(x,y)} \quad \text{and} \quad E_2(x+\delta x, y) = a_2 \cdot e^{i\theta(x+\delta x, y)}. \tag{2.1}$$

In Eq. 2.1, θ is the phase and depends on the coordinates of the considered point and, a_i is the light amplitude. On the image plane, these two fields interfere at a point $1'$ or $2'$ (being the same point) in Fig. 2.9. The total light field, E_T, at this point is therefore,

$$E_T = E_1 + E_2, \tag{2.2}$$

and the monitored intensity by the camera is expressed as,

$$I = E_T E_T^* = 2I_0(1 + \mu \cos \phi), \tag{2.3}$$

where the symbol, "$*$", denotes the conjugate, I_0 is the average intensity, μ is called the contrast,

---

[4]Shear on the object plane and on the image plane are linked by a proportional relation depending on the set-up.

and ϕ is the relative phase angle. The last three terms are then given by

$$I_0 = \frac{a_1{}^2 + a_2{}^2}{2}, \quad \mu = \frac{2a_1 a_2}{a_1{}^2 + a_2{}^2}, \quad \phi = \theta(x,y) - \theta(x + \delta x, y). \tag{2.4}$$

The general expression in Eq. 2.3 serves as a starting point in a lot of references for developing digital shearography theory ([21],[23],[24]).

3.2.2 Step 2: stressed object

Now the object is subjected to thermal stress using an infrared lamp. Note that this is not the only way to go, but it has the advantage of not introducing physical contact with the object. A displacement field will develop by changing the relative phase of the light intensity field described mathematically by

$$I^\star = 2I_0[1 + \mu\cos(\phi + \Delta)]. \tag{2.5}$$

The symbol, "$\star$", identifies the intensity in the stress configuration and Δ is the relative phase variation due to stresses applied. The quantity, $I^\star$, varies in time as the thermal excitation and therefore the displacement field varies in time as well.

The reference intensity distribution, I in Eq. 2.3, is stored as the reference frame while the intensity distribution, $I^\star$, is stored in frames varying in times. At any times, the digital subtraction pixel by pixel of frames with the reference one leads to a new intensity distribution, I_d, of the form

$$I_d = I - I^\star = 4I_0\mu\left[\sin(\phi + \frac{\Delta}{2})\ \sin(\frac{\Delta}{2})\right]. \tag{2.6}$$

This expression mathematically explains the formation of a fringe pattern observed in experimental shearography. Fringe behaviour depends on the relative phase change, Δ, due to the term $\sin(\frac{\Delta}{2})$ in Eq 2.6. This fringe formation phenomenon can be observed in Fig. 2.11.
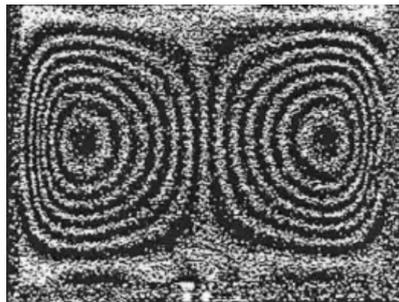
Figure 2.11: Typical fringe pattern issued from [24]. *"Fringe patterns depicting the deflection-derivatives of a rectangular plate clamped along its boundaries and subjected to uniform pressure"*[5].

---

[5][24]

3.2.3 Step 3: relative phase and displacement derivatives

The relative phase change and so the fringes can be linked to displacement derivatives by the following relation,

$$\Delta_x = \left(\frac{\partial u}{\partial x} \boldsymbol{k}_{\mathrm{s}} \cdot \boldsymbol{e}_x + \frac{\partial v}{\partial x} \boldsymbol{k}_{\mathrm{s}} \cdot \boldsymbol{e}_y + \frac{\partial w}{\partial x} \boldsymbol{k}_{\mathrm{s}} \cdot \boldsymbol{e}_z \right) \delta x, \tag{2.7}$$

if the shear is in the x direction (δx). It possible to write an expression similar to Eq. 2.7 for shear in other directions but it is not developed here. In Eq. 2.7, displacements in directions $\boldsymbol{e}_x$, $\boldsymbol{e}_y$ and $\boldsymbol{e}_z$ (being the unity vector in x, y and z direction) are represented by ,u, v and w respectively, $\boldsymbol{k}_s$ is called the sensitivity vector, which is found along the bisector of the angle α representing the angle between the illuminating and viewing direction as can be seen in Fig. 2.9. Its norm can be computed as

$$\|\boldsymbol{k}_s\| = \frac{4\pi}{\lambda} \cos(\frac{\alpha}{2}), \tag{2.8}$$

with λ being the wavelength of the laser light used to illuminate the object. In the case where the illuminating and viewing direction are normal to the object surface, the angle α is equal to zero and the sensitivity vector direction lies along $\boldsymbol{e}_z$, leading to the reduced expression

$$\Delta_x = \frac{4\pi}{\lambda} \frac{\partial w}{\partial x} \delta x. \tag{2.9}$$

This final relation relates the link between the out-of-plane displacement derivative and the relative change of phase due to stress applied on the object. It gives a tool to estimate qualitatively the out-of-plane displacement.

So far, only the intensity described in Eq. 2.6 is recorded by the camera and the relative change of phase, Δ is unknown. Different algorithms and techniques (described in [21], [22], [23] and [24]) exist to obtain this relative phase change. The technique to acquire the phase change is called temporal phase stepping. It involves the recording of successive shearogram shifted in phase. This shift is produced by moving the mirror 2 forward or backward. With a Michelson interferometer as represented in Fig. 2.9, this movement is controlled by a piezoelectric transducer linked to a digital to analog converter. Then, a phase stepping algorithm is performed to obtain what is called the wrapped phase diagram. This phase diagram displays the phase change (Δ) in the interval $[-\pi,\pi]$. Different algorithms are available; the one used later on in experiments is the five-step algorithm. The phase is then calculated with five shifted (each of $\pi/2$) intensity distributions. The phase is obtained by

$$\phi = \tan^{-1} \left(\frac{2(I_2 - I_4)}{2I_3 - I_5 - I_1} \right), \tag{2.10}$$

and the change of phase is then obtained by subtracting the current phase from the reference phase. The full procedure is illustrated in Fig. 2.12.
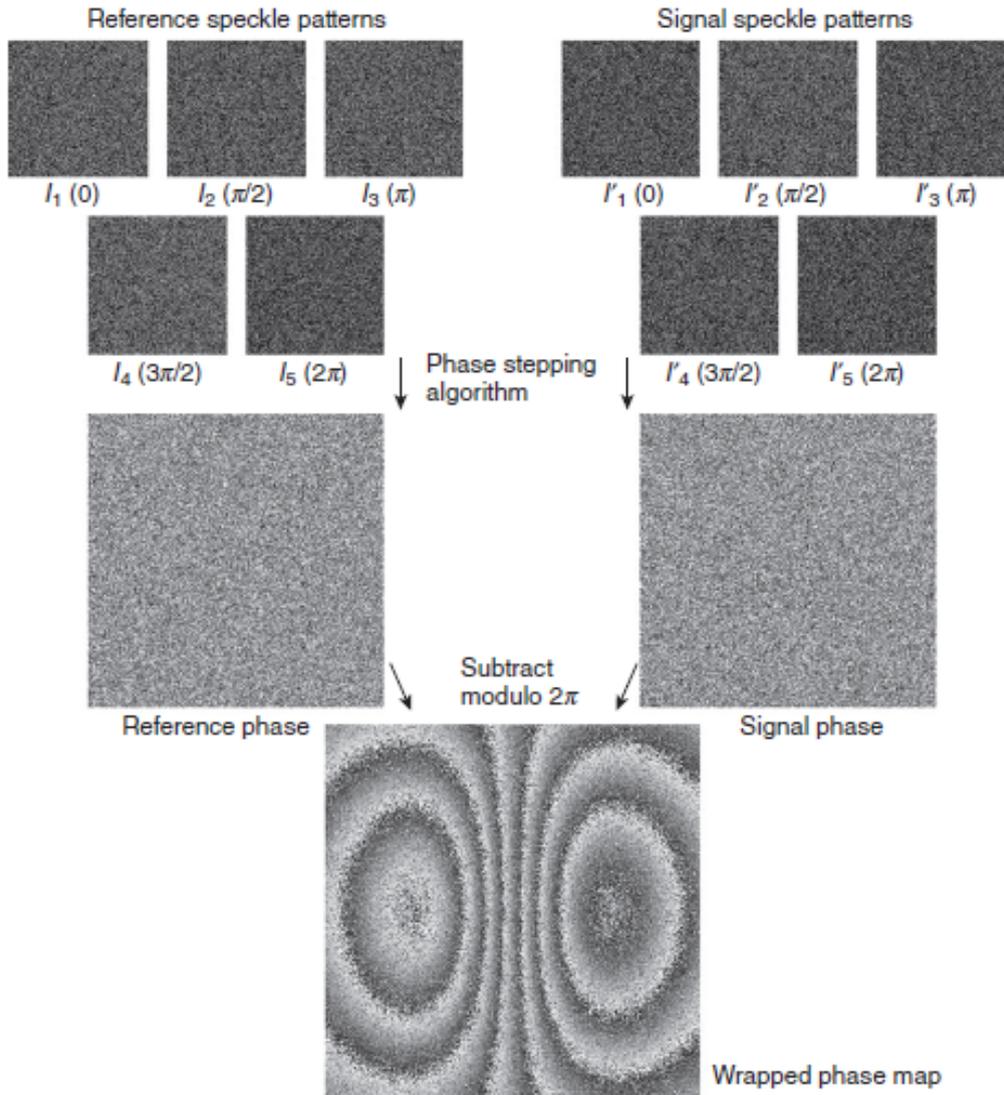
Figure 2.12: Temporal phase stepping algorithms (from [1]).

The important home message is that the relative phase change can be computed and then gives an estimation of the out-of-plane displacement variation.

3.3 Shearography in numerical simulations

To compare experimental and numerical results, the wrapped phase diagram is used. It has been seen in the previous section how obtaining the phase diagram. This section explains how to retrieve the phase diagram in numerical simulations.

The numerical simulations provide the displacement field in each direction. From there, derivatives along x of out-of-plane displacement $(\frac{\partial w}{\partial x})$ are computed. Knowing the shear and the laser wavelength, the phase diagram can be built from Eq. 2.9. Doing so provide in fact, the unwrapped phase diagram. Therefore, the phase is finally numerically wrapped in $[-\pi,\pi]$.

The process could also consist of unwrapping the experimental phase diagram and then in-

tegrating them to recover the displacement field. However, this operation is more tricky. 2D unwrapping algorithms exist but are not always efficient, and the integration is always accurate to within one constant. Note that if boundary conditions are known, it would be possible to obtain, in the end, the full displacement field.

4 Thermography

Another very common NDT technique is infrared thermography. Defects inside materials change their thermal properties locally and the thermal field propagation is therefore impacted. Thermography provides infrared images of this propagation enabling the detection of zones where the defect is located. Different approaches exist differing by the stimulation applied to the object, to quote the approach used in this work, pulsed thermography brings a pulse of energy to the sample. Other methods exist, such as lock-in or step thermography. At first, the contrast method (close to CNR) is exposed. Then, image treatment improving the identification using certain algorithms is investigated. Among images process, pulsed phase thermography and principal component thermography are explained in this section based on [25], [26] and [27].

4.1 Thermal contrast

The thermal contrast, C', is the most simple and most common processing technique. Basically, it is defined as the difference between the temperature at a pixel p and that in a sound zone [25]. Mathematically, it is expressed as

$$C'(t) = T_p(t) - T_s(t) \tag{2.11}$$

where T_p is the temperature at the pixel p and T_s, the temperature in a sound zone. The contrast varies on the image plane but also in time. Actually, a drawback of this definition is that the contrast is very sensitive to the sound zone determination. With an artificial defect, the sound zone definition is straightforward and the contrast is very easy to use.

In practice, only the contrast in the defect zone is analyzed and to take into account the whole defect, an average of the temperature in this zone ($\overline{T}_d$) is performed. The sound zone is sometimes taken at one point or once again an average in a defined zone. In simulations, to avoid this problem of the sound zone determination, its contribution is taken as the mean temperature of the entire image plane ($\overline{T}$). The thermal contrast becomes

$$C(t) = \overline{T}_d(t) - \overline{T}(t). \tag{2.12}$$

In fact, in simulations, the mean temperature of the image is assumed to be equal to the mean temperature in a sound zone. It is very important to note that this last definition is only used for simulation results. When dealing with experimental results, a sound zone is defined to increase

the contrast value due to higher variability coming from noise measurement.

Remark: the apparition of noise in experimental measures is usually taken into account dividing the contrast by the standard deviation difference of the temperatures in the defect and in the sound zone (E. Verstraelen, private communication, April 2021). It is called the contrast to noise ratio (CNR) and is defined as

$$\text{CNR} = \frac{\overline{T}_d(t) - \overline{T}(t)}{0.5\,S(T_d) + 0.5\,S(T)}. \tag{2.13}$$

The standard deviation is denoted by S. Because there is no noise in simulations, this is not usable in the scope of this project. The denominator would just be zero.

4.2 Pulsed phase thermography

Pulsed phase thermography (PPT) uses the discrete Fourier transform (DFT) to emphasize the defect. Basically, the one-dimensional fast Fourier transform (FFT) is applied to the time signal of each pixel of the raw infrared images ([25] & [26]). Considering a pixel p of a sequence of N images with pixels representing the temperature. The temperature at point p is denoted T_p and varies in time. The fast Fourier transform (operator $\mathcal{F}$) is applied to this signal and the general results are expressed as

$$T_p(t) \xleftrightarrow{\mathcal{F}} \mathcal{T}_p(f) = r_p(f) \cdot e^{i \cdot \varphi_p(f)}, \tag{2.14}$$

with r_p the amplitude and φ_p the phase of the complex Fourier transform $\mathcal{T}$. After computation of the FFT, the signal is then represented in the frequency domain with its associated variable f. Eventually, the phase information is inspected for defect identification. A schematic of the algorithm can be seen in Fig. 2.13.
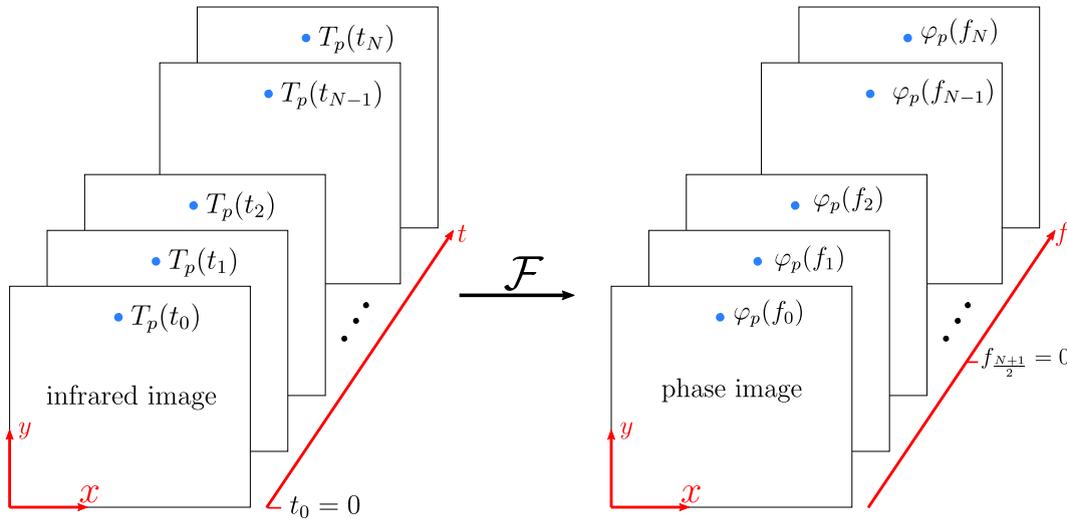
Figure 2.13: Schematic of the FFT alogrithm applied in the scope of pulsed phase thermography.

the benefit of this technique is that the defect depth can be linked to the phase and the

frequency. From the semi-infinite body submitted to periodical uniform heat source of frequency f, the phase is linked to the depth (t_d) by ([28])

$$z = \sqrt{\frac{\alpha}{\pi f}} \cdot \varphi, \tag{2.15}$$

where the symbol α_{th} stands for the thermal diffusivity.

In this method, data is actually projected onto a set of orthogonal basis functions that are oscillatory (Fourier transform implies imaginary exponential functions). Although it works very well with oscillatory signals, when it comes to pulsed phase thermography, it may not use the more appropriate basis ([27]). Indeed, the temperature response to a pulse is likely to be monotonic, therefore, another technique is investigated in the next section.

4.3 Principal component thermography

As the pulsed phase thermography does not use the more appropriate basis, this method relies on empirical orthogonal functions (EOFs). It implies a singular value decomposition (SVD) of the data to construct a set of orthogonal statistical modes. For the SVD to be applicable, data must be represented by a 2D matrix but the transient thermal problem is generally stored in 3 dimension matrices, the first two dimensions for the space and the third one for the time. The first step consists of compacting this matrix so that space variations are re-arranged to vary along the rows and the time along with the columns. Considering the same time sequence of images as depicted on the left in Fig. 2.13, data are contained in a re-arranged 2D matrix, A, of dimensions $(N_x \cdot N_y) \times N$, calling N_x and N_y the number of pixels along x and y and recalling that the number of frames is N. The singular value decomposition of A is given by

$$A = USV^\top. \tag{2.16}$$

As long as $(N_x \cdot N_y) > N$, S is a $N \times N$ diagonal matrix with singular value of A on the diagonal, $V^\top$ is a $N \times N$ matrix and, U a $(N_x \cdot N_y) \times N$ matrix. With the typical re-arrangement of matrix A, it can be shown that columns of U represent a set of empirical orthogonal functions describing the spatial variation of the data. Among these functions, the first two represent the relevant systematic spatial variations [27]. Finally, vectors of U can be reorganized in $N_x \times N_y$ matrices that serve as EOFs.

3 Numerical simulations initiation

To model numerically the physics of non-destructive techniques described in chapter 2, some understanding of the phenomena involved in the methods must be achieved. For both shearography (using a thermal excitation) and thermography, the first physical process to be modeled is the thermal problem. However, the final purpose of the former is to solve the mechanical problem induced by the thermal one. In addition, the numerical parameters required for good modeling will be discussed.

1 Governing equations

Whether in thermography or shearography, the inspected object is stimulated thermally. The focus is on the propagation of the thermal field even though in shearography, the concern is on the resulting displacement field. Therefore, the problem is **fully transient** and no steady-state assumptions can be made. In the more general case, the temperature and displacement fields influence each other, meaning that a modification of the temperature inside the material will impact the displacement field and vice versa. The classical form of the couple heat equation without heat generation is as follow [29]

$$c_p \, \rho \, \dot{T} = \left(k_{ij} \, T_{,j} \right)_{,i} \; - \; T_0 \, \beta_{ij} \, \dot{\varepsilon}_{ij} \tag{3.1}$$

where the Einstein summation convention holds, T_0 is the reference temperature, ρ the density, c_p the specific heat, k_{ij} are the components of the thermal conductivity tensor, ε_{ij} of the components the strain tensor, i and j are space variable and can take the value $1, 2, 3$. Note that the notation ",i" stands for the partial derivative with respect to i for instance: $T_{,i} = \frac{\partial T}{\partial x_i}$. Finally, β_{ij} are the tensor coefficients characterizing the thermal expansion properties of the material. In fact

$$\beta_{ij} = C_{ijkl} \, \alpha_{kl}, \tag{3.2}$$

with C_{ijkl}, the components of the well-known stiffness tensor and α_{ij}, the thermal expansion coefficients. In Eq. 3.1, the term "$T_0 \, \beta_{ij} \, \dot{\varepsilon}_{ij}$" shows the coupling between temperature and displacement. Recall that strains are linked to displacement by the relation (in **small-strains** assumption):

$$\varepsilon_{ij} = \frac{1}{2} \left(\frac{\partial u_i}{\partial x_j} + \frac{\partial u_j}{\partial x_i} \right). \tag{3.3}$$

In addition to the heat equation, the equation of motion in the absence of volume forces is written

$$\sigma_{ij,\, j} = \rho \, \ddot{u}_i, \tag{3.4}$$

where σ_{ij} are the stress tensor components, and the stress-strain relation, assuming a linear thermoelastic behavior, is given by

$$\sigma_{ij} = C_{ijkl}\,\varepsilon_{kl}\, -\, \beta_{ij}\,(T - T_0)\,. \tag{3.5}$$

The physic is then fully described by Eq. 3.1, Eq. 3.3, Eq. 3.4 and Eq. 3.5. This set of equations can only be solved analytically for some fundamental cases. This work aims to use numerical methods to approximate the solution, finite element method are implemented in the solver `Samcef`. However, some more assumptions to simplify the problem can be made.

In many engineering applications, the couple theory is far away from being used as the coupling term is negligible. The point is whether this theory should be applied or not. The excitation is produced by an infrared lamp at a certain distance, resulting in an imposed flux rising the sample temperature quite slowly. This flux implies a rather low-temperature rise at the surface of the material. By experience in NDT, a rise of 3°C is generally sought. In some extreme cases, a change of ~ 10°C is reached, but in any way, this rise is reached with the same lamp, meaning that the time needed for the object to raise its temperature is higher. Even though the imposed flux is imposed suddenly, the temperature at the surface takes some time to adapt. This aspect eludes the case considered of thermal shocks for which the coupled theory must be used ([30] & [31]).

Another problem that can be considered is that this work focuses on the simulation of defects and the defect can locally affect the thermal properties. Mechanical stresses may enhance the defect and consequently alter the intrinsic properties during the experience. To be more convinced that the physic is well represented by the **uncouple problem** (Eq. 3.1 without the coupling term "$T_0\,\beta_{ij}\,\dot{\varepsilon}_{ij}$"), the solution of the couple and uncouple equations can be obtained and compared. However, since the solution is not trivial, a numerical analysis is preferred. In a time-saving approach, the results from the technical report [4] are used to show that results can totally be obtained from the uncoupled equations. This report has simulated a true delamination in a plate submitted to a heat flux for a few seconds. An approach with coupled equations was studied to compare it to the approach using decoupled equations. Results for the temperature at a particular point are shown in Fig. 3.1. It can be seen that the temperature evolution is sensibly the same whatever the approach.

The last assumption that can simplify the problem is the **quasi-static** assumption. The term quasi-static refers to the fact that the thermal part is nevertheless transient, but the inertia term ($\ddot{u}$ in Eq. 3.4) is neglected. This assumption implies that the possible induced thermal vibrations will not be represented. According to [32], this assumption holds if the characteristic time of the thermal problem (t_T) is a lot larger than the characteristic time of the mechanical one (t_M). Note that t_M is in fact the inverse of the first natural frequency and can be estimated quite easily for
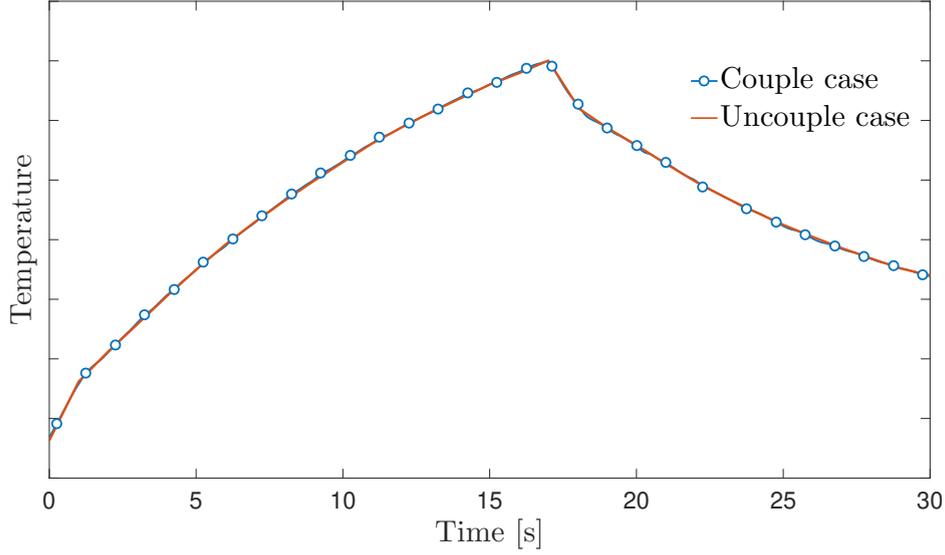
Figure 3.1: Temperature time evolution at a point above the defect. Curves digitalized from [4]. Results are obtained numerically with the two approaches: couple and uncouple.

a plate. The characteristic times are given in [33] as

$$t_T = \frac{t_o^2 \, \rho \, c_p}{k} \quad \& \quad t_M = l^2 \sqrt{\frac{t_o \, \rho}{D}} \tag{3.6}$$

with k the conductivity along with the thickness, t_o the plate thickness, a the small side, D the flexural stiffness and is of the following form for a plate:

$$D = \frac{E \, t_o^3}{12 \, (1 - \nu^2)}. \tag{3.7}$$

The young modulus and the Poisson's ratio are respectively represented by E and ν. These parameters are a priory unknown but some first estimations can be done. Considering that most of the samples tested are in CFRP, those parameters are estimated by

$$t_o \simeq 0.005 \text{ [m]}, \quad l \simeq 0.2 \text{ [m]}, \quad k \simeq 0.8 \text{ [W/(m K)]}, \quad \rho \simeq 1500 \text{ [kg/m}^3\text{]},$$

$$c_p \simeq 1200 \text{ [J/(kg K)]}, \quad E \simeq 4.3 \cdot 10^9 \text{ [Pa]}, \quad \nu \simeq 0.3 \text{ [$-$]}. \tag{3.8}$$

This gives $t_T \simeq 56.25$ [s] and $t_M \simeq 0.016$ [s], consistent with the quasi-static problem hypothesis.

To resume, the assumptions made in this section are listed below:

- Small strains,

- Linear thermoelasticity,

- Uncouple thermal and mechanical, problem

- Quasi-static (transient thermal problem & static mechanical problem).

The displacements are then computed statically after the resolution of the thermal transient problem and the set of equations representing this physic degenerates in

$$c_p \, \rho \, \dot{T} = \left(k_{ij} \, T_{,j} \right)_{,i} \tag{3.9}$$

$$\varepsilon_{ij} = \frac{1}{2} \left(\frac{\partial u_i}{\partial x_j} + \frac{\partial u_j}{\partial x_i} \right). \tag{3.10}$$

$$\sigma_{ij} = C_{ijkl} \, \varepsilon_{kl} \, - \, \beta_{ij} \left(T - T_0 \right). \tag{3.11}$$

$$\sigma_{ij,\,j} = 0 \tag{3.12}$$

2 Material considerations

In the previous section, equations and physic have been presented, but no assumptions have been made on the material behavior. This section deals with material considerations.

So far, the more general case has been considered and properties have been assumed to be anisotropic. The scope of this report is on composite laminates for which orthotropic plies are stacked. Each ply is composed of fibers and a matrix, giving some different properties in different directions. The most popular type of fibers for aerospace applications is certainly carbon fibers. More often in practice, composites with unidimensional or bi-directional fibers are tested and are the focus of this work. Fibers are embedded in a matrix, for instance, an epoxy matrix which is a polymeric matrix but metallic or ceramic matrix exist too.

Considering UD stacking, with known properties at ply level and a known stacking sequence, the whole material properties can be found. The process of getting the material properties from plies and stacking sequence is called the assembly. Some theories such as the classical laminate theory (CLT) [6] exist for the assembly process. The development of the assembly theory is not the concern. Still, it was desirable to mention this process because later in the simulations, plies properties and the stacking sequence are the parameters introduced in the solver.

When one of the axes is aligned with fibers, they are called orthotropy axes (refers as x, y, z) and in these axes, it possible to demonstrate that there are 9 independent parameters that describe the mechanical properties and 8 parameters describing the thermal properties. Indeed as stated in [34], the heat equation needs 5 parameters to be solved, the density, the heat capacity, and the thermal conductivity in the three directions of orthotropy axes ($k_{ij} = k_{ii}$ in this in this frame) to which is added the thermal expansion coefficients (again $\alpha_{ij} = \alpha_{ii}$ in orthotropy axes). If radiation is taken into account, the material emissivity ϵ is one more property. Regarding the

mechanical properties, the Young modulus in the three directions plus the Poisson's coefficients and the three shear modulus in directions "xy", "xz" and "yz" are needed.

This holds for UD composites, but in woven fabrics, it is sometimes possible to reduce the number of needed parameters again. Although in practice, the tested samples are very often UD composites and that simulations must be able to represent this type of composites, it happens that samples are with woven fabrics arrangement. In this instance, numerical simulations about a delamination defect covered in the next chapter will be done using the material in carbon/epoxy woven fabric with well-known properties. The samples available have plies with same properties in the "x" and "y" direction leading to $E_x = E_y$, $G_{yz} = G_{xz}$ (G is the shear modulus), $\nu_{yz} = \nu_{xz}$, $\alpha_x = \alpha_y$ and $k_x = k_y$. It reduces the number of independent parameters to 13 instead of 18 (9+9).

The number and the independent material parameters are finally summarised in Tab. 3.1.

18 independent parameters
E_x, E_y, E_z
ν_{xy}, ν_{yz}, ν_{xz}
G_{xy}, G_{yz}, G_{xz}
α_x, α_y, α_z
k_x, k_y, k_z
ρ, c_p, ϵ

(a) General UD composites.

13 independent parameters
$E_x = E_y$, E_z
ν_{xy}, $\nu_{yz} = \nu_{xz}$
G_{xy}, $G_{yz} = G_{xz}$
$\alpha_x = \alpha_y$, α_z
$k_x = k_y$, k_z
ρ, c_p, ϵ

(b) Woven fabric carbon/epoxy (real sample for testing and simulations).

Table 3.1: Independent parameters for the case of UD composites and the one of carbon/epoxy woven fabrics.

3 Loads, boundary and initials conditions

Boundary and initials conditions strongly influence the solution. Their influence has been studied and introduced into the problem. As only the thermal part is treated as transient, only thermal conditions will appear in initials conditions. On the other hand, boundary conditions exist for both thermal and static mechanical problems. The heat load is under a radiative flux form and can be treated as a boundary condition[1] for the resolution of the heat equation but as to be treated as a temperature load in the mechanical part.

---

[1]Here the term boundary condition and load represent the same phenomenon as the flux is imposed at the boundaries of the object.

3.1 Thermal problem

3.1.1 Initial condition

The first discussed condition is probably the most simple, in addition to being the only initial condition. It states that the sample is at a uniform temperature at 0 seconds. It is written as

$$T(x,y,z,t=0) = T_0 \simeq 20 \ [°\mathrm{C}], \tag{3.13}$$

recalling that T_0 is the reference temperature in Eq. 3.11 and equals the room temperature.

3.1.2 Free convection

Inevitably, the sample is submitted to free convection as experiments are not conducted in the void. The free convection heat flux, q''_{conv}, is described by *Newton's law of cooling*:

$$q''_{\mathrm{conv}} = h \, (T_s - T_0), \tag{3.14}$$

with T_s is the temperature at the boundary of the solid and h the free convection coefficient. In general, instead of T_0, T_∞ is used to described the temperature of the fluid far away from the boundary layer but here, the fluid is considered to be at the reference temperature. The convection coefficient is a fluid property but also depends on the solid boundary because the boundary layer does not develop the same way on different surfaces. Considering free convection with air, a range of typical values is given in [35]:

$$h_{\mathrm{gas}} \in [2 - 25] \ [\mathrm{W/(m^2K)}]. \tag{3.15}$$

A more advanced method of the free convection coefficient computation is also developed in [35] and sum up in [36] or [37]. Note that in theory, the free convection coefficient is not the same everywhere on a surface and depends on the geometry (different h for vertical or horizontal plate for instance). However in this work, a constant convection coefficient, $h = 5 \ [\mathrm{W/(m^2K)}]$ is assumed. The advanced method shown in appendix A.1 give very similar values meaning that the assumption is not so far from reality.

The order of magnitude of the convection flux can be obtained by assuming a temperature difference of 5 degrees between the solid surface and the fluid. This is really the biggest convection flux that can arise as that temperature difference happens at the end of the heating process. It results in

$$q''_{\mathrm{conv}} \simeq 25 \ [\mathrm{W/m^2}]. \tag{3.16}$$

3.1.3 Radiative flux

The problem of radiation is a bit more complex. During the heating process, one face of the sample is submitted to an external radiative flux produced by an infrared heater. Whether the object is heated or not, the object radiates naturally to its environment. Therefore the radiative considerations are split into two phases, the heating phase and the cooling phase. The cooling phase is treated first as it is the simplest one but keep in mind that the object is first heated.

1. **Cooling phase:** During this phase, the object radiates energy to its environment because it has been heated, the sample surface is hotter than its surroundings and then loses energy through radiation. The sample is assumed to be a gray[2] diffuse[3] surface, therefore the net flux radiated to its environment, $q''_{\mathrm{rad_{cool}}}$, is governed by [35]

$$q''_{\mathrm{rad_{cool}}} = \epsilon\,\sigma_{\mathrm{S\text{-}B}}\,(T_s^4 - T_0^4). \tag{3.17}$$

   The temperature T_0 is still the reference temperature and is in fact used as the surrounding temperature, $\sigma_{\mathrm{S\text{-}B}} = 5.67 \cdot 10^{-8}$ W/(m^2 K^4) is the Stefan–Boltzmann constant. As for the free convection flux, an estimation of the flux is obtained by setting T_0 to 293 K and T_s to 298 K. The emissivity is assumed to be ~ 1 which is realistic for the samples usually tested, then

$$q''_{\mathrm{rad_{cool}}} \simeq 29.3 \; [\mathrm{W/m^2}]. \tag{3.18}$$

   The value obtained in Eq. 3.18 is similar to the free convection flux. In certain applications, it may be convenient to express the radiation flux under the following form

$$q''_{\mathrm{rad_{cool}}} = h_r\,(T_s - T_0) \qquad \text{with } h_r = \epsilon\,\sigma_{\mathrm{S\text{-}B}}\,(T_s + T_0)(T_s^2 + T_0^2) \simeq 5.85 \; [\mathrm{W/(m^2 K)}], \tag{3.19}$$

   This form has the advantage of giving a similar expression as for the free convection. A comparison of the radiation coefficient h_r and the free convection coefficient h can be managed and it is seen that both of them are ~ 5 W/(m^{2}K). Note that h_r is very sensitive to the temperature while the temperature dependency of h is weak. Even though the radiative flux has the same order of magnitude as the free convection flux, it will be neglected in simulations for simplicity. It could seem not logical, but both fluxes are rather low and considering only convection does not impact significantly the solution.

2. **Heating phase:** The object is illuminated with an infrared heater, and the aim is then to characterize the flux received by the object when heated. It can be achieved by resolving the three surfaces radiation problem [35]. The first two surfaces are the sample and the heater whereas the third one represents the room walls. This configuration is shown in Fig. 3.2 and 3.3.
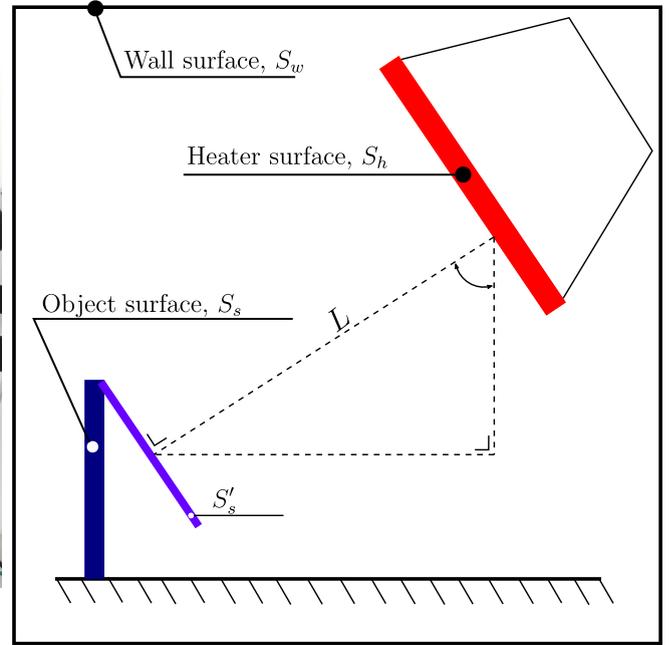
---

[2]A gray surface is a surface for which the emissivity is equal to the absorptivity.
[3]A diffuse surface is a surface that emits radiation the same way in every direction of space.
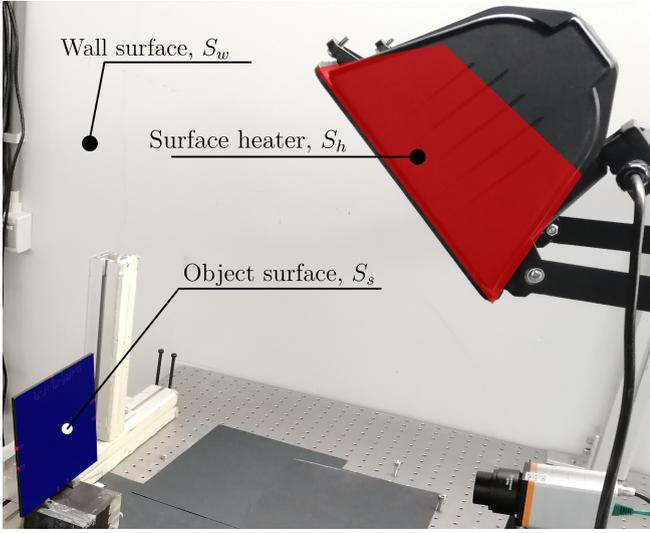
Figure 3.2: Disposition of the heater and the object in the lab.

Figure 3.3: Disposition schematic of the three surfaces radiation problem.

The three surfaces radiation problem can be rearranged under an equivalent electric circuit form, as can be seen in Fig. 3.4. In this figure, J is the radiosity (sum of radiation emitted and reflected from a surface), E_b is the emissive power of a black body and F_{ij} is the view factor between surface i and surface j. Some assumptions make possible the simplification of the equivalent circuit, in Fig. 3.4, the assumption of black bodies for all surfaces ($\epsilon_w = \epsilon_h = \epsilon_s = 1$) enable to go from step 1 to step 2. At the beginning of the heating process, $T_w = T_s$ enabling again to go from step 2 to step 3 because in this case, $q_{\text{rad}_{ws}} = 0$ W.

With all these assumptions, the net radiation flux seen by the sample surface can be computed from Fig. 3.4 as follow

$$q''_{\text{rad}_{\text{heat}}} = \frac{q_{\text{rad}_{\text{heat}}}}{S_s} = \frac{S_h \, F_{hw}(E_{bh} - E_{bs})}{S_s}. \tag{3.20}$$

There are two problems with Eq. 3.20, first, the emissive power of the heater is unknown and its temperature is unknown. However the electric power (P_h) is known, doing the hypothesis that the electric power is equal to the illuminating power:

$$P_h = S_h \, E_{bh}, \tag{3.21}$$

and inserting Eq. 3.21 in Eq. 3.20,

$$q''_{\text{rad}_{\text{heat}}} = \frac{F_{hw}(P_h - S_h \, E_{bs})}{S_s}. \tag{3.22}$$
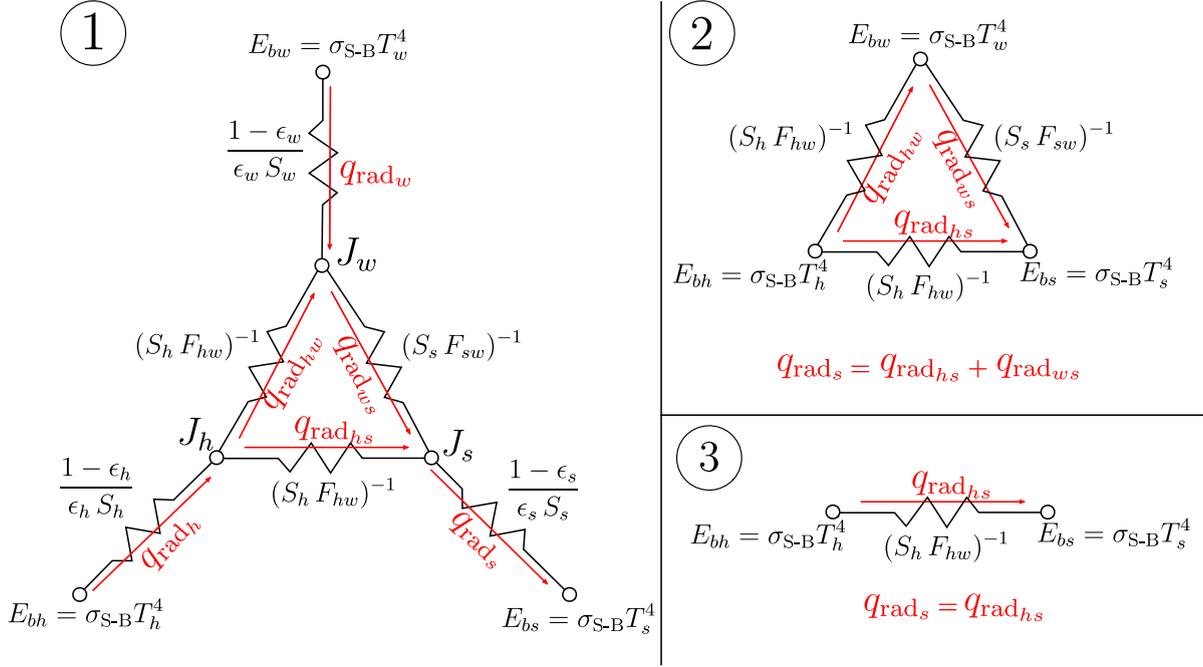
Figure 3.4: Equivalent electric circuit for the three surfaces radiation problem.

Then, the view factor is also unknown, fortunately, there is an analytical relation to view factors calculation. It can be estimated by relations in Fig. 3.5 ([35]), where i is the heater and j, the tested object. As the surfaces involved are rectangles, the radius is taken to have the same surface area:

$$r_i = r_h = \sqrt{\frac{S_h}{\pi}} \quad \& \quad r_j = r_s = \sqrt{\frac{S'_h}{\pi}} \tag{3.23}$$

with S'_s the projected surface area in Fig. 3.3 such as $S'_s = S_s \sin(55°)$.

Figure 3.5: View factor of coaxial parallel disks [35].

Taking, $L = 0.3$ m, $S_s = 0.184 \cdot 0.148 = 0.0272$ m^2, $S_h = 0.3 \cdot 0.15 = 0.045$ m^2, it comes

$$F_{hs} = 0.0559 \quad [-]. \tag{3.24}$$

Eventually, knowing that $P_h = 1300$ W and that $T_s = 293$ K (at the beginning of the heating process, the sample is at room temperature), Eq. 3.22 lead to

$$q''_{\text{rad}_{\text{heat}}} = 3023 \quad [\text{W/m}^2] \simeq 3000 \quad [\text{W/m}^2] \tag{3.25}$$

It is interesting to see that this value is way higher than q''_{conv} meaning that the convection is negligible during this process.

3.2 Mechanical problem

3.2.1 Thermal loads

The object is submitted to thermal loads via the heater. Mechanically, it is translated by a thermal field that introduces deformation in the solid. The thermal field is not homogeneous and varies in time. As the mechanical problem is solved statically, the thermal field (obtained from the transient thermal problem) at a particular time is imposed at each point of the solid. Mathematically, it can be written

$$\Delta T(x,y,z) = T_{tr}(x,y,z,t=t_p) - T_0, \tag{3.26}$$

where T_{tr} is the temperature field and t_p is a particular instant.

3.2.2 Fixations

Two fixation cases are investigated. This choice is mainly driven by the fact that the samples available present two different cases of fixations. The first sample has a frame that blocks all displacements at the edges. The other one does not have any fixations and is considered as being submitted to free-free condition. In reality, the free-free condition never exists but this condition is also inspected because it might represents the worst conditions for defect detection. If the defect can be identified with the worst conditions, better conditions will work even better for the detection.

Clamp case

For the clamp case, a frame is fixed to maintain the plate edges. This frame bites the edges to avoid any displacement. Of course, in practice, this is never perfect and some displacement may nevertheless occur. This fixation is exposed in Fig. 3.6 where the bite is well seen at the right.

The clamping condition in simulation is imposed on lateral faces by blocking all degrees of freedom on these faces, as can be seen in Fig 3.7. Even though it does not represent perfectly the frame described before, it is considered sufficient to represent the effect of the frame globally.

Free-free case

The free-free fixation case is more subjected to a discussion as in simulation it is straightforward to not constraint the plate but on the contrary, in real life, the plate must be maintained at some points. In the laboratory, what is done is shown in Fig. 3.8. The plate is actually supported punctually by two bars and leaned underneath on a block to limit the supports on the bottom face. The plate is only in contact with the bars with the smallest possible surface area, which is
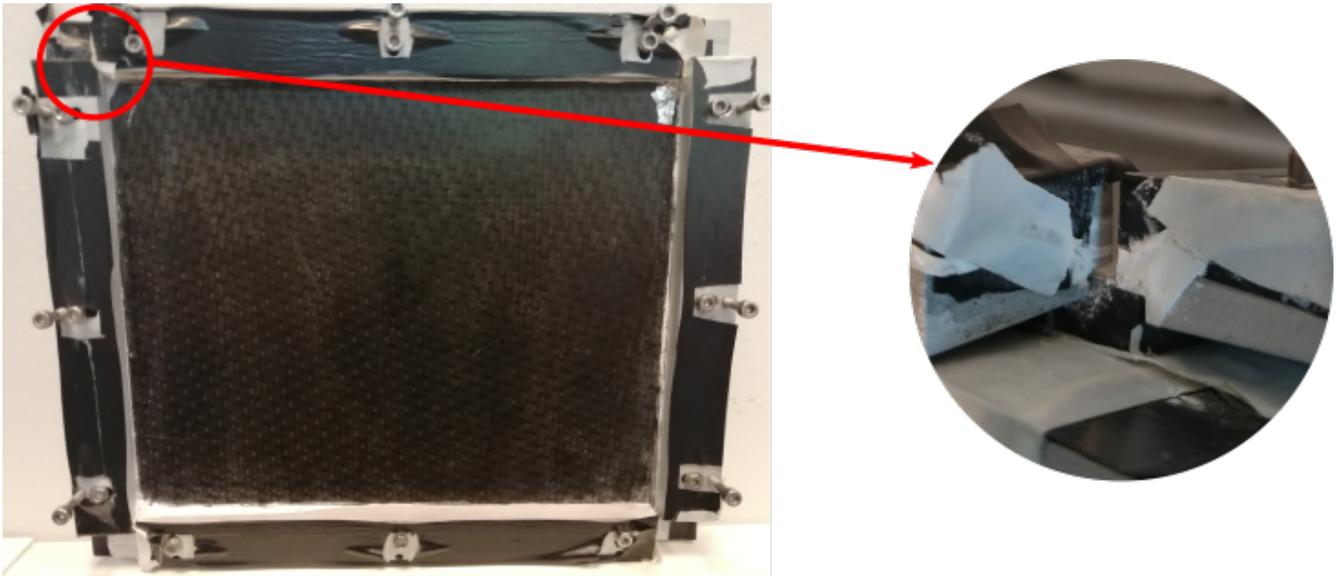
Figure 3.6: Clamping fixation

Clamped face
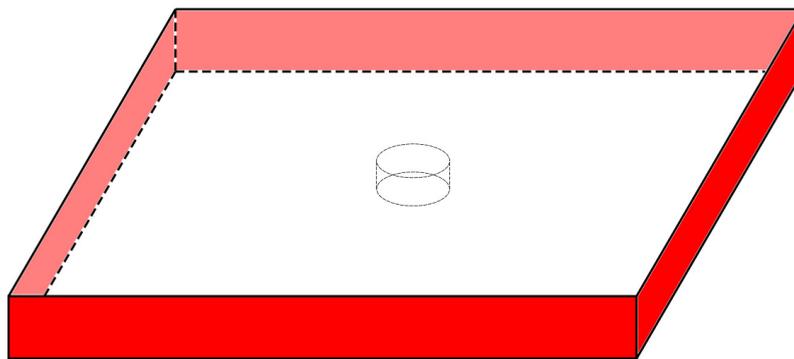
Figure 3.7: Clamping fixations case in simulations.

why it is inclined. The plate is not really free though, some discussions of the impact of these introduced conditions might be managed later on.

In simulations, the free-free fixation case is imposed by blocking degrees of freedom of one point. This point is chosen to be the center point of the upper face, as seen in Fig. 3.9. A point must be constrained in any case to prevent rigid body modes that would cause trouble to the numerical simulation algorithms used to get the solution. Any points could have been fixed, but the center is a better choice as more symmetry is kept in the model.

4 Resolution

The problem has been addressed with its boundary conditions and has to be solved now. Analytical solutions exist for some elementary cases [31]. This work aims to use numerical simulations to obtain the solution, finite elements are chosen and the solver `Samcef` is preferred. It gives tools to model composite laminates under thermal loads. Although it is possible to couple the prob-
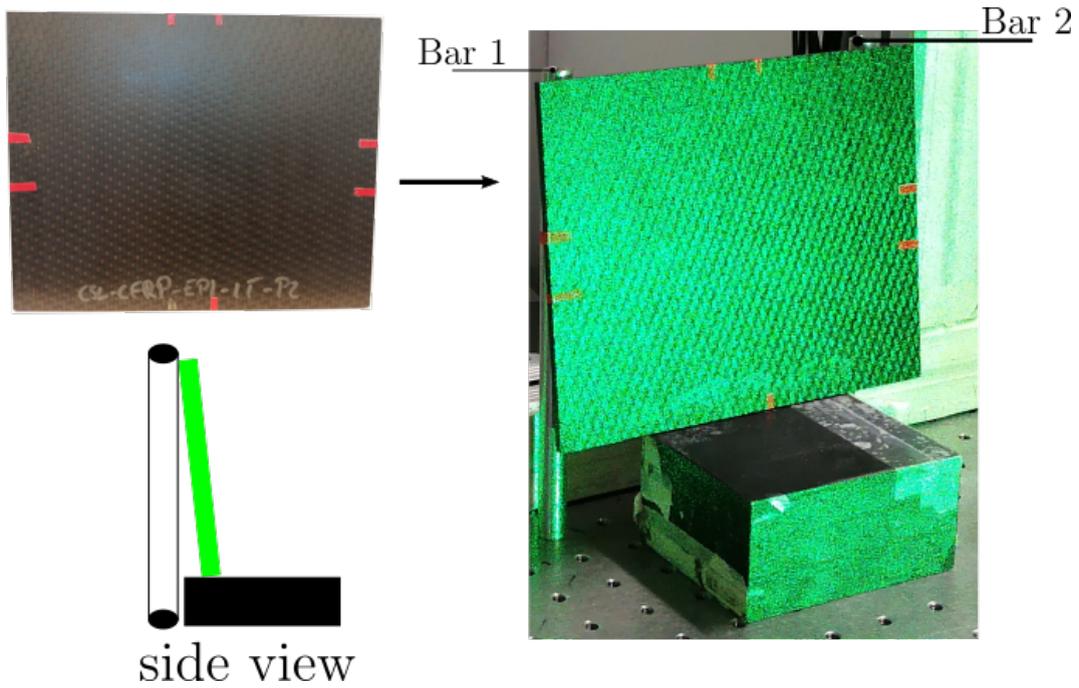
Figure 3.8: Fixation close to free constraints use in the lab.

● Blocked point
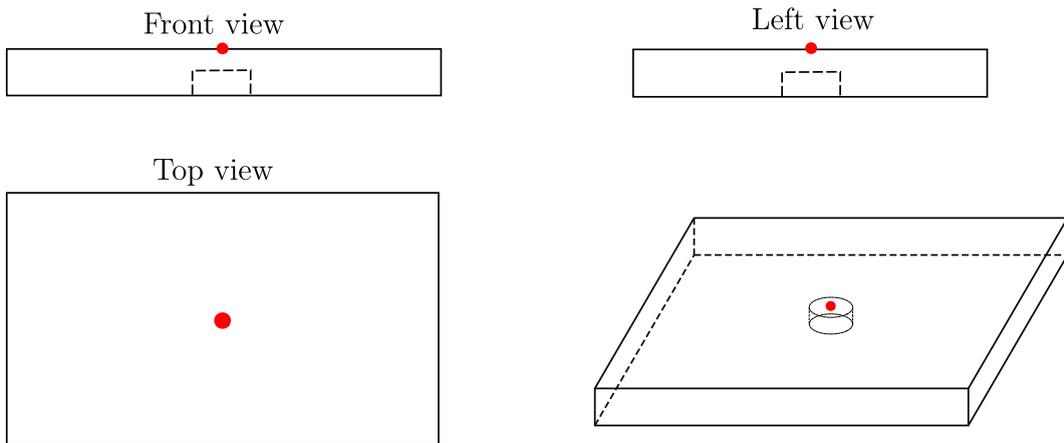
Figure 3.9: Free-free fixation case in simulation.

lem using `Samcef Co-simulation`, the decoupled quasi-static approach is adopted (this choice has been justified in section 1). The problem is then decomposed into two parts, the thermal solution and the mechanical solution. From the thermal transient solution, the temperature must be imposed. **The exact same mesh** is conserved for the two parts to be able to impose the temperature easily. The description of the mesh will be particularized to the defect model in the next chapters. A code is automated to resolve the thermal problem and reimpose the temperature field at the desire time step. As the thermal problem is transient, an iterative scheme must be chosen. The mechanical part is solved by the usual finite element method in static mechanics. Its description is not the point in this work.

4.1 Iterative scheme

In `Samcef thermal`, the transient response is obtained with a first-order implicit time integration scheme [38]. Between the iteration n and $n+1$, the time domain is divided into one-time interval such as

$$t_\gamma = (1-\gamma)t_n + \gamma t_{n+1}. \tag{3.27}$$

Different values of the parameter γ are possible. Hence different schemes can be used for the resolution:

1. $\gamma = 1$: fully implicit Euler scheme. This scheme gives good stability properties.

2. $\gamma = \frac{2}{3}$: Galerkin type weighting scheme. The stability properties are not as good as for the Euler scheme but the accuracy is better.

3. $\gamma = \frac{1}{2}$: Crank-Nicolson scheme. The best accuracy is reached with this scheme, although it may be subjected to numerical oscillations although unconditionally stable.

In the best accuracy vision, the Crank-Nicolson scheme is chosen. Therefore, particular attention to numerical oscillations is addressed. It is known that sharp initial transient condition will introduce oscillations in the solution [39]. Damping these oscillations can be achieved by reducing the time step or smoothing the initial conditions (in fact it is quite the same in a certain way, initial conditions seem less sharp with reduced time step). An example taken from simulations illustrates this pattern in Fig. 3.11. The radiation flux obtain in section section 3.1.3 is imposed sharply for 8 seconds as can be seen in Fig. 3.10, it goes from 0 to 3000 [W/m^2] in 0.1 seconds and descends from 3000 to 0 in the same amount of time at the end of the step. In Fig. 3.11, oscillations are seen for higher time step, $dt = 0.5$ to $dt = 0.2$ second whereas for smaller dt these oscillations disappear almost totally.
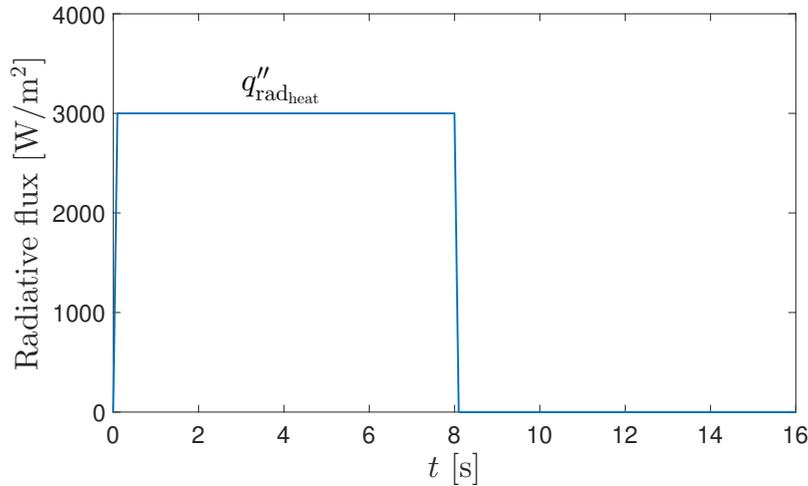
Figure 3.10: Variation of the flux imposed on the front face of the sample by the heater.

(a) $dt = 0.5$ s

(b) $dt = 0.25$ s

(c) $dt = 0.2$ s

(d) $dt = 0.125$ s

(e) $dt = 0.1$ s
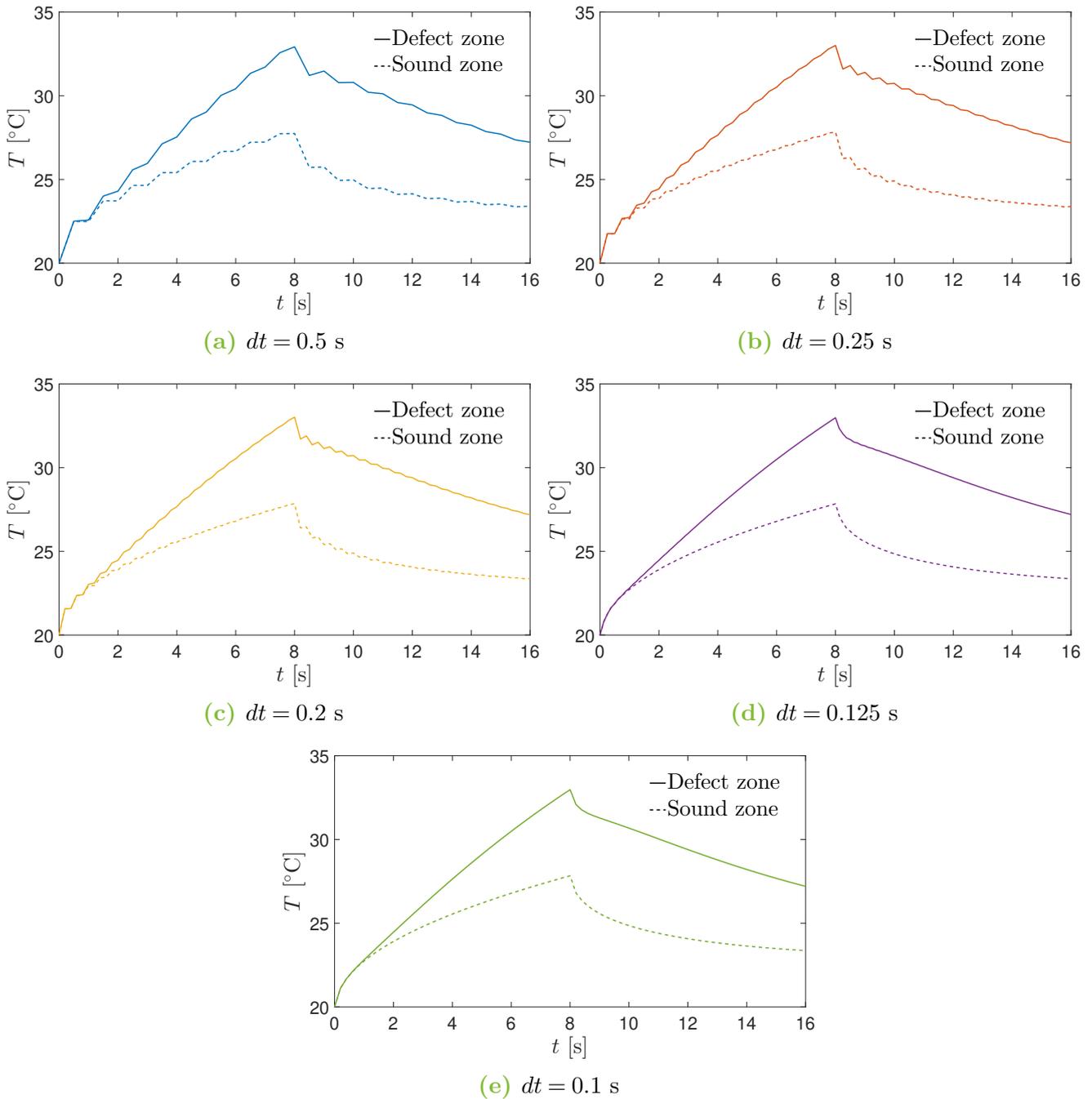
Figure 3.11: Time evolution of the temperature computed with different timestep at two points, one above the defect and one in the sound zone. Results obtained with the **Cranck-Nicolson scheme**.

The problem when reducing so much the time step is that the computation becomes very high (see Fig. A.3 in appendix A.2 for qualitative data). Reducing the time step may not be convenient and rather than reducing it, the temporal shape of the flux imposed can be smoothed. In this context, third order polynomials are used and the time for the flux to reach its maximal value is increased. The new shape is compared in Fig. 3.12 where the flux is smooth to attain its maximum value after 1 second and the solution with a time step of 0.2 seconds is obtained in Fig. 3.13. This figure shows that oscillations are totally damped with the smoother variation of flux.
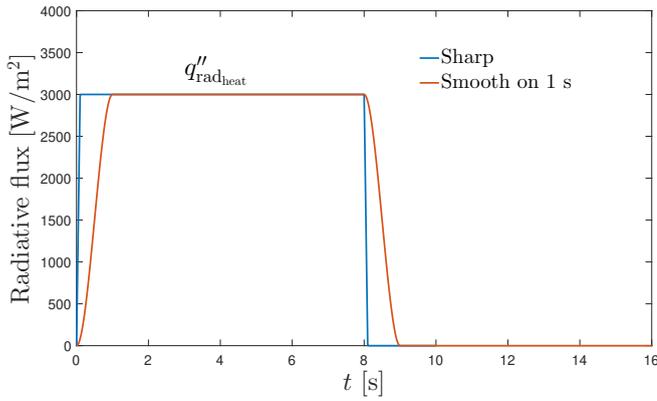
Figure 3.12: Smoother flux variation imposed on the front face of the sample by the heater.
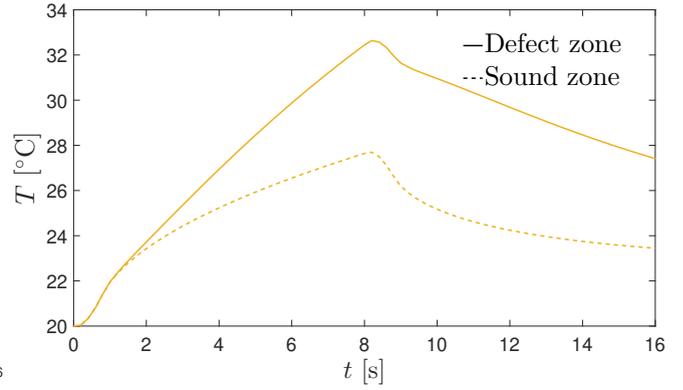
Figure 3.13: Temperature time evolution with a time step of 0.2 second and an smooth imposed flux as seen in Fig. 3.12.

Smooth initial conditions seem to lead to damped oscillations. However, in reality, the heater does not produce a smooth variation. A final solution is adopted to damp the oscillations. The smooth polynomial variation is still used but on 0.1 seconds in combination with an adaptive time step. The time step is taken very smaller near fast variation of the flux and remains higher when the flux is stable. This is illustrated in Fig. 3.14 with the shape of the flux variation, and the solution is shown in Fig. 3.15. No oscillation is present, proving that this mix solution is a good compromise.
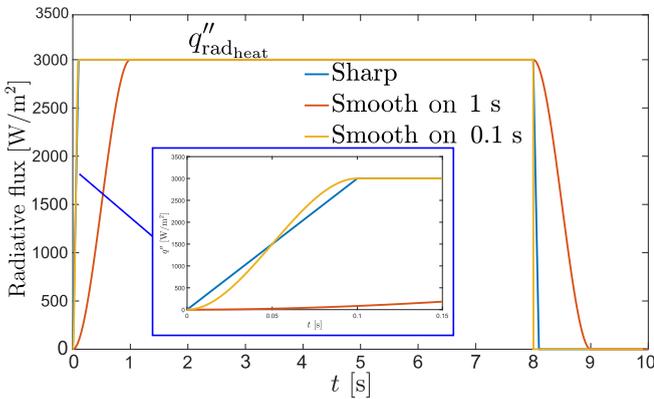
Figure 3.14: Final smoothed flux variation imposed on the front face of the sample by the heater. Smoothed flux on 0.1 second compared with previous shapes.
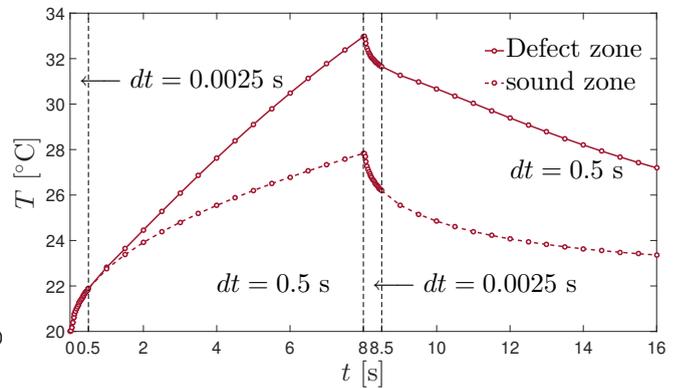
Figure 3.15: Temperature evolution with adaptive time step and a smooth flux variation on 0.1 second (see Fig. 3.14).

4 Delamination models

In the previous chapter, a bunch of considerations has been seen such as the equations related to the physics of NDT techniques, the material considerations, the load, initial and boundary conditions and finally, the transient scheme resolution. All these considerations set the basis for numerical simulations. This chapter is entirely devoted to the numerical model of a delamination. Concepts seen in the preceding chapter are then particularized to this end.

Four delamination models are investigated:

- "**True delamination**": the term true delamination might be confusing as the size and position of the delamination are unknown and cannot be modeled as such. The term "true delamination" refers to the case where the geometry is not modified in the model but only the properties at the interface between two plies are modified. Two options are investigated. The first one consists of modifying "numerically" the interface of the surface where the delamination occurs. And in the second one, a layer of air is introduced in the material to simulate the change of properties due to the presence of the defect. The thickness of the layer can be adjusted as a function of the amount of delamination.

- **Physic insert**: a physic material layer is added to represent the delamination. Material may show variables properties. Simulations focus particularly on insert in Teflon®. A study of the thermal conductivity is also performed.

- **Flat bottom hole (FBH)**: a flat bottom hole is made in the matter such as a kind of delamination is seen from the face without the hole. It is the most academic case, and it is used in practice to understand better the effect of the size, depth, etc on the detection of delaminations.

For each model, the same size and depth of delamination are considered except at section 7.3 where the depth influence is studied on the FBH model. **The free-free fixation**, described in section 3.2.2 of chapter 3, is treated for all models and the transient thermal problem is solved using the Cranck-Nicolson scheme (section 4 in chapter 3).

1 Geometry & Material

Simulations are based on a plate with known dimensions and material properties from a reference sample. This sample will also be analyzed experimentally in the next chapter. Its dimensions are presented in Fig. 4.1 and 4.2.

The plate is made of woven fabric CFRP and thirteen independent parameters are needed to fully describe a ply as shown in Tab. 3.1b. The properties are given in [3], issued from a
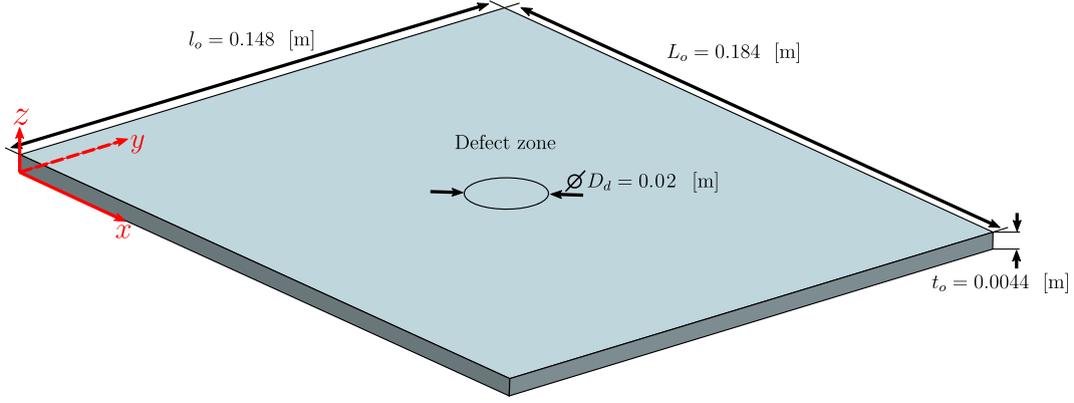
Figure 4.1: Dimension of the sample modelled in simulations.
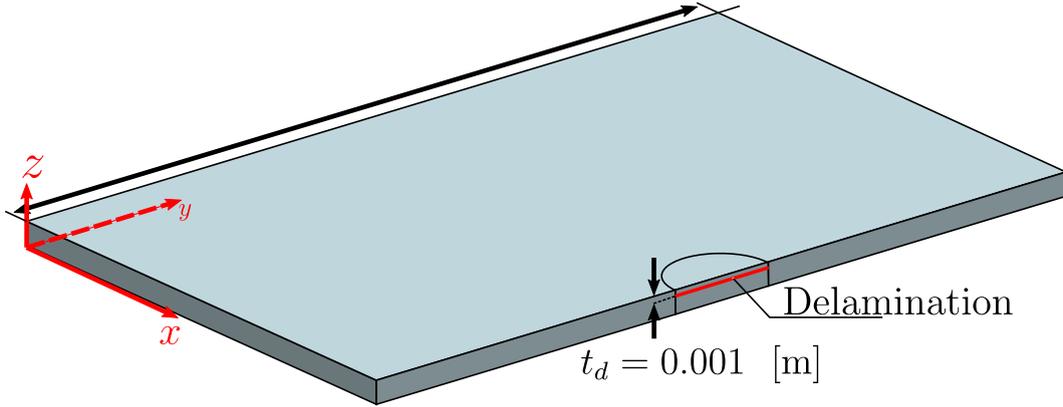
Figure 4.2: Cutting view of the sample modelled in simulations.

technical report in their hands. From this report, only mechanical properties were known, thermal properties have been estimated with common value in the literature. Thermal properties like thermal conductivity and the specific heat are taken here from [40]. Tab. 4.1 gives the value of the final properties required to set simulations where G_{xy} has been assumed equals to G_{yz} and G_{xz}. The stacking sequence is 22 plies stack with alternating plies at 0 and 90 degrees ($[90/0]_{11}$ bottom to top). Note that the stacking sequence is not symmetric. With UD composites, it leads to coupling between in- and out-of-planes effect. Nevertheless, in this particular case of woven fabric with the same properties along x and y, the composite should not show this coupling effect. Keep in mind, though, that if properties of a ply are not exactly symmetric in x and y in reality, couplings would appear.

2 Mesh

In a computation time-saving approach, only one-quarter of the plate is meshed and used to get the solution. The quarter plate kept is obtained by cutting the plate along the median of the highest surface area faces. Three zones are defined to mesh with different element size as illustrated in Fig. 4.3. On the one hand, the zone delimiting the defect region will be the most finely meshed and on the other hand, the farthest zone will contain the coarser mesh. Thermal and composites three-dimensional bricks are used respectively for the thermal and mechanical analysis. Elements

Property	Units	Value
Density	[kg/m^3]	$\rho = 1504$
Specific heat	[J/(kg K)]	$c_p = 1200$
Emissivity	[-]	$\epsilon \simeq 1$
Thermal conductivity	[W/(m K)]	$k_x = k_y = 7$ $k_z = 0.8$
Thermal expansion coefficient	[K^{-1}]	$\alpha_x = \alpha_y = 6 \cdot 10^{-6}$ $\alpha_z = 2.8 \cdot 10^{-5}$
Young modulus	[GPa]	$E_x = E_y = 67$ $E_z = 4.3$
Poisson's ratio	[-]	$\nu_{xy} = 0.037$ $\nu_{yz} = \nu_{xz} = 0.332$
Shear modulus	[GPa]	$G_{xy} = G_{yz} = G_{xz} = 4.3$

Table 4.1: Material properties of a ply in the stacking sequence $[90/0]_{11}$ (woven fabric CFRP). Properties are given in orthotropic axes.

have nodes at corners of the brick but some nodes in the middle of the edge can be added to increase precision. This second option is preferred so that elements with an increased number of nodes are selected. The choice of the element size in the different zones relies on a convergence study exposed in appendix A.2. The size is given in Tab. 4.2.
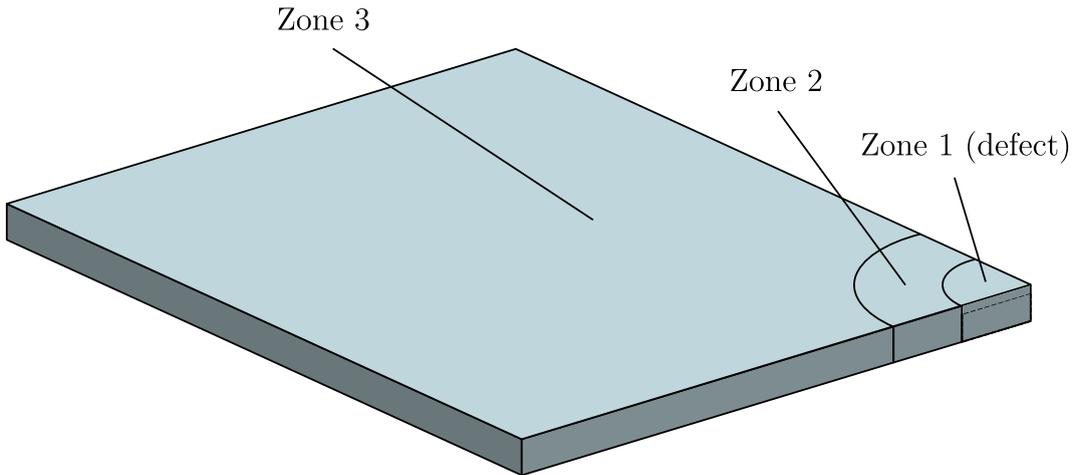
Figure 4.3: Zone delimitation for meshing. Symmetry is used and only a quarter of the plate is meshed to reduce computation time.

The last point is that each layer in the laminates is modeled by a layer of bricks leading to 22 layers of bricks along with the thickness in this case. Locally, the mesh will differ depending on the delamination model but an example with the FBH is shown in Fig. 4.4.

	Size of one element
Zone 1	2 mm
Zone 2	4 mm
Zone 3	8 mm

Table 4.2: Element size in the zone defined in Fig. 4.3.
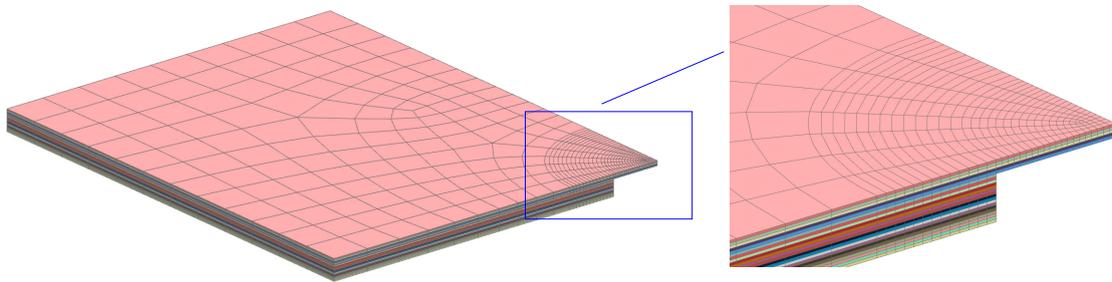
Figure 4.4: Example of typical mesh with element size given in Tab. 4.2. This example is based on the FBH model.

3   Symmetry conditions

As only a quarter of the plate is taken for the solution calculation, some symmetry conditions must be applied. On the one hand, there is no need to apply symmetry conditions in the thermal analysis, given that the correct view factor has been used for the external flux estimation. On the other hand, internal reactions may appear on the entire plate in the mechanical part and not considering them would lead to incorrect results. Some fixations are added to represent that factor and can be seen in Fig. 4.5.
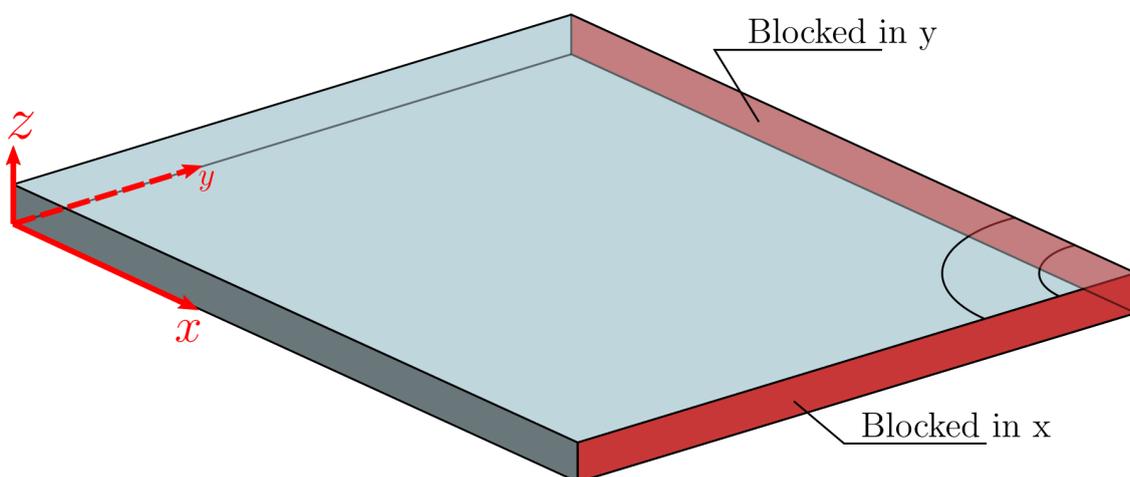
Figure 4.5: Added fixations to ensure symmetry conditions (mechanical problem only).

4 Thermal excitation

In section 3.1.3 (chapter 3), the involved radiative fluxes have been investigated. It can be recalled that the lost energy by radiation is neglected. Only the radiation coming from the heater is considered. However, bear in mind that the sample loses energy by convection applied on all faces in contact with air. The free convection coefficient is assumed to be constant ($h = 5$ W/(m^2 K) during the whole simulation.

The radiation contribution of the heater, $q''_{\mathrm{rad_{heat}}} = 3000$ W/m^2 has been computed in section 3.1.3 (chapter 3). In section 4 of chapter 3 the influence of its time variation has been highlighted. Targeting a temperature elevation of 4 K, $q''_{\mathrm{rad_{heat}}}$ is applied during two seconds as seen in Fig. 4.6. The flux variation is seen by the sample on its face exposed to the heater, Fig 4.7 illustrates this concept.
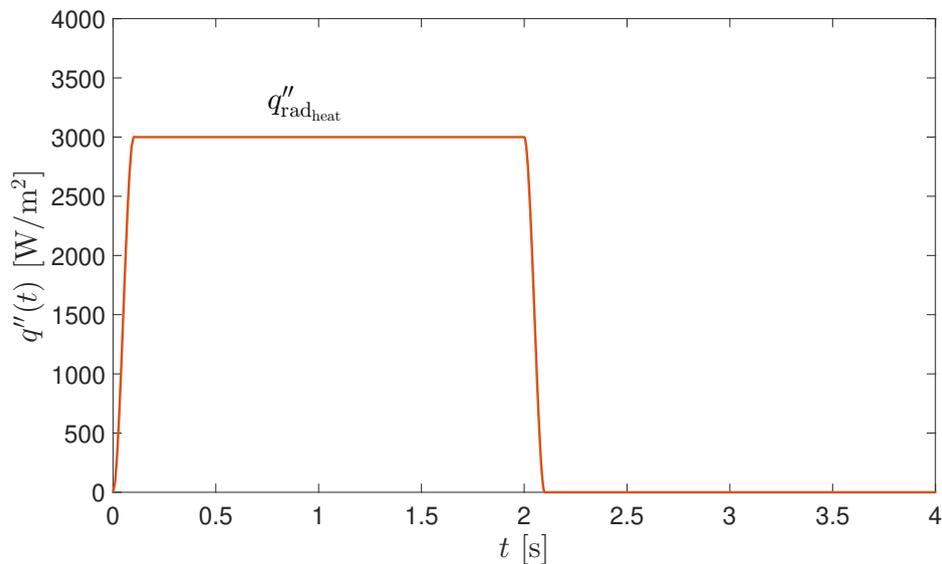
Figure 4.6: Variation of the imposed flux by the heater.
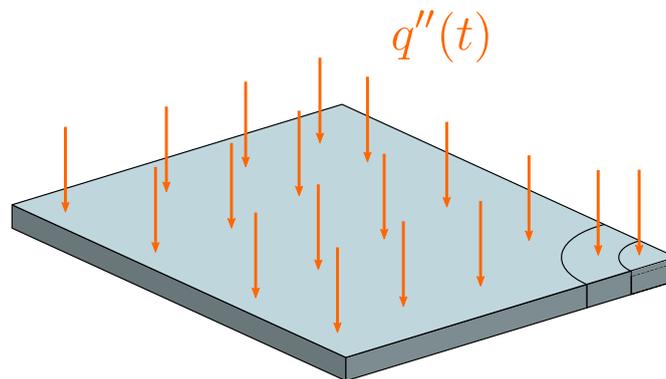
Figure 4.7: Face exposed to the heater. The time variation of $q''(t)$ is observed in Fig. 4.6.

5 True delamination

5.1 Interface modification

This model aims to represent a true delamination inside the material. This is achieved by detaching the two plies at the delamination location and imposing a thermal gluing between them as shown in Fig. 4.8.
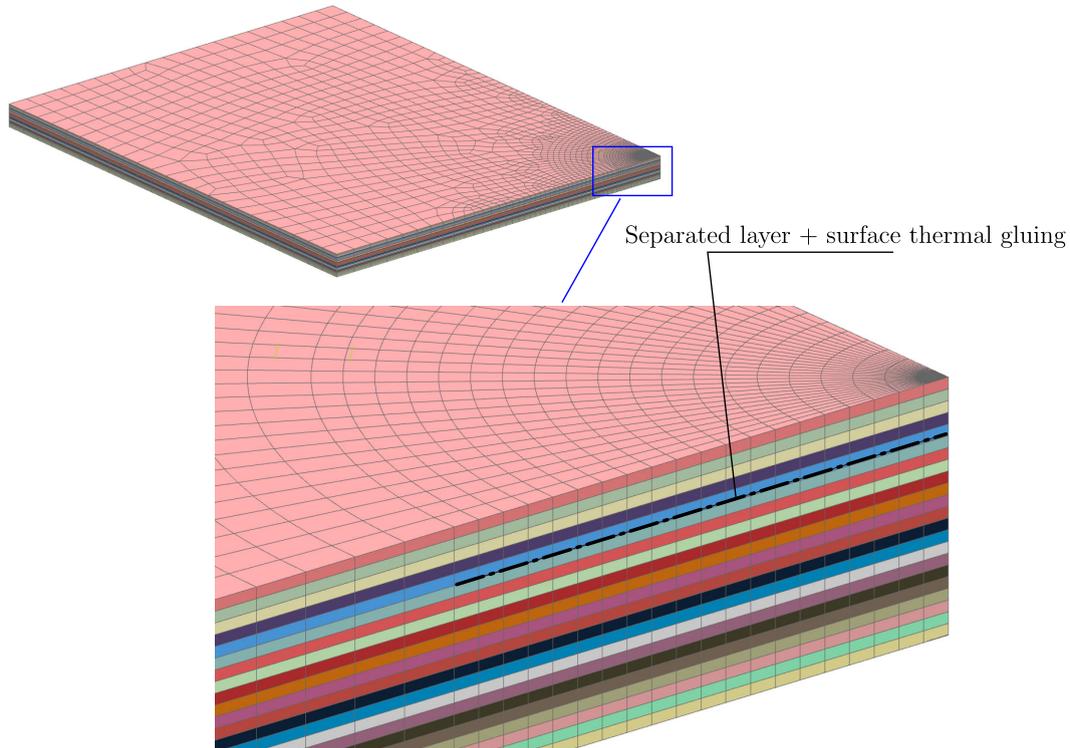
Figure 4.8: True delamination model. A thermal gluing is imposed at the delamination location and plies are physically detached.

The thermal gluing must be defined by thermal contact between the two separated surfaces. If no thermal contact was assumed, the detachment of the surfaces would lead to no interaction between them and the temperature would not be able to diffuse (which could be the case for some big delaminations). The problem is that the influence of the delamination is a priory unknown. Therefore, different gluing contact represented by k_i' at the interface is investigated. The contact (k_i') is introduced by a value representing a thermal conductivity by unit of length and enables thermal diffusion in the surface normal direction. In `Samcef`, this thermal gluing is set thanks to the ".Pritt" command. Actually, three different values are tested:

$$k_1' = 0.1 \simeq 0 \ \ [\text{W/(m}^2 \ \text{K)}] \quad \& \quad k_2' = 10^2 \ \ [\text{W/(m}^2 \ \text{K)}] \quad \& \quad k_3' = 10^3 \ \ [\text{W/(m}^2 \ \text{K)}] \tag{4.1}$$

Important remark: when using the thermal gluing condition, elements without the mid edge node are used. To compensate this fact, the size of elements given in Tab. 4.2 are divided by 2.

5.1.1 Thermal analysis

Results are obtained with all parameters discussed previously. Fig. 4.9 shows the temperature distribution at 3 seconds with the three values for k'. It is observed that the effect of the defect decreases when k' increases. Indeed, for k_3' (Fig. 4.9c), the defect is almost invisible in such a raw image like this one, whereas for k_1' the defect is very well visible. It is logical because a very low interface contact value will block the temperature diffusion locally and the temperature at this point will increase compared to a sound zone. Fig. 4.10 also illustrates this concept by showing the time evolution of the temperature at two points of the upper surface; one point in the middle (defect zone), and one point in the corner (sound zone). The contact effect is even more noticeable, for $k' \to \infty$ the defect tends to disappear.

(a) $k_1' \simeq 0$ [W/(m^2 K)]

(b) $k_2' = 10^2$ [W/(m^2 K)]

(c) $k_3' = 10^3$ [W/(m^2 K)]
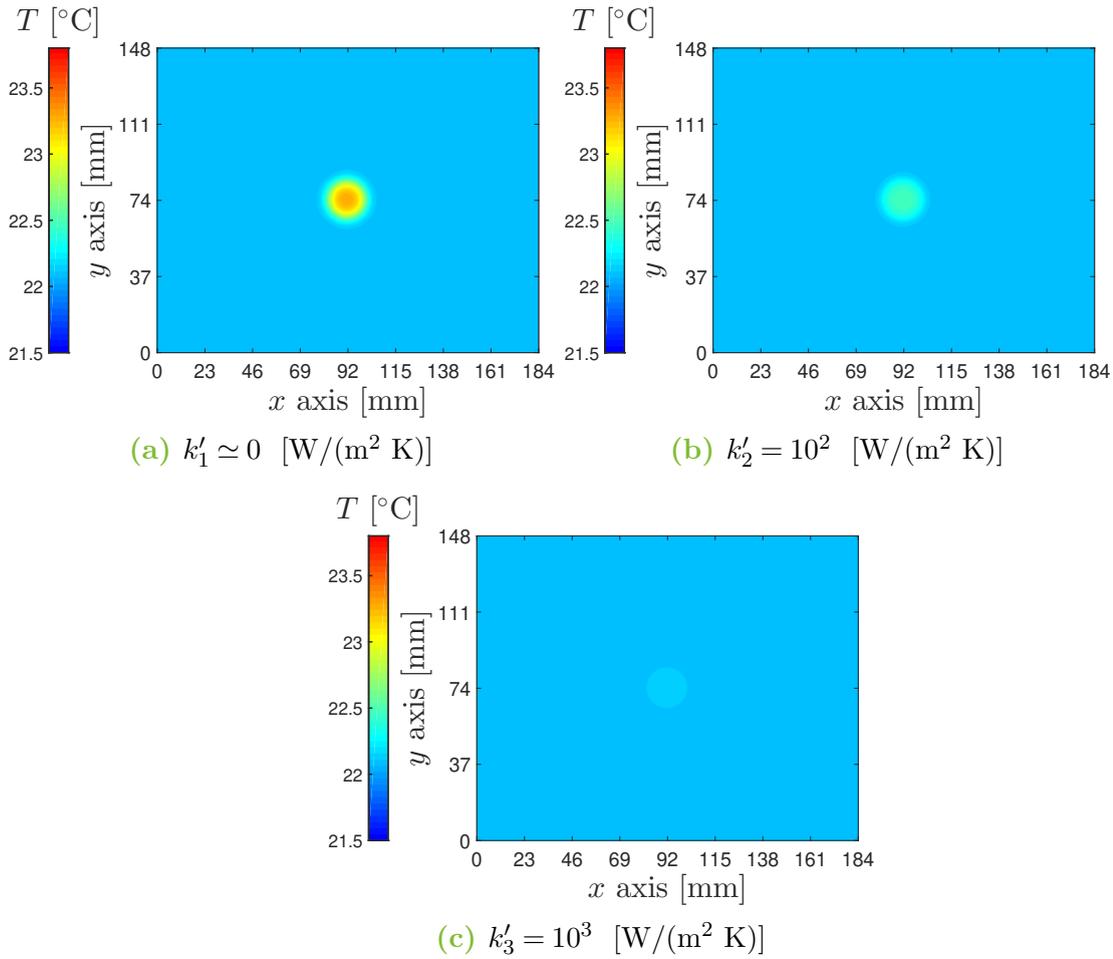
Figure 4.9: Temperature of the upper surface at 3 seconds for different value of k'.

The contrast as outlined in section 4.1 of chapter 2 is computed to quantify the defect impact and is shown in Fig. 4.11. Again it is clear that the defect impact tends to disappear with k' increasing. In addition, it can be concluded that to maximize the chances to identify the defect for k_3' visually, the thermogram (like Fig 4.9) should be looked at, at about 3 seconds.
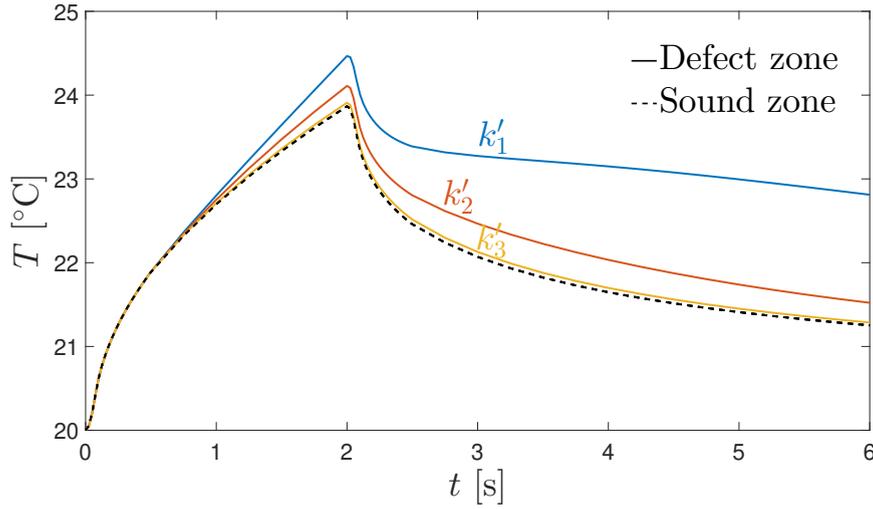
Figure 4.10: Time evolution of the temperature above the defect zone and in a sound zone. The effect of the interface conductance is shown.
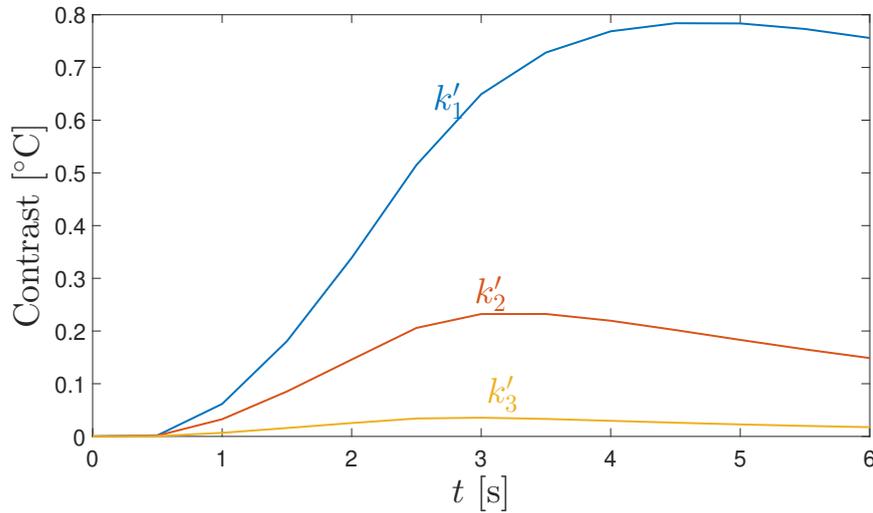
Figure 4.11: Contrast evolution with time for different values of k'.

5.1.2 Mechanical analysis

The solution provides displacements, strains and stresses in every direction. Because in shearography, the focus is on the out-of-plane displacements, Fig. 4.12 shows them for the quarter plate at 6 seconds with k'_3 by way of example. It is interesting to notice that at the delamination location, a separation has occurred. It means that the part of matter above the defect has deformed more than the part underneath.

If the upper face of the entire plate is concerned, the out-of-plane displacements, w, are shown in Fig. 4.13 for the different values of k'. They are shown at 3 seconds as the thermal contrast is the highest for k'_3 and so the relative displacements above the defect are most visible. When looking at displacements, it is often tough to see the effect of the defect, and indeed, in Fig. 4.13, the displacements seem to be the same for all k'.

The derivatives along x are thus computed and observed in Fig. 4.14. This time the defect
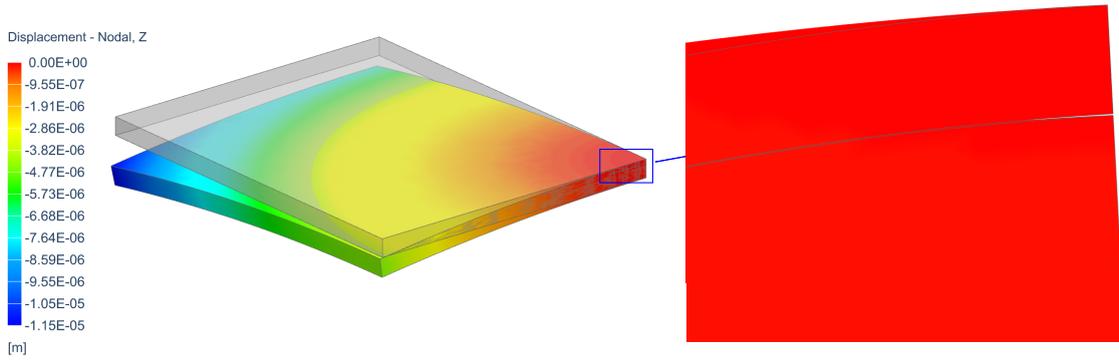
Figure 4.12: Displacements according to z (w) of the quarter plate. The image corresponds to deformation at 6 seconds with the conductance set to k_3'.

(a) $k_1' \simeq 0$ $[\mathrm{W/(m^2\ K)}]$

(b) $k_2' = 10^2$ $[\mathrm{W/(m^2\ K)}]$

(c) $k_3' = 10^3$ $[\mathrm{W/(m^2\ K)}]$
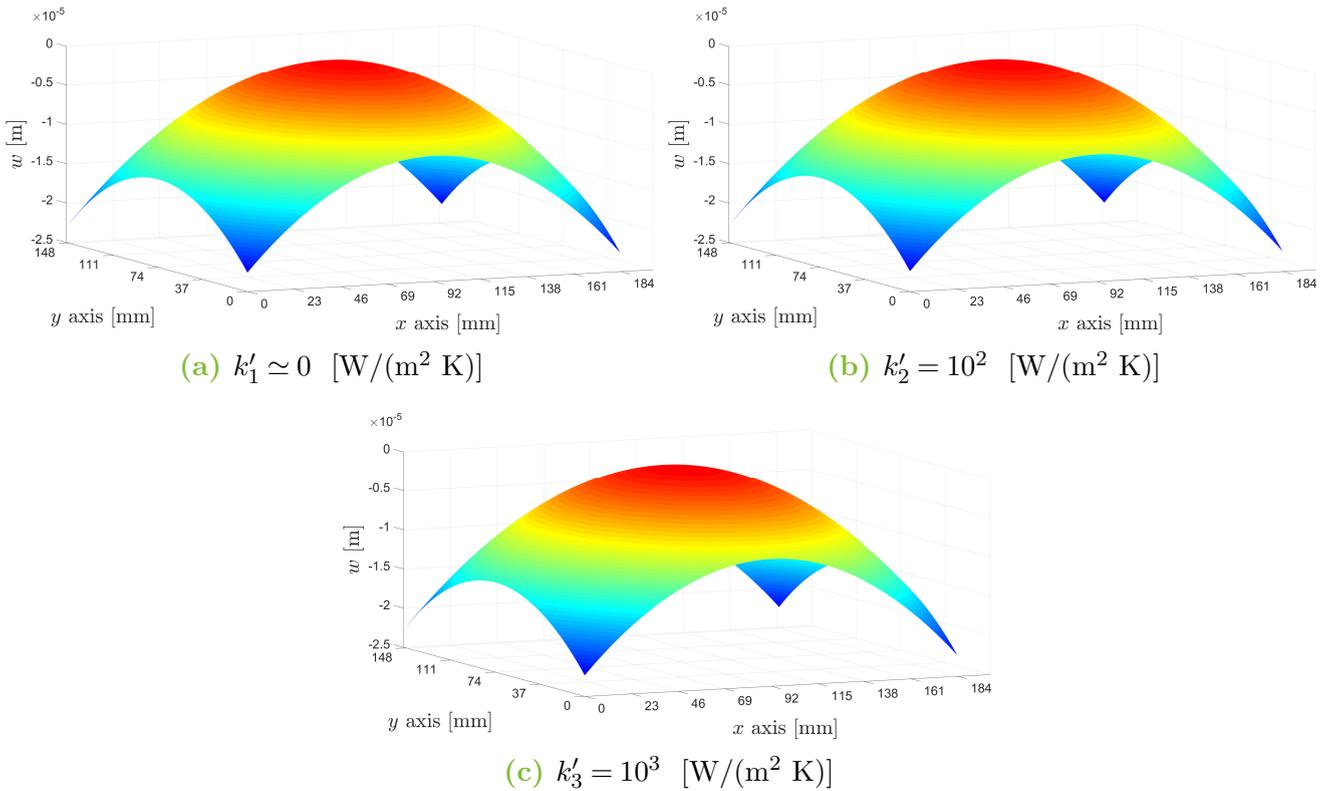
Figure 4.13: Displacements, w, of the upper surface at 3 seconds for the three values of k' tested.

impact is very well emphasized and again decreases with k'. Now the defect is visible for k_1' and k_2' but it is very hard to conclude the same for k_3'. Same conclusions can be drawn in Fig. 4.15, where phase diagrams (see section 3, chapter 2) are depicted, accounting for a shear in x direction of 0.005 m. In the phase diagram, vertical fringes can be observed representing a gradient across the x direction. Indeed, in Fig. 4.14, it can be seen that the derivatives are as a plane inclined shape (sometimes called median plane) and that is this effect that fringes represent. At the defect location, fringes are modified as the derivative is impacted at this spot. In shearography, only the phase diagram is provided and this modification of the fringes can lead to the detection of the defect.

(a) $k'_1 \simeq 0 \;\; [\mathrm{W/(m^2\ K)}]$

(b) $k'_2 = 10^2 \;\; [\mathrm{W/(m^2\ K)}]$

(c) $k'_3 = 10^3 \;\; [\mathrm{W/(m^2\ K)}]$
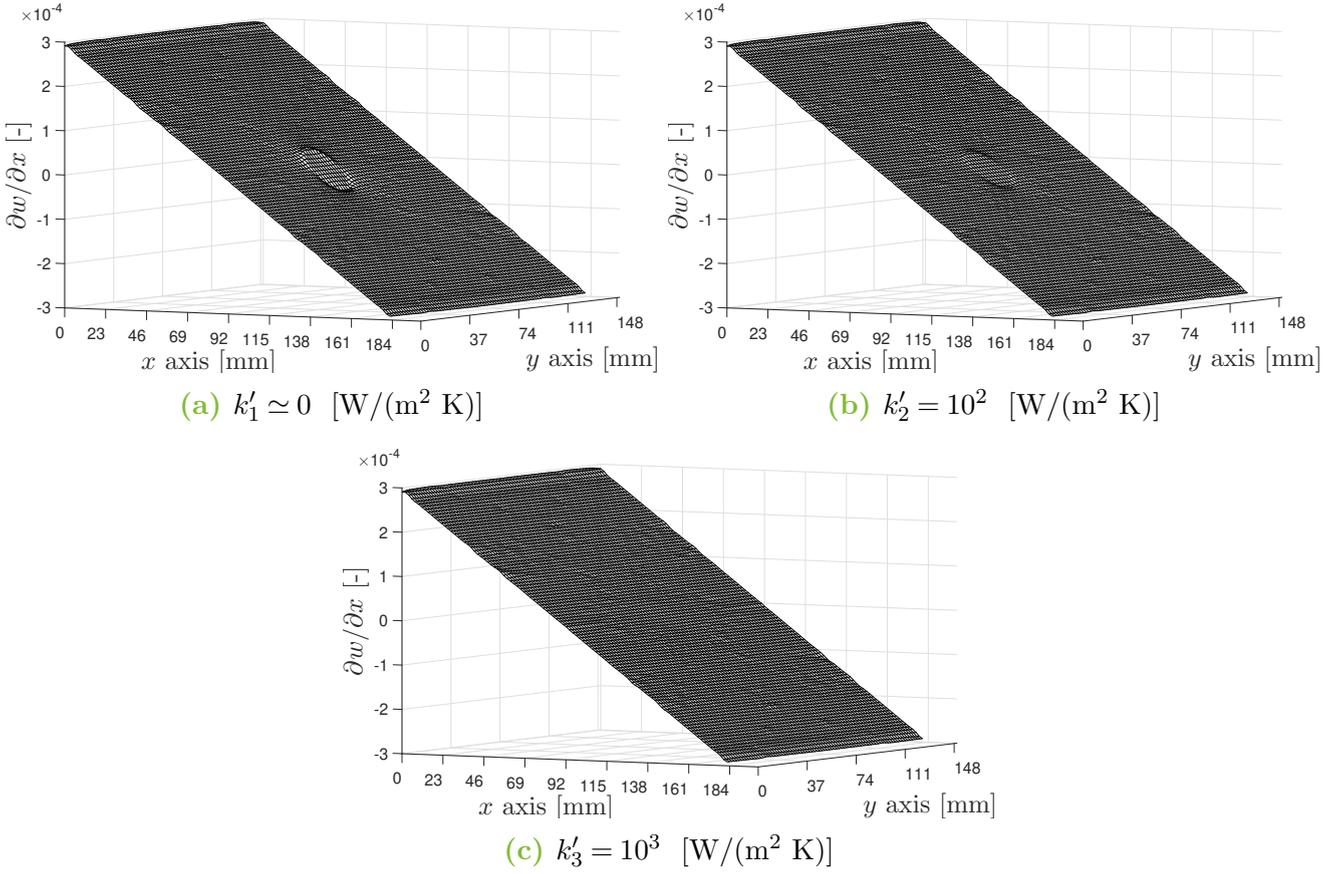
Figure 4.14: Displacement derivatives along x, $\partial w/\partial x$, of the upper surface at 3 seconds for the three values of k' tested.

5.2 Air insert

The second true delamination model consists of inserting an air layer of finite thickness. The model can be seen in Fig. 4.16, with a 0.002 m air layer thickness at 1 mm under the top surface. In the previous section, the thermal contact at the interface influenced results. For this model, the results would be affected by the air layer thickness. Compared to the interface modification where diffusion was allowed only across the surface normal, adding a real layer implies that the temperature diffusion is now tri-dimensional. An air layer thickness of 0.002 m represents a diffusion through the thickness similar to a thermal contact:

$$k' = \frac{k_a}{0.002}, \qquad (4.2)$$

with k_a the air thermal conductivity. Accounting for $k_a = 0.026$ W/(m K), the equivalent value of k' is equal to 13 W/(m^2 K). It is near k'_1 investigated in the previous section. In this work, only one model with one thickness is explored. Like the true delamination model, the air layer is purely a numerical tool to model a delamination. In practice, it is not really possible to recreate these exact conditions.

To be able to complete simulations, the physical parameters of air must be discussed. It is

(a) $k'_1 \simeq 0$ [W/(m^2 K)]

(b) $k'_2 = 10^2$ [W/(m^2 K)]

(c) $k'_3 = 10^3$ [W/(m^2 K)]
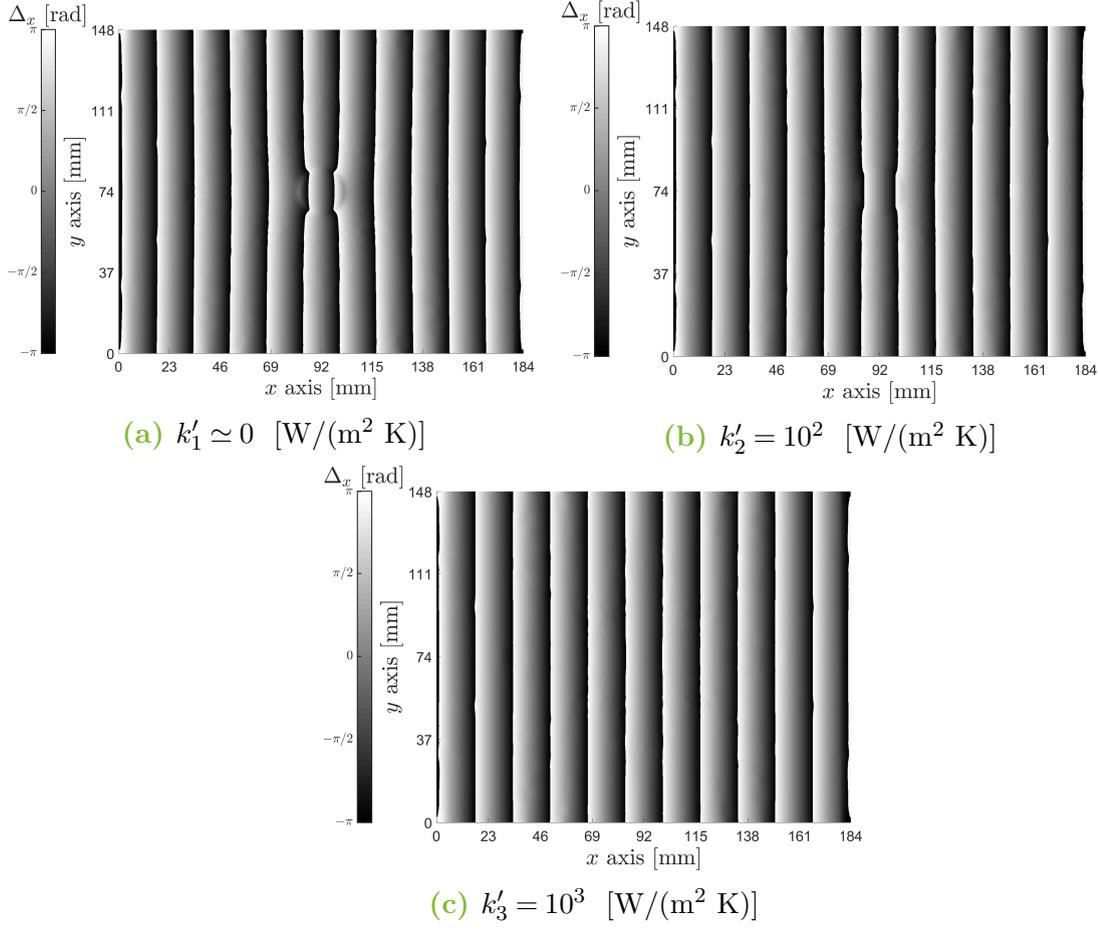
Figure 4.15: Phase diagram, Δ_x, at 3 seconds for the three values of k' tested. Shear: $\delta x = 0.005$ m.

assumed that air keeps the same properties during simulations, although in reality, properties change with temperature. This assumption is quite valid as for instance, a change from 20 °C to 25 °C only induces a change smaller than 1% on the air density. Basically, all properties are taken at 20 °C. Density, thermal expansion coefficient, thermal conductivity, specific heat are taken from [41]. For mechanical properties, the air is considered as an isotropic in-compressible gas ($\nu \sim 0.5$). The Young modulus and the shear modulus are usually not relevant when dealing with fluid; however, equivalent elastic modulus can be obtained from the bulk modulus (K). In linear isotropic theory, they are linked by ([31])

$$E = 3K(1 - 2\nu), \quad G = \frac{3K(1 - 2\nu)}{2(1 + \nu)}. \tag{4.3}$$

And finally, air properties are summarized in Tab. 4.3 where the bulk modulus is also taken from [41].

5.2.1 Thermal analysis

As for the previous model, the temperature distribution of the upper face is observed at 3 seconds in Fig. 4.17. Visually, it seems to be near the true delamination case accounting for k'_2.

Property	Units	Value
Density	[kg/m^3]	$\rho_a = 1204$
Specific heat	[J/(kg K)]	$c_{p_a} = 1006.1$
Thermal conductivity	[W/(m K)]	$k_a = 0.026$
Thermal expansion coefficient	[K^{-1}]	$\alpha_a = 0.00343$
Bulk modulus	[Pa]	$K_a = 101325$
Poisson's ratio	[-]	$\nu_a = 0.499$
Young modulus	[Pa]	$E_a = 607.5$
Shear modulus	[Pa]	$G_a = 202.785$

Table 4.3: Air properties at 20 °C.
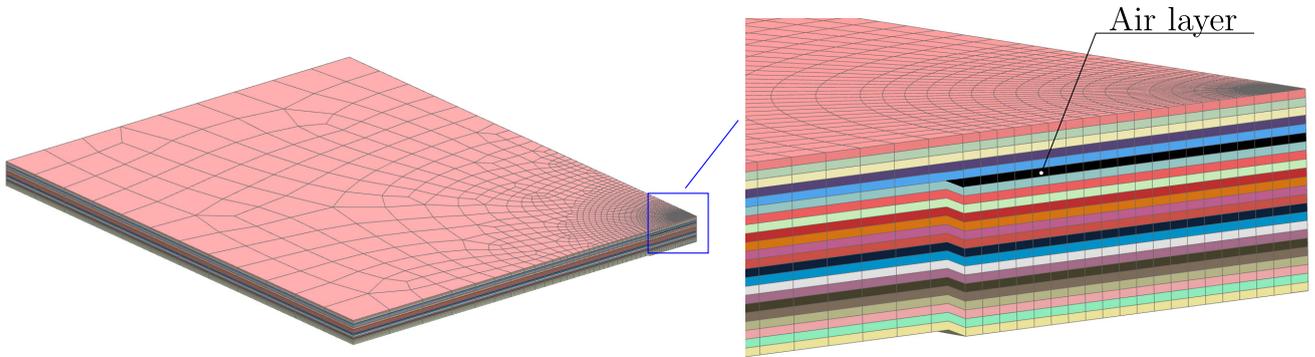
Figure 4.16: Delamination model with an air layer inserted.

When the time evolution of the temperature (Fig. 4.18) and the contrast (Fig. 4.19) are observed, it can be estimated that the case of the air layer is probably similar to a true delamination with an interface contact between k_1' and k_2'.
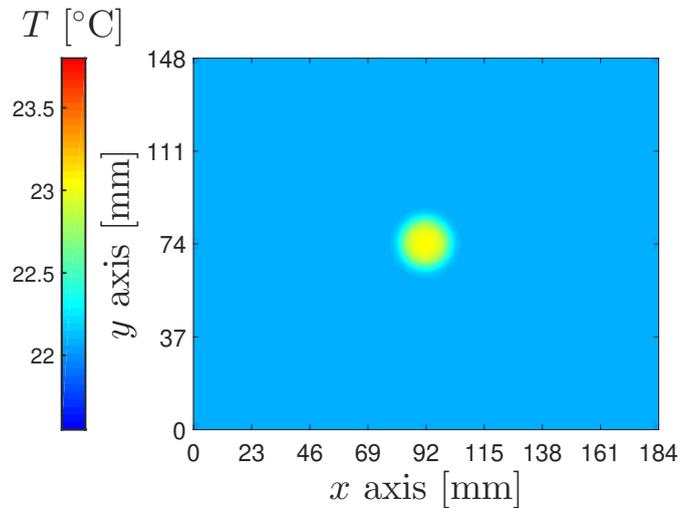
Figure 4.17: Temperature of the upper surface at three seconds with the air layer.
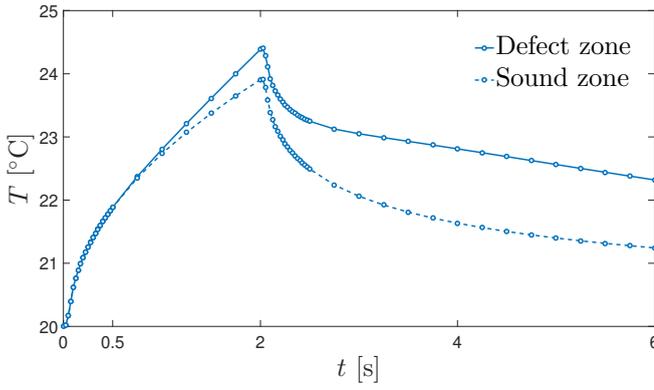
Figure 4.18: Temperature time evolution above the defect and in a sound zone .
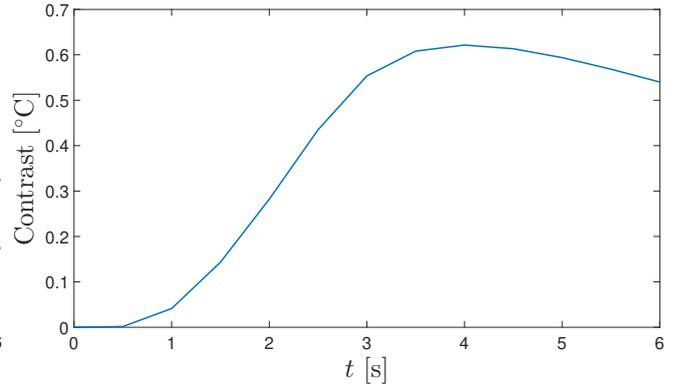
Figure 4.19: Thermal contrast evolution with the air layer.

5.2.2 Mechanical analysis

The displacements w, displacements derivatives along x and the phase diagram are shown in Fig.4.20, Fig. 4.21 and Fig 4.22, respectively. Once again the deformation in the defect zone seems to follow the continuity and no real effect is observed. The derivative and phase, on the other hand, display the presence of the defect.
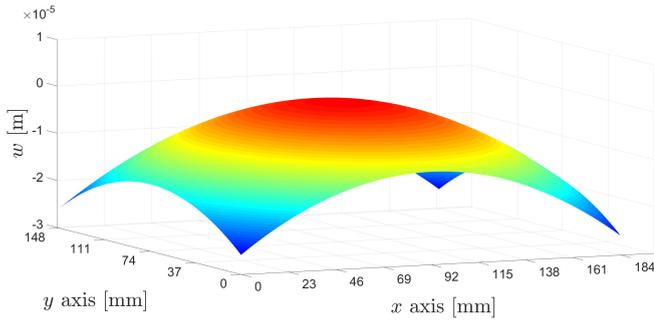
Figure 4.20: Displacements,w, of the upper surface at 3 seconds.
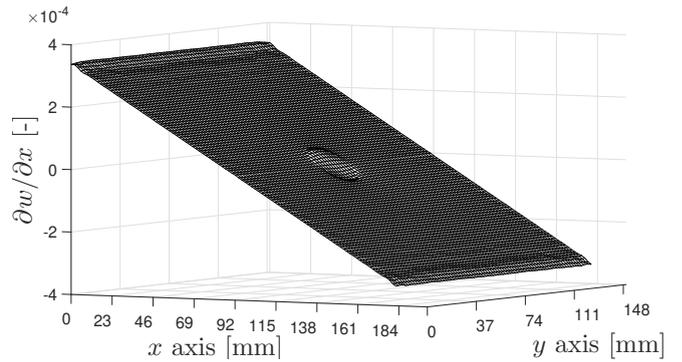
Figure 4.21: Displacement derivatives along x, $\partial w/\partial x$, of the upper surface at 3 seconds.
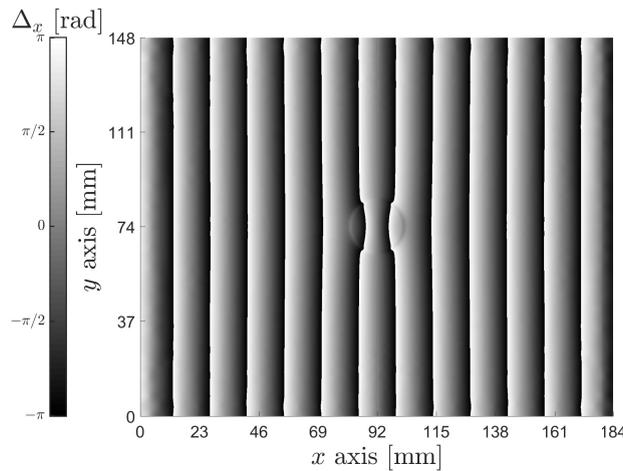
Figure 4.22: Phase diagram, Δ_x, at 3 seconds. Shear: $\delta x = 0.005$ m.

6   Physic insert

In practice, to recreate a kind of delamination with a known size and location, a layer of another material is sometimes inserted in the laminates. Inserts might be of different materials and study all of them require an overly extensive study. Therefore, it is interesting to examine these cases in numerical simulations focusing on one type of insert. As for the air layer, a layer of polytetrafluoroethylene (PTFE, also known as Teflon®) is added between two plies at 1 mm under the surface as can be seen in Fig. 4.23. As a matter of fact, in industry, other materials with different thermal conductivity are used. Hence the impact of the thermal conductivity is also studied in this section (for simplicity, other properties are kept constant and equals to the Teflon® ones).
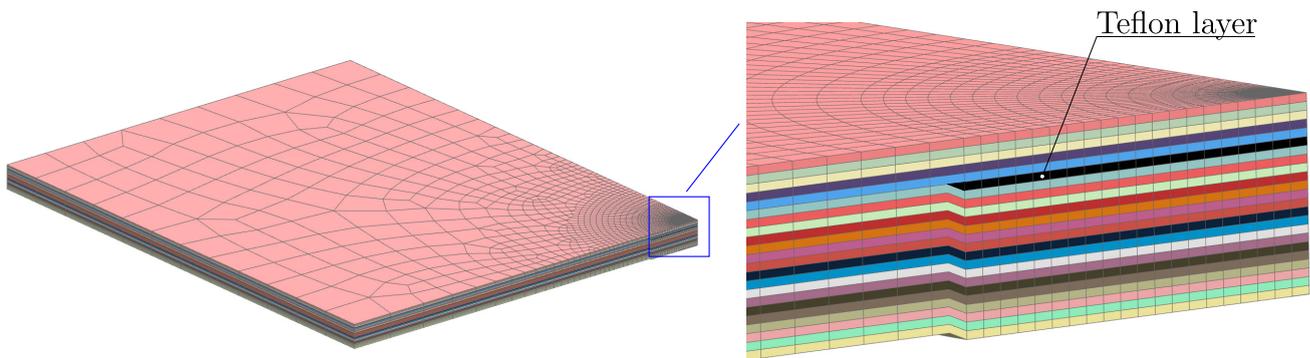
Figure 4.23: Delamination model with a Teflon® layer inserted.

Teflon® is considered to be an isotropic material. Its properties are issued from [42] and [43] are given in Tab. 4.4. The value of thermal conductivity given is the more frequent in the literature and when examining the effect of its variation, values around it are explored.

Property	Units	Value
Density	[kg/m³]	$\rho_t = 2170$
Specific heat	[J/(kg K)]	$c_{p_t} = 1000$
Thermal conductivity	[W/(m K)]	$k_t = 0.25$
Thermal expansion coefficient	[K⁻¹]	$\alpha_t = 0.00171$
Poisson's ratio	[-]	$\nu_t = 0.45$
Young modulus	[GPa]	$E_t = 0.475$
Shear modulus	[GPa]	$G_t = 0.23$

Table 4.4: Teflon® properties.
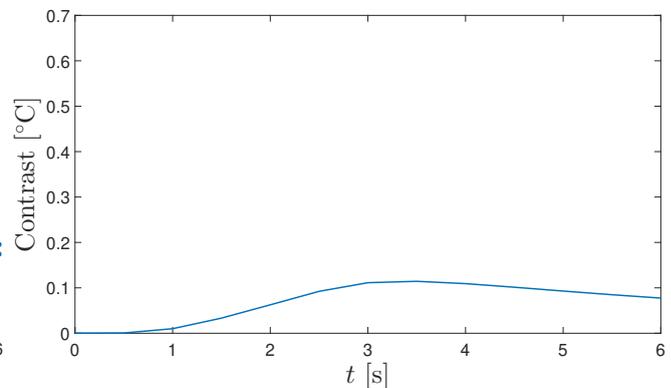
6.1 Thermal analysis

The thermal analysis reveals that the defect impact is rather low in thermography. In Fig. 4.24 the defect is barely visible as well as in Fig. 4.25 with a small difference in the temperature in the defect zone and in the sound zone. It is enhanced by Fig. 4.26 where it can be observed that the contrast has a maximum at about 0.1 °C whereas it is at about 0.6 with the air layer.
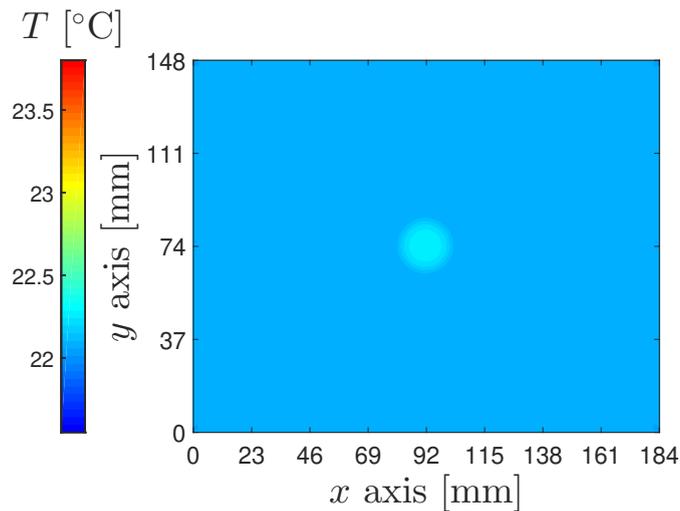
Figure 4.24: Temperature of the upper surface at three seconds with the Teflon® layer.
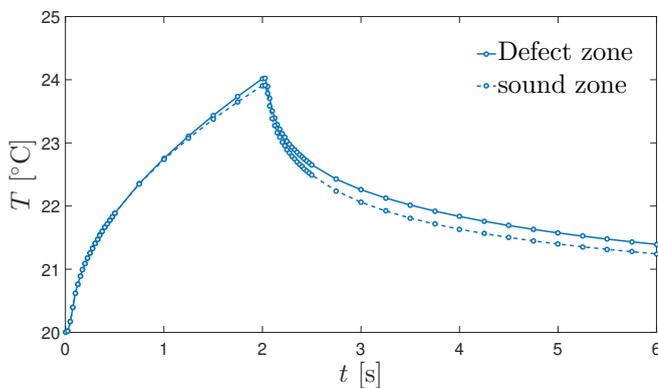
Figure 4.25: Temperature time evolution above the defect and in a sound zone .

Figure 4.26: Thermal contrast evolution with the Teflon® layer.

6.2 Mechanical analysis

By contrast to the true delamination or the air insert, the Teflon® insert shows a huge response in terms of displacements. This can be seen in Fig. 4.27, the defect effect is very well discernible. In Fig. 4.28, the derivatives also exhibit a tremendous impact of the defect and it translates by a phase diagram in Fig. 4.29 with a very visual defect impact. In the phase diagram, fringes seem impacted by the defect but inside the defect zone, non-physical results appear. Indeed, many phase jumps arise inside the defect zone (inside the "crescent moon shape").

This spurious effect comes most probably from numerical errors. In fact, the phase diagram

is obtained by deriving the displacement field, which is obtained from an interpolation of the primary numerical solution. The interpolation could have led to amplifying solution errors that are not visible directly on the displacement field in Fig. 4.27 but small variations directly impact derivatives computation. In all cases, the displacements should not be as high in the defect area (relative to the global deformation).

In any case, a deeper study should be envisaged to validate this model. In the future, a comparison to experimental results could give a better understating to improve the model.
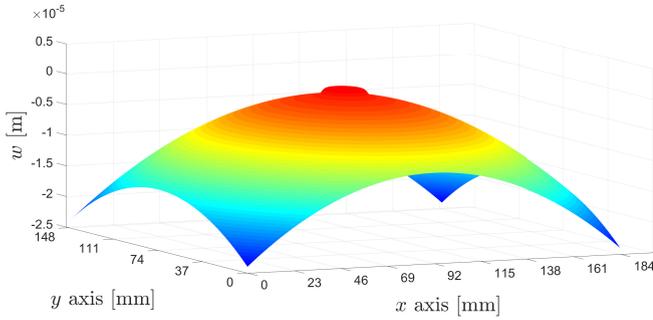
Figure 4.27: Displacements,w, of the upper surface at 3 seconds.
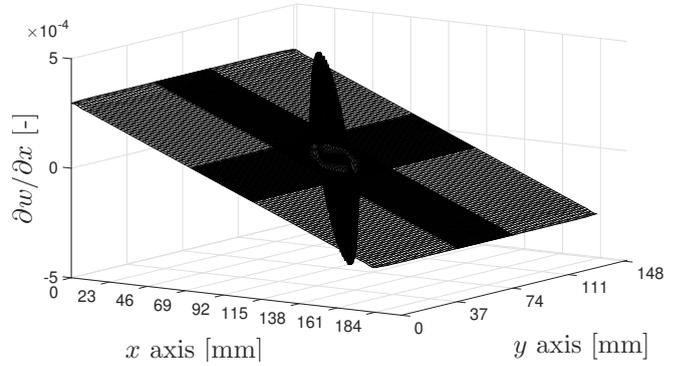
Figure 4.28: Displacement derivatives along x,$\partial w/\partial x$, of the upper surface at 3 seconds.
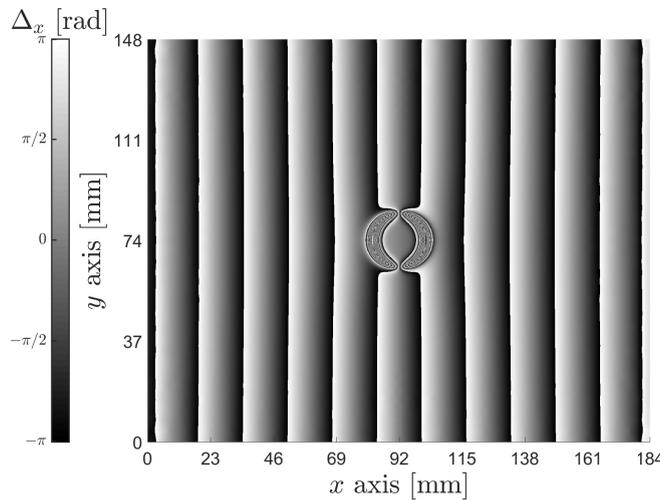
Figure 4.29: Phase diagram,Δ_x, at 3 seconds. Shear: $\delta x = 0.005$ m.

6.3 Conductivity effect

As described above, different thermal conductivity is investigated, its influence is studied here. Thermal conductivity around the one given in Tab. 4.4 is envisaged. Actually, 9 values of k_t are taken in $[0.1;0.5]$ W/(m K) linearly spread. The effect of this variation is seen in the thermal contrast graphic in Fig. 4.30.

The maximum contrast is plotted as a function of the thermal conductivity in Fig. 4.31. Note that the maximum contrast does not arise, especially at the same time. Obviously, as given
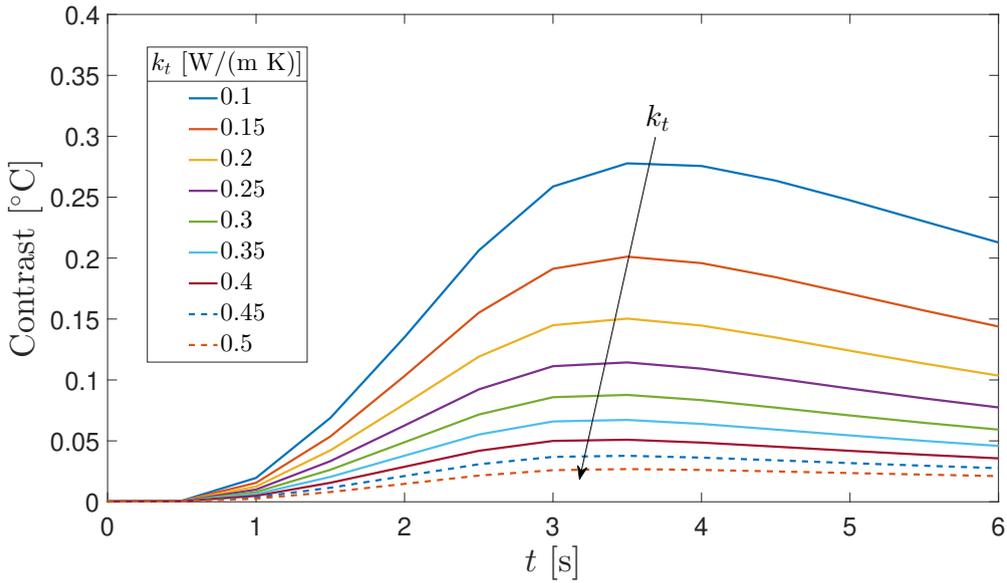
Figure 4.30: Thermal contrast with different thermal conductivity values of the added Teflon® layer.

in Fig. 4.30 the contrast decreases with k_t increasing. If inserts with too high conductivity are used, the detection might be complicated. Even with low conductivity, the contrast stays rather low. The lowest value $k_t = 0.1$ W/(m K), is still one order of magnitude above the air thermal conductivity ($k_a \sim 0.003$ W/(m K)).
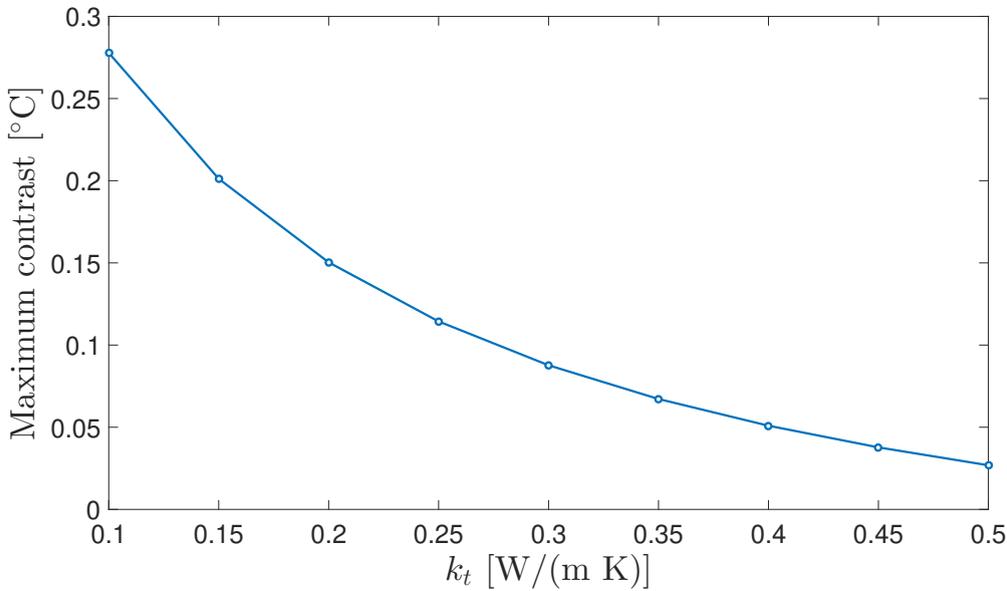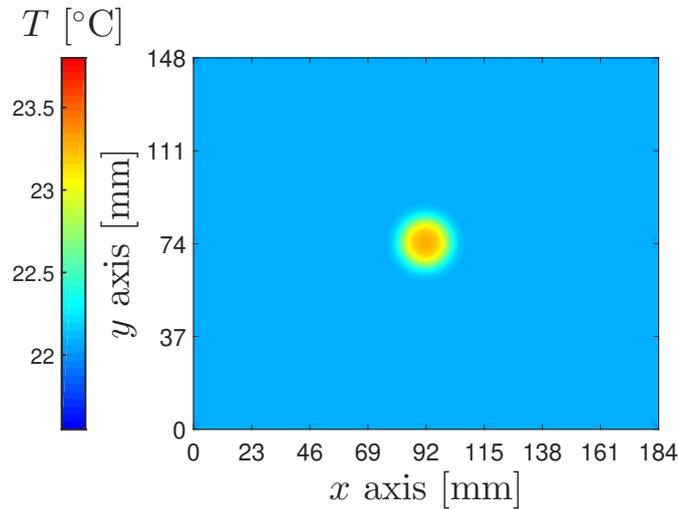

Figure 4.31: Maximum contrast evolution with the Teflon® thermal conductivity.

7   Flat bottom hole

The last model of delamination is the flat bottom hole. It is very common to use this basic model because it is easy to control the depth, size and location of the delamination. The model and the mesh have already been shown in Fig. 4.4. For all models, a defect at 1 mm below the surface has been dealt with. In this section, a study of the depth impact is also performed.
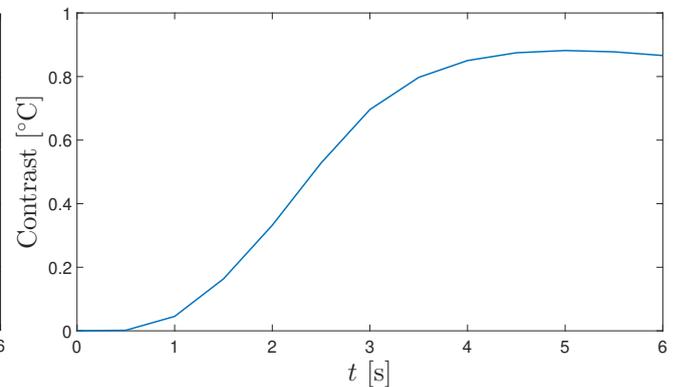
7.1 Thermal analysis

The thermal analysis reveals a behavior quite close to the true delamination model with the interface conductance k'_1. This can be seen in Fig. 4.32, Fig. 4.33 and Fig 4.34. The hole blocks the temperature penetration and a region above the defect gets warmer compared to a sound zone. In fact, the hole is the same as an air layer of infinite thickness or similar to the interface contact modification with $k' = 0$ W(m^2 K).

Figure 4.32: Temperature of the upper surface at three seconds with the FBH model.
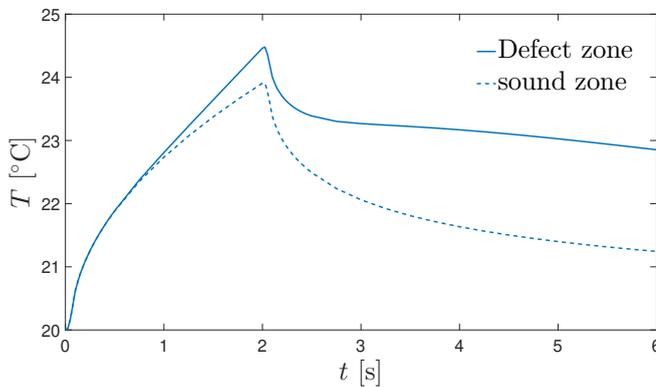
Figure 4.33: Temperature time evolution above the defect and in a sound zone.

Figure 4.34: Thermal contrast evolution with the FBH.

7.2 Mechanical analysis

As for the true delamination or the air layer model, displacements in Fig. 4.35 are continuous and it is hard to distinguish the defect. It should require to inspect Fig. 4.36 or Fig. 4.37 to see the impact. Once again, it is visually very close to the true delamination model (considering k'_1). The fringes in the phase diagram are well locally modified due to the defect presence.
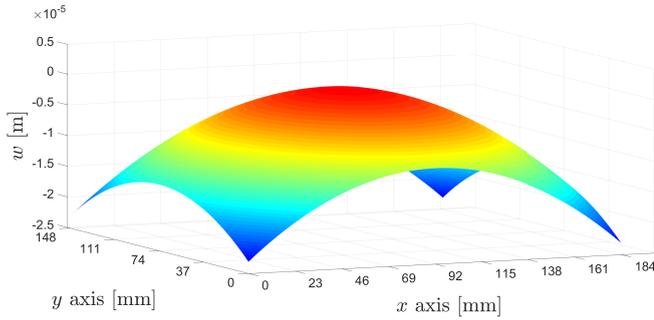
Figure 4.35: Displacements,w, of the upper surface at 3 seconds.
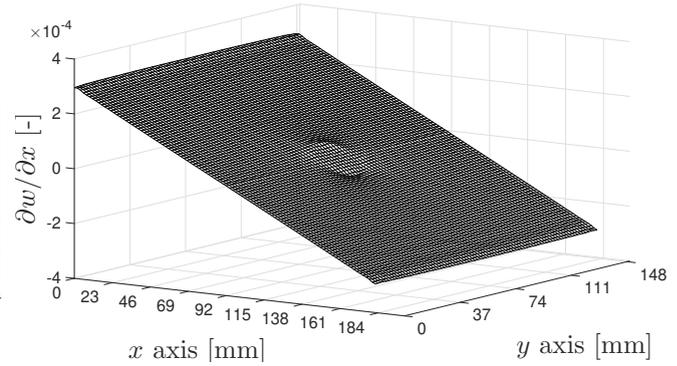
**Figure 4.36:** Displacement derivatives along $x,\partial w/\partial x$, of the upper surface at 3 seconds.
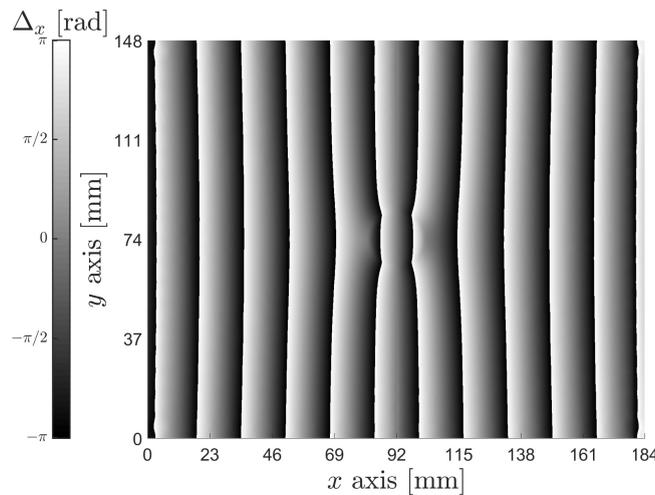


Figure 4.37: Phase diagram,Δ_x, at 3 seconds.

7.3 Defect depth

In industry, one important point is to assess which defects of which size and depth are detectable.the variation in depth is inspected going from $t_d = 0.5$mm to $t_d = 3.5$mm with an increment of 0.5 mm (t_d is defined in Fig. 4.2 and is the defect depth). Only the depth is studied here; hence the size of the defect is kept constant. In the same way that the study of thermal conductivity effect on the physic inserts, the thermal contrast is exposed in Fig. 4.38. Of course, the contrast decreases with the depth of the defect increasing but for depth higher than ~ 2 or~ 2.5 the contrast is very close to zero. Furthermore, the contrast is the highest around 20 seconds for those depths, meaning that a lot of time must be waited to detect a defect potentially. In fact, it is quite logical as the temperature diffusion takes more time to reach the defect for deeper ones.

To better see the effect of the defect depth, the maximum contrast evolution is shown in Fig. 4.39. It is seen that the contrast tends to zero, which is an expected outcome. Also it drops quickly between $t_d = 0.5$ mm and $t_d = 1.5$ mm.
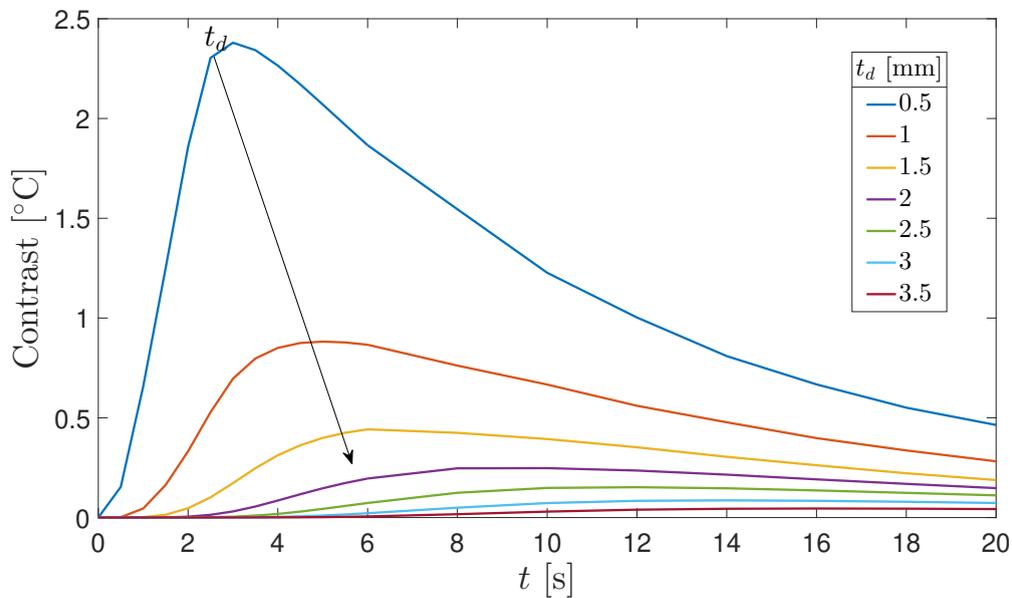
Figure 4.38: Thermal contrast with different depth of the defect.
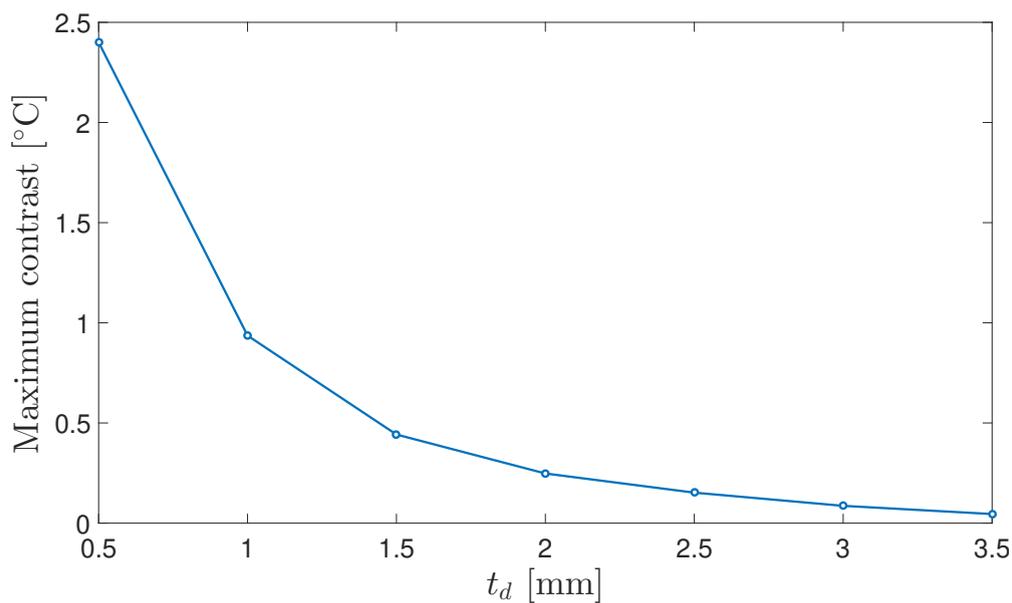
Figure 4.39: Maximum contrast evolution with defect depth.

5

Porosity models

Porosity is probably one of the most common defects in laminates. Unfortunately, shearography is generally poorly adapted as the defect size is too small and too widespread in the material [18]. However, thermography might be a good option to highlight this type of defect. Tools developed in thermography in chapter 2 in combination with numerical models representing porosity will be considered in this chapter. A model representing true porosity would be very complicated as it would ask to represent all voids in the laminate. Therefore an equivalent model is investigated with some small flat bottom holes concentrated in a particular region. This type of model is used in some industries but is criticized by some others.

1   Equivalent porosity models

The equivalent model is based on flat bottom holes of small diameters done locally within the material with different depths. The number of flat bottom holes can also be adapted to change the porosity level. A model is presented in Fig. 5.1 based on a sample available for experimental testing. The porosity is modeled by a 5 by 5 matrix of flat bottoms holes with variable depths of 25, 50 and 75 % of the thickness equally but randomly distributed. This kind of porosity model is not yet well implemented in the NDT world, especially the aerospace field's main actors (Airbus, Boeing, etc.). The size of the holes is considered too large in comparison with typical porosity. Works are in progress to building new models or achieving smaller hole diameter by machining or by laser (S. Hoffait, private communication, 2021).

This model contains a zone representing about 27 % of an apparent porosity level in the zone of the holes computed as follow:

$$\text{taux}_p = \frac{V_v}{V_t} = 27\%, \tag{5.1}$$

with V_v the volume of void and Vt the volume if no porosity was present (in the porosity zone). The apparent level of porosity is far from the equivalent level, which is not easy to define. Based on the fall of the background echo of an ultrasonic beam (Servais P., private communication, June 2021), some techniques enable its determination but are out-of-scope. In the majority of cases, a behavior equivalent to 2% of porosity is sought.

2   Mesh and material properties

Materials properties are to be defined. Only a thermal analysis is performed, so the only properties needed are density, thermal conductivity and specific heat. Unfortunately, no information is provided with the sample the modeling is based on. The material is then considered to be constituted of a UD plies with the stacking sequence $[0/90]_{11}$. The other properties are summed up in
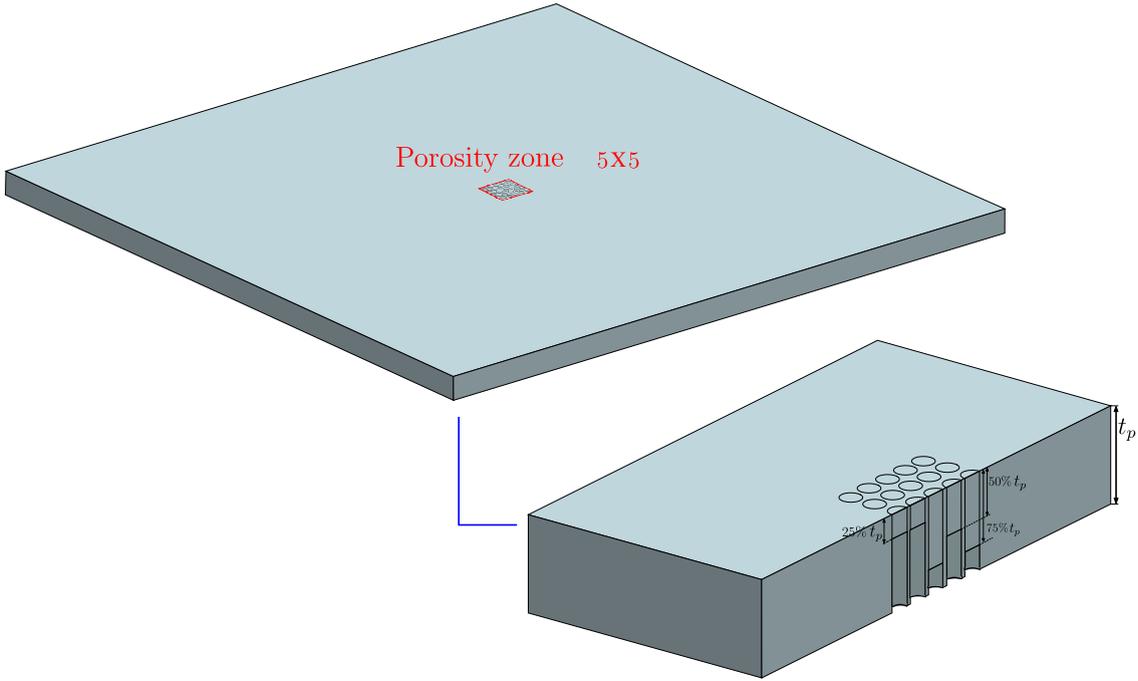
Figure 5.1: Equivalent model with a porosity zone.

Tab. 5.1. In opposition to the delamination model where the plies properties of the laminate are considered symmetric in x and y, here the UD assumption suggests that the transverse direction properties (along y and z) are the same. Once again, typical values from [40] are used.

Property	Units	Value
Density	[kg/m^3]	$\rho = 1503$
Specific heat	[J/(kg K)]	$c_p = 1200$
Thermal conductivity	[W/(m K)]	$k_x = 7$
		$k_y = k_z = 0.8$

Table 5.1: Material properties of a ply in the stacking sequence $[90/0]_{11}$ in the scope of the porosity model. Properties are given in orthotropic axes.

Mesh is generated in Fig. 5.2 with more refined mesh in the porosity zone and one element per ply along with the thickness. Bricks elements with additional mid nodes are chosen as for the delamination model.
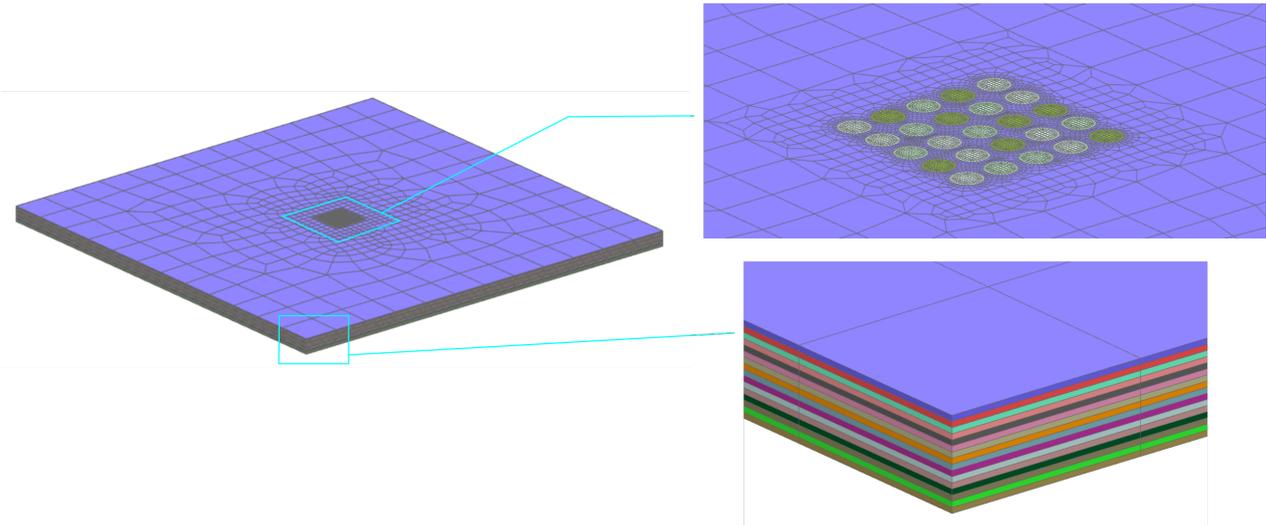
Figure 5.2: Mesh for the porosity model.

3 Thermal excitation

The thermal excitation is still investigated to represent the reflector that implies a radiative flux at the surface of the sample tested. The flux value, $q''_{\mathrm{rad_{heat}}} = 3000$ W/m^2, is still guided by the view factor computation in section 3.1.3 in chapter 3. Moreover, the shape of the flux is still smoothed on the rise and fall of its time evolution, as explained in section 4 of chapter 3. For this model, two types of thermal excitation are tested. By experience, it is known that the response is quite weak with this model of porosity, so that the first case consists of illuminating the upper face for 8 seconds with a flux intensity equal to $q''_{\mathrm{rad_{heat}}}$. For the second case, a pulse shape is explored. The same amount of energy is supplied to the system but over a very short interval of 0.2 seconds. The shape of the excitations in both cases is shown in Fig. 5.3.
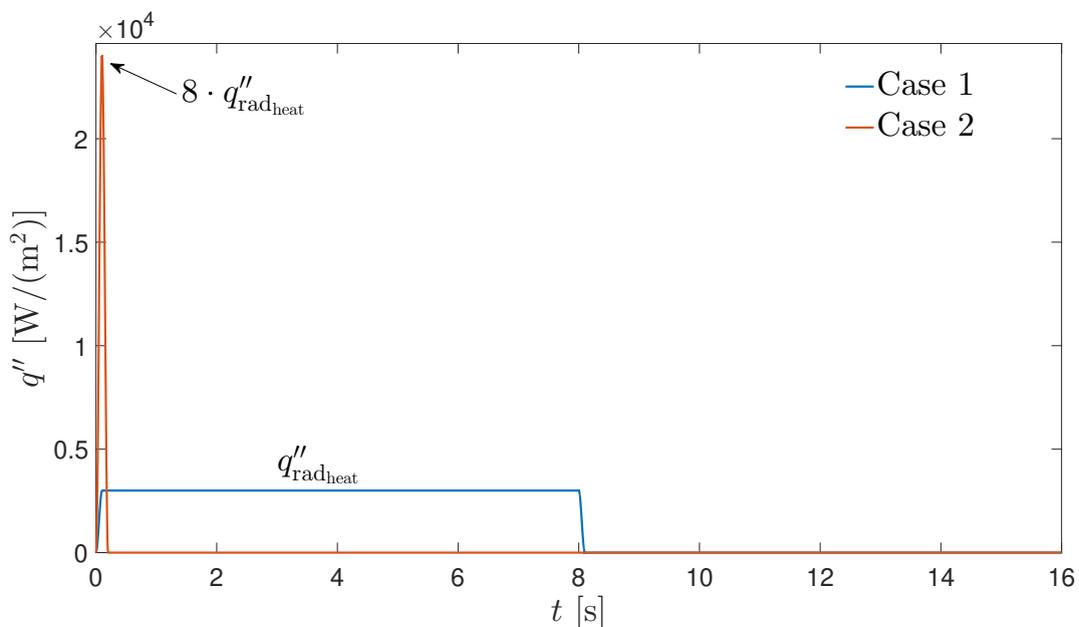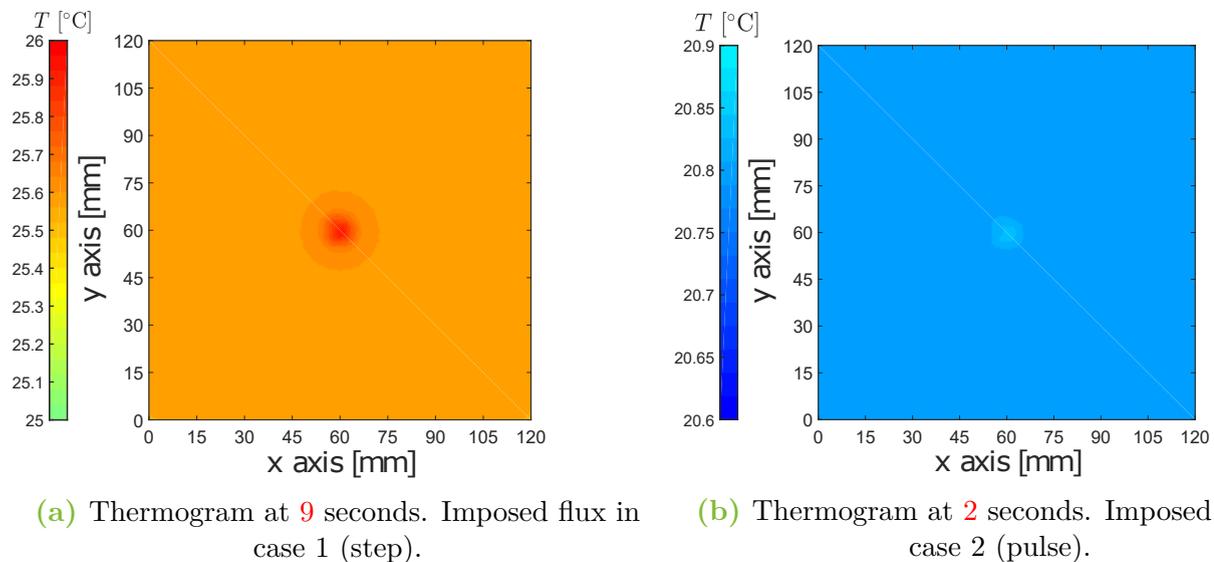

Figure 5.3: Thermal fluxes imposed in simulations.

4 Simulations

Simulations with the radiative fluxes described in the previous section and with the Crank-Nicolson scheme using adaptive time steps as described in section 4 (chapter 3). The solution is obtained from zero to 16 seconds and the two cases of flux loads are directly compared side to side.

First, the thermograms are analyzed in Fig. 5.4. For both cases, the porosity zone is clearly visible but it is essential to mention that the scale has a very small range. This means that the contrast is not so high, especially for the thermal excitation case 2. The thermograms are not taken at the same time because of the shape of the excitation. In experimental tests, it could be easy to miss them as the scale could not directly be as well adapted as it is done in Fig. 5.4. Furthermore, noise is present in experimental data, and if the contrast is comparable to the noise, no conclusion could be made on the detection.

(a) Thermogram at 9 seconds. Imposed flux in case 1 (step).

(b) Thermogram at 2 seconds. Imposed flux in case 2 (pulse).

Figure 5.4: Thermograms obtained with the two cases of imposed flux discussed in Fig. 5.3.

Then, the time evolution of the temperature in the defect zone and a sound zone is observed in Fig. 5.5 for the two cases of flux considered. The temperature in the defect zone is the mean temperature in the porosity zone in Fig. 5.1 (taken only at the surface as always). The temperature in the sound zone is taken at a point in the corner of the top surface. The contrast is shown in Fig. 5.6 again for both cases of thermal excitation. In case2, the difference in the sound zone and the defect zone is very small, confirming that it could be challenging to detect the defect in practice. To detect the defect with a thermal pulse, it would maybe require a higher energy pulse.

The techniques described in section 4 in chapter 2 can be used to enhance the detection. The sequence of thermograms is taken with a time step of 0.5 seconds. The phase, φ, obtained with the pulse phase thermography (PFT) and the first empirical orthogonal (EOF 1) with principal
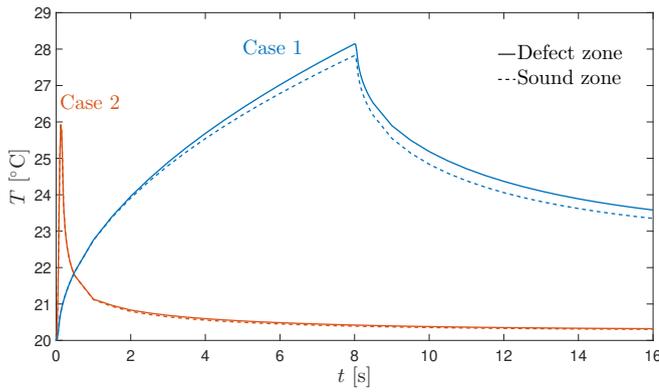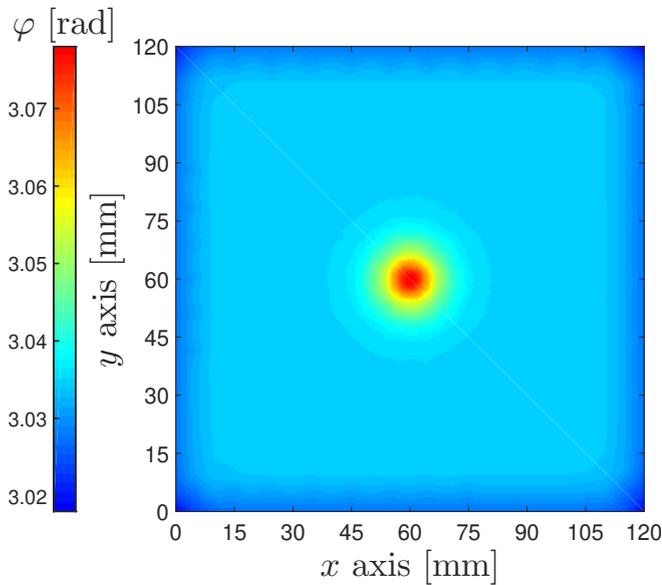
Figure 5.5: Temperature time evolution in the defect zone and in the sound zone for the two cases of imposed fluxes considered.
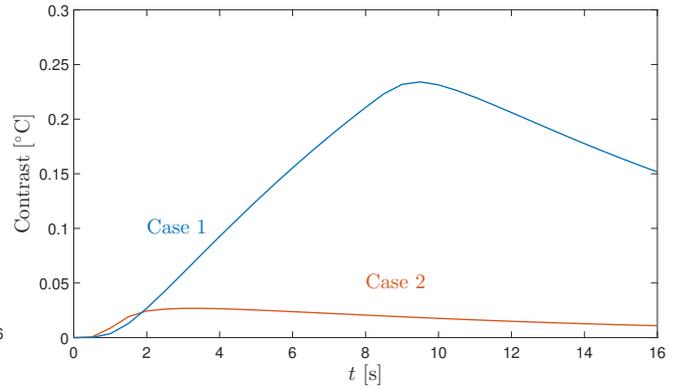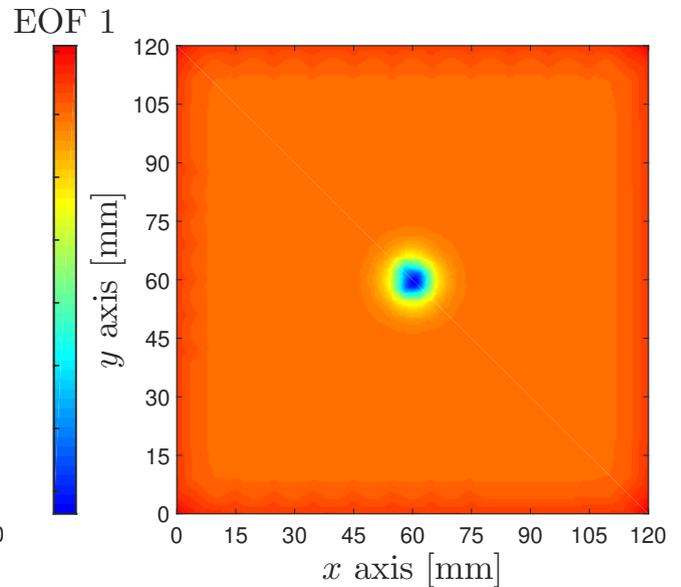

Figure 5.6: Thermal contrast evolution for the two cases of imposed fluxes considered.

component thermography (PCT) are shown in Fig. 5.7 and Fig. 5.8 respectively. It shows that the defect is highlighted and clearly identifiable.

Figure 5.7: Phase (φ) at 0.097 Hz obtained with PFT method.

Figure 5.8: Empirical orthognoal function 1 (EOF 1) obtained with the PCT method.

6

In order to validate simulations, they are compared to experimental results. It is an important process as numerical results are often based on simplifications and assumptions that may not lead to physical results. The experimental approach brings tools to understand better what happens in reality. Nevertheless, it is often affected by measurement errors. Interpreting and comparing numerical and experimental results is a crucial step that must be carried out with a critical mind. Firstly, the samples tested will be presented even though some small glimpses of them have already been delivered. Two samples with flat bottom holes as a delamination model and a sample with zones of simulated porosity are reviewed. The set-ups in thermography and in shearography are then presented. Finally, a comparison and a correlation of results are achieved.

1   Samples

Three samples will be tested, two with one flat bottom hole and one with a network of flat bottom holes to represent porosity. The former two were the basis for simulations in chapter 4 and the last was the model on which the simulations in chapter 5 were based. They will be identified by the name "sample FBH$_{\mathrm{free}}$", "sample FBH$_{\mathrm{clamped}}$" and "sample POR". They are presented in Fig. 6.1, Fig. 6.2 and Fig. 6.3.

Important remark: the two samples with one FBH differ by the boundary conditions but, moreover by the depth of the defect. Sample FBH$_{\mathrm{free}}$ has a defect depth (t_d) of 2.5 mm while for FBH$_{\mathrm{clamped}}$ it is 1 mm. The defect depth is the distance between the plain surface and the top of the defect and should not be confused with the depth of the hole.

All samples will be tested in thermography with an infra-red camera and only the first two will be tested in shearography. The reason is that for porosity, shearography comes to be poorly adapted according to [18].

2   Experimental set-up

Two set-ups are discussed here, one for thermography and one for shearography. However, in both set-ups, the external heater is the same and placed at the same distance of samples. The heater used is an infra-red heater of 1300 W as seen in Fig. 6.4.
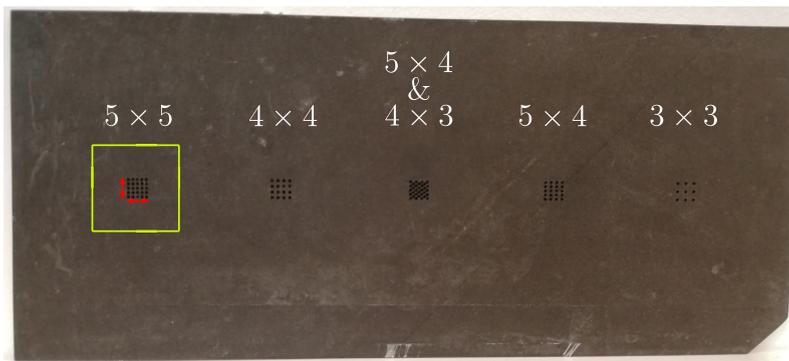
2.1   Thermography

The set-up is presented in Fig. 6.5 with the sample FBH$_{\mathrm{clamped}}$ as an example but the set-up is quite the same for the two others. Black sheets are used to eliminate a maximum of reflection that would perturb the camera. The camera is tilted slightly downwards because if it is set up
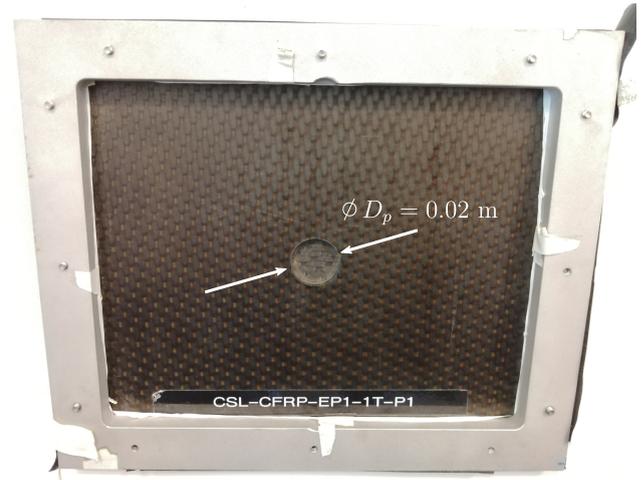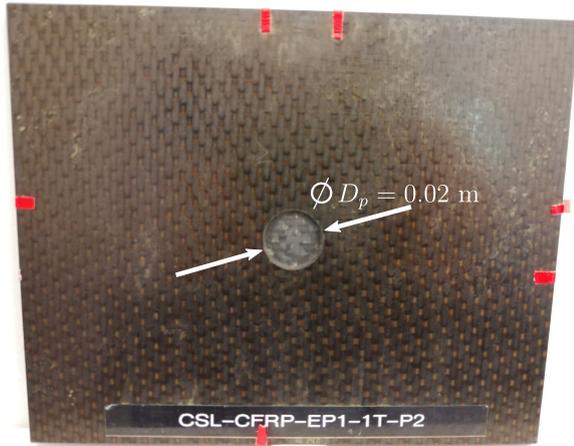
Figure 6.1: sample FBH$_{\text{free}}$ ($t_d = 2.5$ mm)

Figure 6.2: sample FBH$_{\text{clamped}}$ ($t_d = 1$ mm)

Figure 6.3: sample POR

Figure 6.4: Infra-red heater of 1300 W.

perpendicularly to the sample, reflections of the objective itself would appear. Regarding sample FBH$_{\text{free}}$ and POR, they are not laid on the table like sample FBH$_{\text{clamped}}$ in Fig. 6.5. Sample FBH$_{\text{clamped}}$ is laid that way because of its frame that is present whether it is tried to insulate the sample from the environment or not. Fig. 6.6 shows how sample FBH$_{\text{free}}$ or POR are placed in the set-up taken the example of sample FBH$_{\text{free}}$. Some insulator pieces are employed to isolate the sample from its support. The camera used is a `XENICS GOBI-PLUS-640-17-50-GE`, the data-sheet is given in [44].

2.2 Shearography

The set-up is basically the same, the difference is the camera and the fixation of sample FBH$_{\text{free}}$. It is observed in Fig. 6.7 with sample FBH$_{\text{free}}$. Bear in mind that only samples FBH$_{\text{free}}$
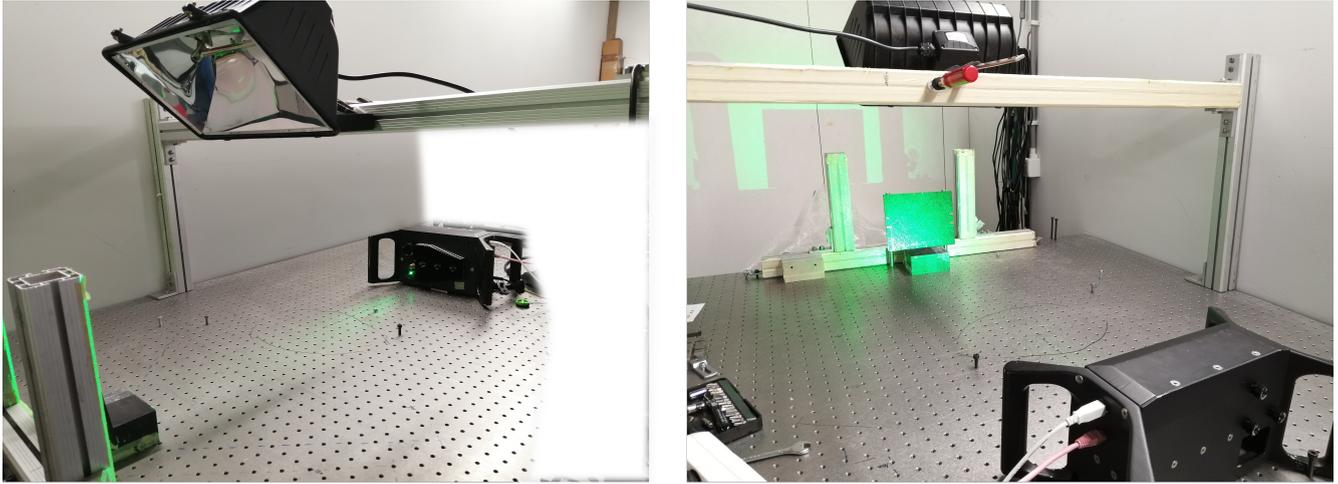
Figure 6.5: Experimental set-up in thermography. Example with the sample FBH$_{\text{clamped}}$.


Figure 6.6: Set-up of sample FBH$_{\text{free}}$ and 3, sample FBH$_{\text{free}}$ is shown but the same set-up is used for the sample POR.

and FBH$_{\text{clamped}}$ are tested in shearography and that fixations of these samples were previously introduced in Fig. 3.8. The camera for shearography combines the laser emitter and the camera receiving back the information. It is positioned as perpendicular to the sample as possible to be as close as possible to having a sensitivity vector lying along with the sample normal. This is essential to measure the displacements along z (w, in other words) as explained in section 3.2.3 of chapter 2.

In shearography, a value of shear must be set up. This is done using a reference frame and a reference mark as illustrated in Fig. 6.8. The value is chosen to 5 mm in the x direction, ($\delta x = 0.005$ m).

Figure 6.7: Shearography experimental set-up with sample FBH$_{\text{free}}$ as example.
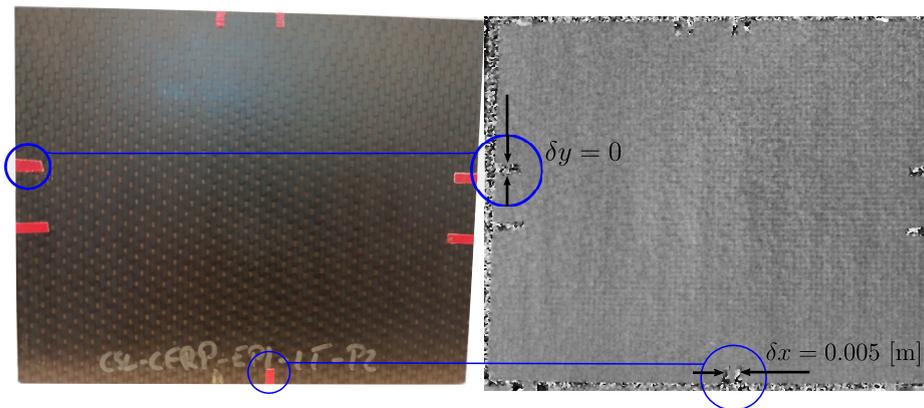
Figure 6.8: Definition of the shear thank to a reference frame.

3 Comparison and correlation

Now that set-ups have been exhibited, measures and comparisons with numerical simulations are performed.

3.1 Sample FBH$_{\text{free}}$

This sample is tested both in thermography and shearography. For the two tests, the same thermal excitation is imposed. **The lamp is switched on for 8 seconds**, this choice is made because simulations described in chapter 4 revealed that for a defect depth of 2.5 mm (case of sample FBH$_{\text{free}}$) a heat stimulation of 2 seconds leads to low contrast. Therefore, a simulation with a thermal excitation of 8 seconds and keeping all other parameters unchanged is launched.

3.1.1 Thermography

Results obtained experimentally are presented and directly compared with numerical simulations. At first, the thermograms are compared in Fig. 6.9 at 15 seconds. The first thing to notice is that the experimental thermogram seems to be around 21 or 22 °C (in the light blue region),
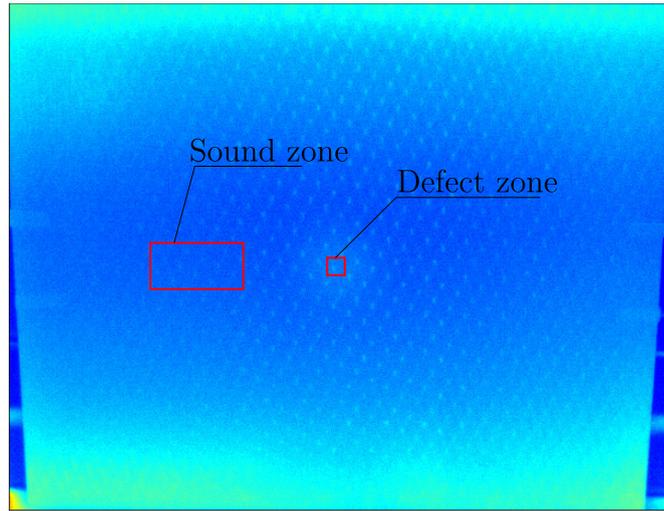
(a) Experimental result.

(b) Simulation result.
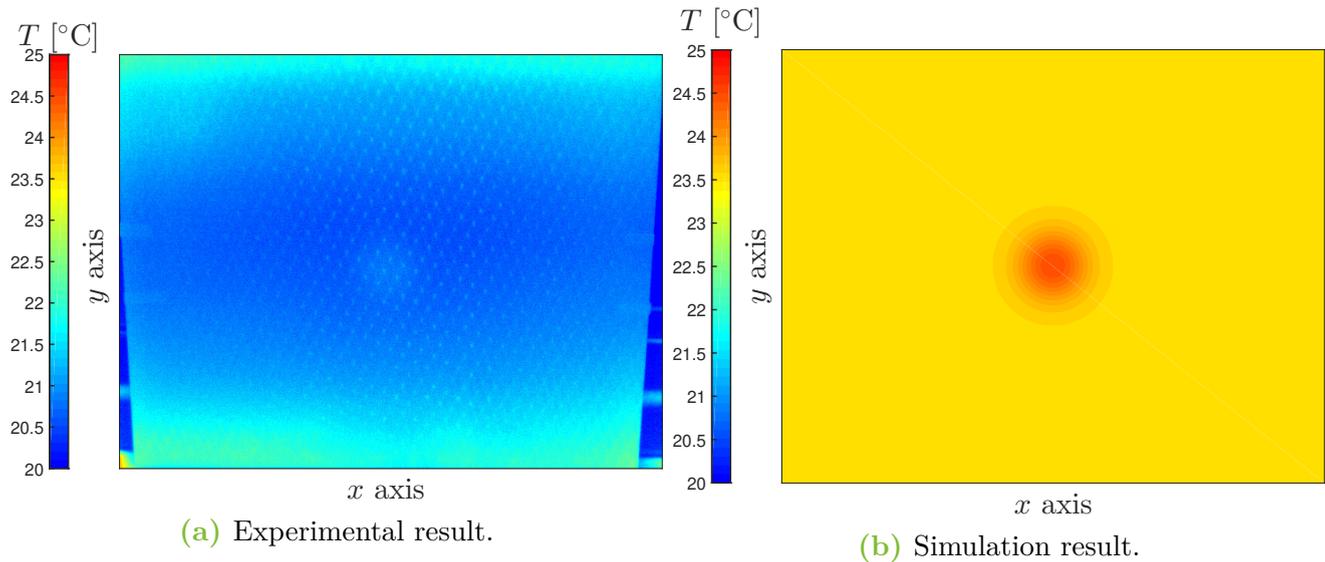
Figure 6.9: Comparison of experimental and numerical simulation thermograms at 15 seconds with sample FBH$_{\text{free}}$.

whereas the one from simulations is around 23 to 24°C (yellow region). This means that the value of imposed flux by the heater overestimates the real flux emerging from the heater. The second observable phenomenon is the two green bands up and down in Fig. 6.9a, suggesting that the heater does not produce a uniform flux on the surface. This was expected but now it is confirmed and is most probably one reason for the overestimation of the flux.

Thermograms have been shown at 15 seconds because the contrast is maximum at this time. A look at the time history of the temperature in a sound zone and the defect zone in Fig. 6.11 shows this pattern. In addition, the contrast in Fig. 6.12 confirms this. In simulations, the temperature in the defect zone is easily represented by the temperature of the central point and the temperature in a sound zone by the temperature at any corner. Experimentally, the temperature is represented by an average in the defect zone and a sound zone. The sound zone choice is nevertheless not trivial and very result-impacting. In view of the non-uniform temperature distribution, the sound zone is taken not too far from the defect zone and on the same horizontal axis as shown in Fig. 6.10.

Results of Fig. 6.11 reinforce the idea that the imposed flux is overestimated in simulations. On the other hand, the shape looks very similar in simulations and experimentally. Regarding the cooling part (after 8 seconds), the temperature in simulation decreases more sharply than experimentally but as the temperature reaches higher values, the convection and radiation fluxes are also higher. In Fig. 6.12 and below 2 seconds, the contrast is negative, which may be due to measurement errors. At 0 seconds, the plate is supposed to be ideally at a uniform temperature but it is never perfectly the case (results of previous experiments, for instance). Otherwise, the contrast seems to match the simulations between 2 and 8 seconds but is then fading. It may be explained by the fact that, experimentally, the temperature rises to lower values leading to less

Figure 6.10: Zone definition for experimental results on sample FBH$_{\text{free}}$.
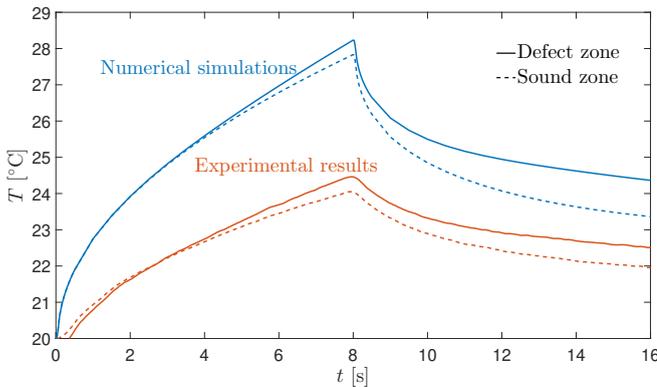
Figure 6.11: Comparison of temperature time evolution in the defect and a sound zone between experimental and simulation results on sample FBH$_{\text{free}}$.
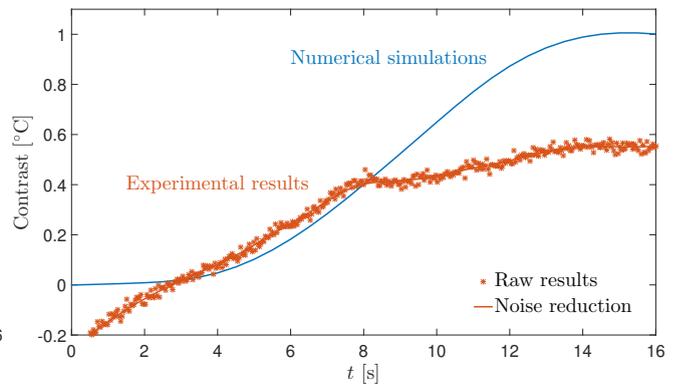
Figure 6.12: Comparison of contrast evolution of experimental and simulation results on sample FBH$_{\text{free}}$.

energy accumulating in the defect zone.

3.1.2 Shearography

Phase diagrams obtained experimentally and numerically are compared in Fig. 6.13. In both cases, the defect is visible. In experimental results, fringes do not appear perfectly symmetric but still fairly. It may translate to a slight asymmetry of the material properties. Furthermore, compared to numerical results, fringes are not straight, especially at the border. Remember when talking about materials properties, it has been said that the laminate does not have a symmetric stacking sequence. As long as properties are symmetric in x and y, it does not imply coupling between in- and out-of-plane effects. If in reality, these properties are not really as symmetric as thought, couplings may arise.

However, it is to be observed that the number of fringes is very similar in the two approaches. Clearly, six jumps from $-\pi$ to π are observed in simulation and almost 6 with experimental results. Nearly six because a small white region to the left in Fig. 6.13a can be seen. It means that globally,

the displacement derivative has the same order of magnitude. The non-uniformity of heating in the experimental part is a significant factor in the difference observed. In addition, the uncertainty on material properties certainly plays a role too.

(a) Experimental result.

(b) Simulation result.
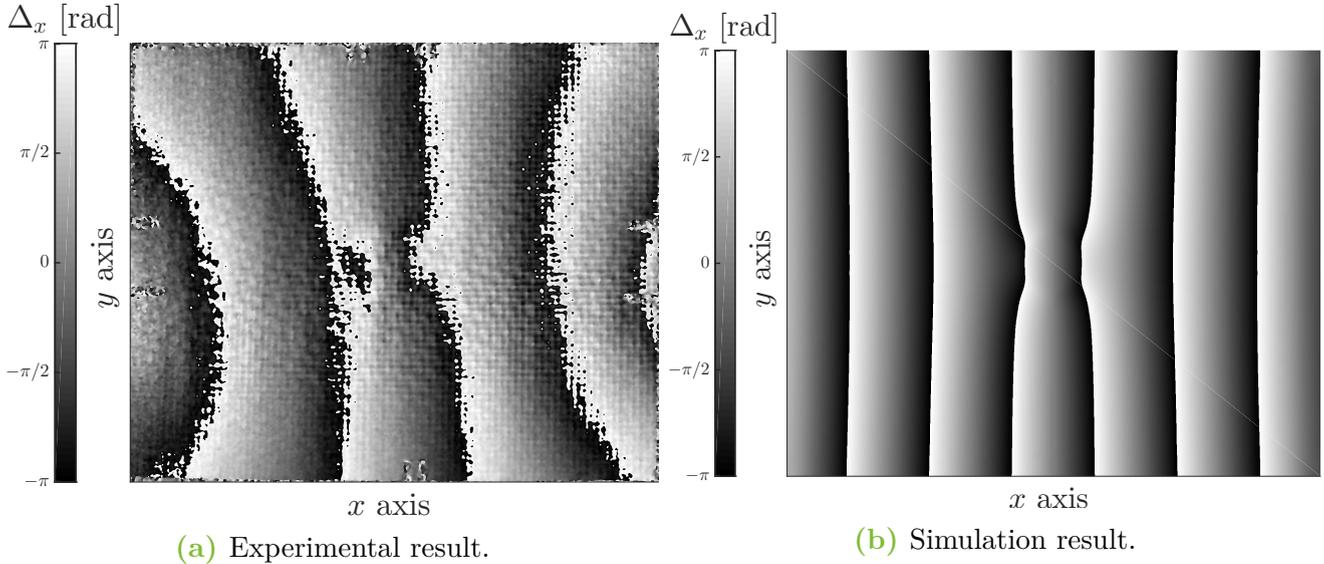
Figure 6.13: Comparison of experimental and numerical simulation phase diagram at 15 seconds with sample FBH$_{\text{free}}$ ($\delta x = 0.005$ m).

3.2 Sample FBH$_{\text{clamped}}$

This sample is almost the same as sample FBH$_{\text{free}}$, the boundary conditions change as edges of sample FBH$_{\text{clamped}}$ are clamped. On top of that, the defect depth is lower, $t_d = 1$ mm against 2.5 mm for sample FBH$_{\text{free}}$. This sample is also tested in thermography and shearography. **The lamp is on for 3 seconds** in this case, the depth being lower, less energy is needed and the contrast remains high enough.

3.2.1 Thermography

As with sample FBH$_{\text{free}}$, the results obtained experimentally and by numerical simulations are compared. Fig 6.14 illustrates the two thermograms at 6 seconds. Basically, the same conclusion as with sample FBH$_{\text{free}}$ can be drawn. The temperature is not homogeneous and is lower in the experimental case. This once again means that the flux has been overestimated in simulations and that the homogeneous flux assumption is not so close to reality. Another point is that the defect is very well visible here, but it is normal since the defect depth is relatively small compared with sample FBH$_{\text{free}}$.

Taking the same sound and defect zone reference as used for the sample FBH$_{\text{free}}$ and defined in Fig. 6.10 (just transposed to sample FBH$_{\text{clamped}}$), the time evolution of the temperature and the contrast can be compared. It is done in Fig. 6.15 and Fig. 6.16. The curve shapes are very similar but the experimental temperatures are still lower when considering experimental results. The big difference with sample FBH$_{\text{free}}$ is that this time, the experimental contrast does not follow the one

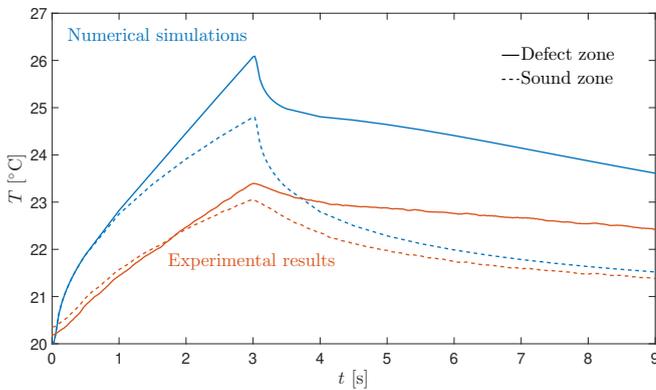(a) Experimental result.
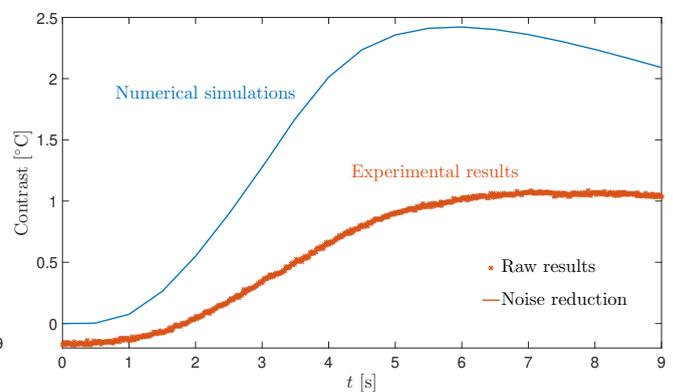
(b) Simulation result.
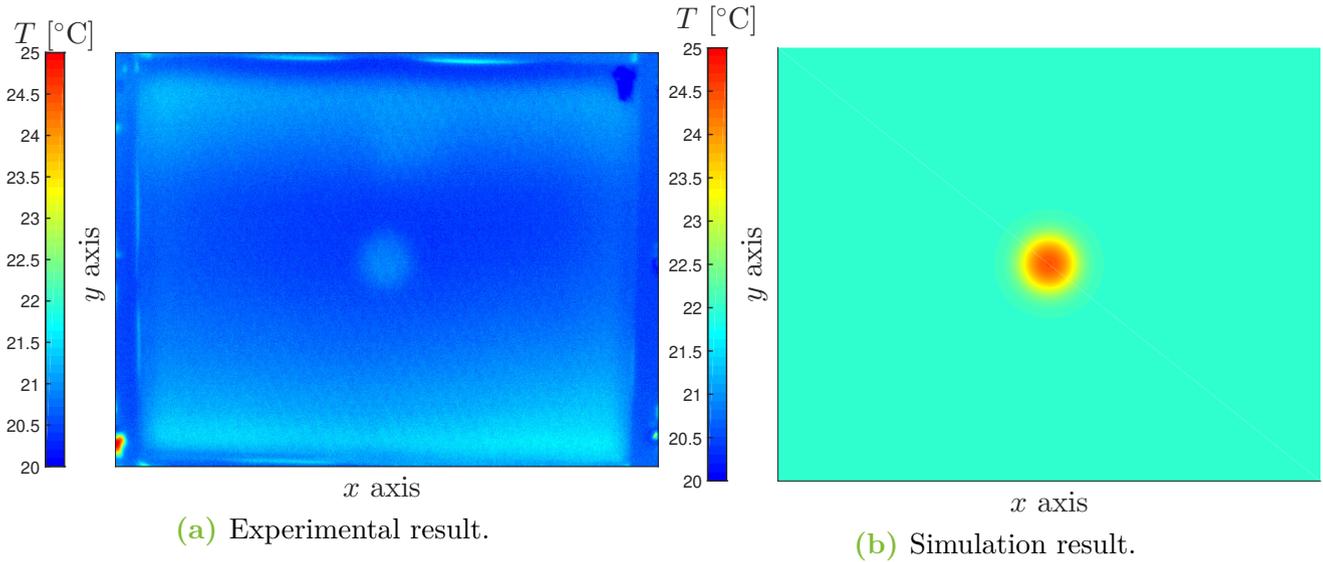
Figure 6.14: Comparison of experimental and numerical simulation thermograms at 6 seconds with sample $\mathrm{FBH_{clamped}}$.

from simulation even during the rise in temperature (with sample $\mathrm{FBH_{free}}$, at least during the rise the experimental contrast was close to simulation contrast). This phenomenon comes once more from the overestimation of the flux imposed in simulations combined with the fact that the depth of the defect is smaller. The sample reaches a higher temperature in simulations, and so more energy accumulates above the defect. As the defect is rather close to the top surface, the difference in temperature in the defect zone and the sound is marked more quickly. On sample $\mathrm{FBH_{free}}$, the defect being deeper, this difference is more hidden. When the lamp is turned off (after 3 seconds for sample $\mathrm{FBH_{clamped}}$), the contrast is still smaller in experimental results. The temperature in the experimental approach reaching a lower temperature, less energy can be accumulated above the defect leading to a smaller contrast.


Figure 6.15: Comparison of temperature time evolution in the defect and a sound zone between experimental and simulation results on sample $\mathrm{FBH_{clamped}}$.

Figure 6.16: Comparison of contrast evolution of experimental and simulation results on sample $\mathrm{FBH_{clamped}}$.

3.2.2 Shearography

Still considering a shear of 5 mm in the x direction, results at 6 seconds are compared in Fig. 6.17. It is clear that there is a difference between both results. In experimental results, some fringes appear, suggesting that the sample bends despite the clamping. In simulations, the only fringes formed are located at the defect, meaning that the sample does not bend elsewhere. Besides that, the number of experimental fringes is relatively low, insinuating that the bending is rather low. In reality, the clamping is perhaps not perfect and out-of-plane displacements come out. The properties could also have poorly been estimated at some points leading to couplings between deformation modes in the composite.

(a) Experimental result.

(b) Simulation result.
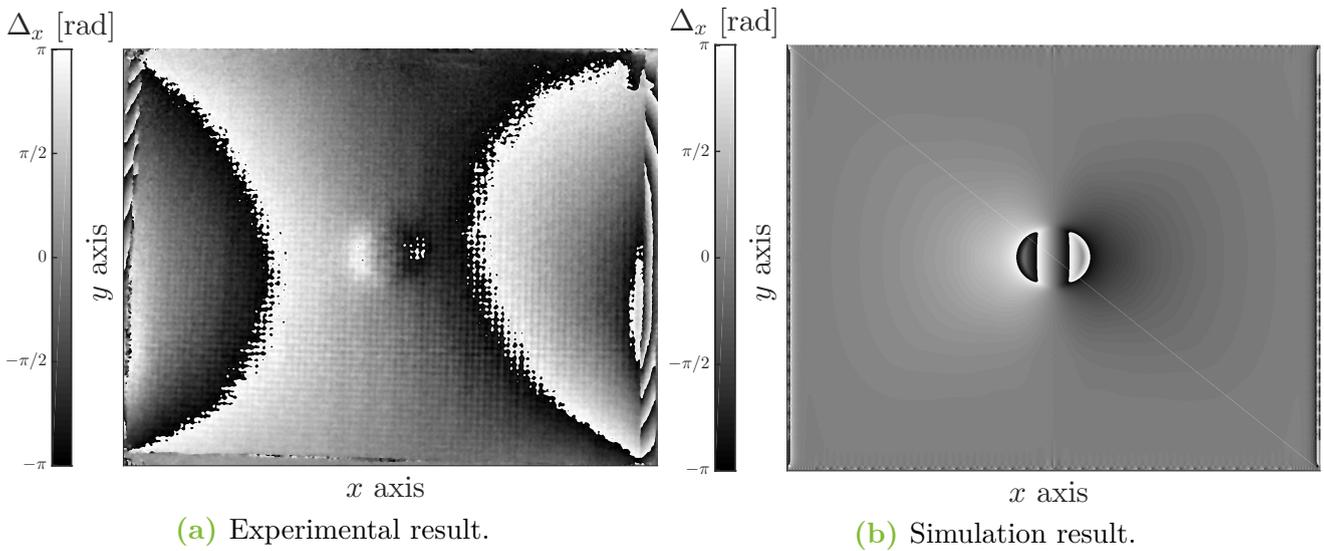
Figure 6.17: Comparison of experimental and numerical simulation phase diagram at 6 seconds with sample FBH$_{\text{free}}$ ($\delta x = 0.005$ m).

3.3 Sample POR

The different zones of porosity are tested at once, and the zone of 5x5 flat bottom holes is compared to the numerical results obtained in chapter 5. The object surface is **illuminated over 8 seconds** which corresponds to the case studied in simulations in section 4 of chapter 5 (particularly to case 1 in this section). Remind that this sample is only tested in thermography.

3.3.1 Thermography

Results are obtained with the set-up described previously and also by simulations. The thermograms at 10 seconds are being analyzed in Fig. 6.18. The sample used in experimental tests has different porosity zones, while in simulations, only one model is studied. With experimental results, it is tough to distinguish the defects. First, the simulated porosity zones do not exhibit a very high response in thermography, even in simulations. Secondly, the non-uniformity of the heating process very much impacts the results in this case. It is seen in Fig. 6.18a, a band at the bottom of the figure that is hotter than the rest of the plate. It leads to temperature distribution

that tends to hide the defects. Of course, in numerical simulations, this is not present as the flux coming from the heater has been supposed perfectly homogeneous. By looking at the scales in Fig. 6.18 , it can also be said that once again, the temperature reached by the plate is lower in experimental results. It results in an overestimation of the flux imposed by the reflector.

(a) Experimental result.

(b) Simulation result (5×5 porosity zone).
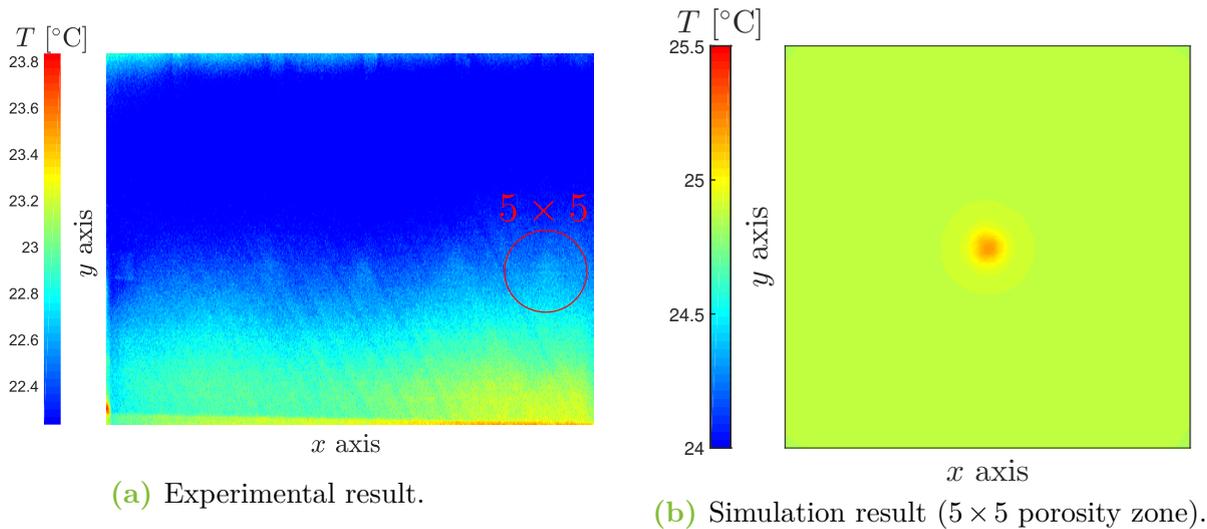
Figure 6.18: Comparison of experimental and numerical simulation thermograms at 10 seconds with sample POR.

For the time evolution of the temperature and the contrast computation, the definition of the sound and defect zones is done in Fig. 6.19. By inspecting Fig. 6.20 and Fig. 6.21, the same conclusion can be drawn. The contrast is shallow and tends to show that results are very variable. The difference in the sound zone and the defect zone is very low, making it hard to conclude the detection of the defect. Moreover, in Fig. 6.21, the experimental results show a very high variance explaining the difficulty of detecting the defect. The noise present in the measurement seems to be as high as the contrast. However, the general allure shows that the experimental contrast increases and reaches its maximum at 10 seconds. Improving the quality of the measures by rather making more uniform the flux from the reflector or decreasing the noise from the acquisition. Note that the non-uniformity induces probably a higher variability in the results. The noise from the acquisition is not something easy to reduce. The only thing feasible is to increase the measure elsewhere to reduce its relative effect.
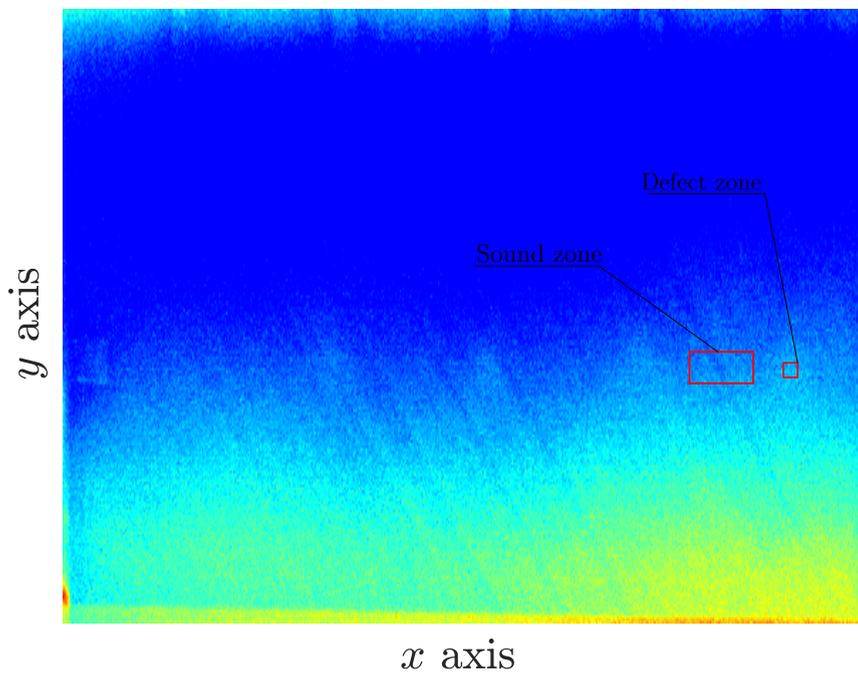
Figure 6.19: Definition of the sound and defect zone for the sample POR.
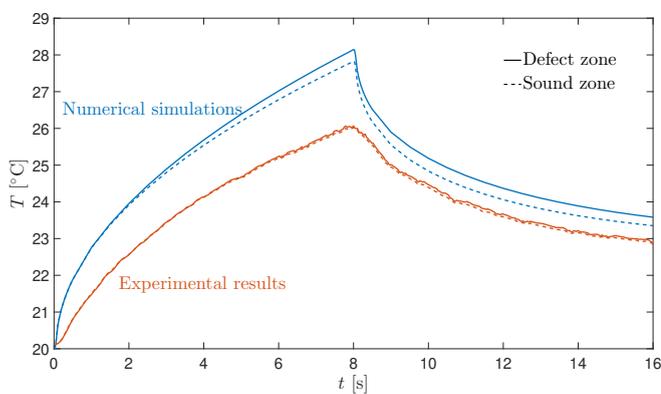
Figure 6.20: Comparison of temperature time evolution in the defect and a sound zone between experimental and simulation results on sample POR.
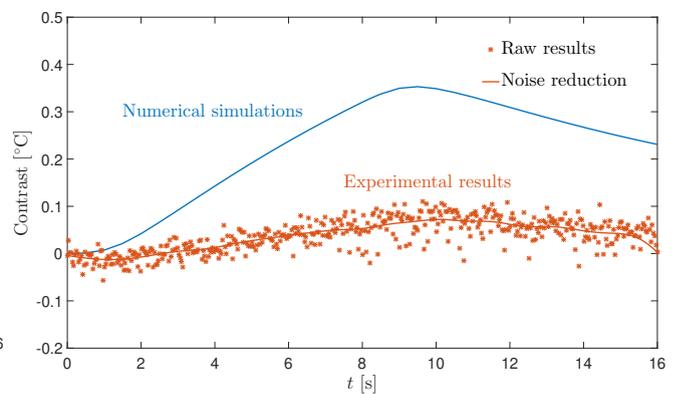
Figure 6.21: Comparison of contrast evolution of experimental and simulation results on sample POR.

7   Conclusion and perspectives

Composites are being produced in larger quantities in the aerospace domain each day. The detection of defects linked to their internal composition is, therefore, a critical preoccupation. Numerical simulations have assisted the improvement of shearography and thermography as non-destructive techniques of detection. Simulations on delamination and porosity models have been implemented to increase the comprehension and the practical realization of defect detection techniques.

After reviewing composites material, their defect and the non-destructive techniques such as shearography and thermography, the prerequisites to numerical simulations have been given. Different numerical models of delamination have been investigated. A model representing true delamination is compared to artificial models that are the physic insert and the flat bottom hole. A porosity model has then been presented and its response to two different thermal excitations has been discussed. The last part was dedicated to the experimental comparison with numerical results. Flat bottom hole models (delamination and porosity) on actual samples have been tested for the comparison.

The two non-destructive techniques used in this work have been investigated with a thermal excitation. The characterization of a lamp was the first significant result, and a methodology for estimating the emitted flux has been developed. The delamination study has shown similarities between the true delamination and artificial models. However, the Teflon insert results in shearography are incoherent with true delamination and with what has been observed in real life. The porosity study has exhibited a small response in thermography. Nevertheless, this model may not be the most representative of the natural porosity. The procedure might also be poorly adapted, especially for the experimental approach. Eventually, the experimental survey with flat bottom hole models has revealed coherent results between the experimental and numerical methods. Nonetheless, discrepancies have been found, notably, the non-homogeneity and the intensity of the flux irradiated by the lamp. The uncertainty on material properties has also caused divergent results.

The characterization of the flux emitted by the heater remains to be improved. The full distribution could be studied by inspecting experimentally a surface receiving all energy irradiated. The mechanical response of the Teflon® layer as a delamination model has to be reconsidered with a more detailed study as the results are questionable. The porosity model still has to be improved because the industry tends to consider that the size of FBHs is too large compared to the actual porosity. Even though equivalent macro responses are observed, they are not convinced of the physical aspect. Other defects or similar detection techniques could be modeled and investigated

with the basis given in this work. With more reliable models, improvements in defect detection could become very significant in the future. Composite materials would therefore become more efficient and used than ever.

Appendix

A.1   Free convection coefficient computation

A method to compute the free convection coefficient, h, does exist ([35], [36], [37]). It implies the knowledge of some dimensionless numbers asking themselves the knowledge of some fluid properties. First, a reminder of the dimensionless numbers is done then the free convection coefficient will be computed on vertical. The plate is generally maintained with the highest area faces vertically.

The Grashof number measures the ratio of the buoyancy force over viscous forces. It is noted Gr_L and is expressed as

$$Gr_L = \frac{g\,\beta\,(T_s - T_\infty)\,L^3}{\nu^2} \tag{A.1}$$

with $g = 9.81$ m/s^2 the gravitational constant, T_s the temperature at the body surface, T_∞ the fluid temperature outside of the boundary layer, L a characteristic length, ν the kinematic viscosity (intrinsic property of the fluid), and finally β known as the volumetric thermal expansion coefficient, its general expression, assuming ideal gas, is (at constant pressure)

$$\beta = -\frac{1}{\rho}\left(\frac{\partial \rho}{\partial T}\right)_p = \frac{1}{\rho}\frac{p}{RT^2} = \frac{1}{T},$$

with p the pressure and R the perfect gas constant.

The Prandtl number, Pr is the ratio of the momentum and thermal diffusivities:

$$Pr = \frac{c_p\,\mu}{k_f} = \frac{\nu}{\alpha_t}, \tag{A.2}$$

where μ is the dynamic viscosity, k_f the fluid thermal conductivity, α_t is the thermal diffusivity.

The Rayleigh number is simply

$$Ra = Gr_L\,Pr. \tag{A.3}$$

Finally, the Nusselt number, Nu_L, is the ratio of convection to pure conduction heat transfer and has the following expression:

$$Nu_L = \frac{h\,L}{k_f}. \tag{A.4}$$

In practice, experimental formulations based on previous numbers are developed, and therefore the convection coefficient can be obtained.

To evaluate all these numbers, some properties must be known, considering air at 293 K ($= T_\infty$), those properties are summed up in Tab. A.1 based on [35]. As properties vary with

the temperature, and the temperature varies in the boundary layer, usually these properties are evaluated at

$$T_{\text{eval}} = \frac{T_s + T_\infty}{2}. \tag{A.5}$$

Taking into account that the temperature T_s varies during the experiment, the maximum value taken is $T_{s_{\max}} = T_\infty + 4$ K, leading to $T_{\text{eval}} = 295.5$ K.

T	ρ	c_p	μ	ν	k_f	α_t	Pr
[K]	[kg/m^3]	[J/(kg K)]	[N s/m^2]	[m^2/s]	[W/(m K)]	[m^2/s]	[-]
295.5	1.182	$1.007 \cdot 10^{-3}$	$1.824 \cdot 10^{-5}$	$1.549 \cdot 10^{-5}$	$2.594 \cdot 10^{-2}$	$2.191 \cdot 10^{-5}$	0.708

T	β
[K]	[K^{-1}]
295.5	$3.384 \cdot 10^{-3}$

Table A.1: Air properties evaluated at $\frac{T_s + T_\infty}{2}$.

A.1.1   Vertical face

Regarding free convection on a vertical face, the first step is to calculate the Rayleigh number because the Nusselt number is generally expressed as a function of this number. The characteristic length is the long side of the plate, the used plate in experiments and simulations is $L = 0.184$ m. Recall that $T_\infty = 293$ K and $T_s = 297$ K, it follows

$$Ra = Gr_L \, Pr = \frac{g\beta \, (T_s - T_\infty) \, L^3}{\nu^2} \cdot Pr = 1.588 \cdot 10^6 \tag{A.6}$$

For laminar flow, $10^4 < Ra < 10^9$, a convenient expression for the Nusselt number is given by [35]

$$Nu_L = 0.68 + \frac{0.670 Ra_L^{1/4}}{\left[1 + (0.492/Pr)^{9/16}\right]^{4/9}} = 18.93 \qquad Ra_L \leqslant 10^9 \tag{A.7}$$

And finally,

$$h = \frac{Nu_L k}{L} = 3.318 \ \ [\text{W}/(\text{m}^2 \ \text{K})] \tag{A.8}$$

In conclusion, the assumption of taking $h = 5$ W/(m^2 K) is not so far from this result but it has to be remarked that the convection overestimates the real flux. In addition, this value is valid when $T_s = T_\infty + 4$ K, it is the highest value of T_s at the surface at the end of the heating process. At any other time, T_s is smaller and the free convection coefficient as well, overestimating again the real flux.
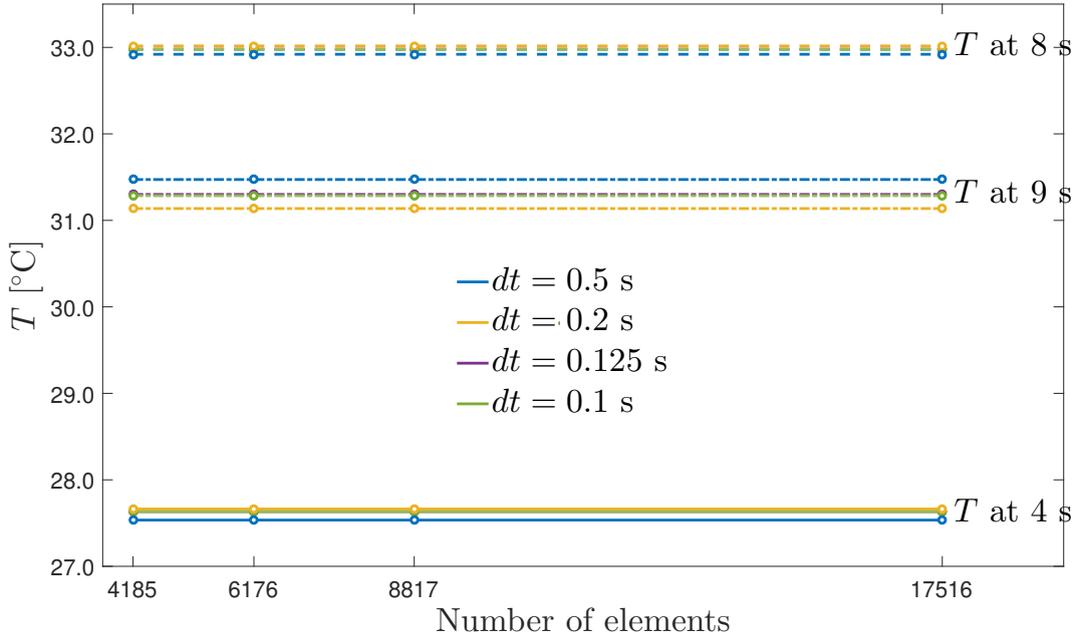
A.2 Convergence

A.2.1 Thermal

The effect of the time step is shown in Fig. A.1. Oscillation almost stops for $dt = 0.125$ s and are not present anymore for $dt = 0.1$ s.

(a) $dt = 0.5$ s

(b) $dt = 0.25$ s

**(c)** $dt = 0.2$ s

(d) $dt = 0.125$ s

(e) $dt = 0.1$ s
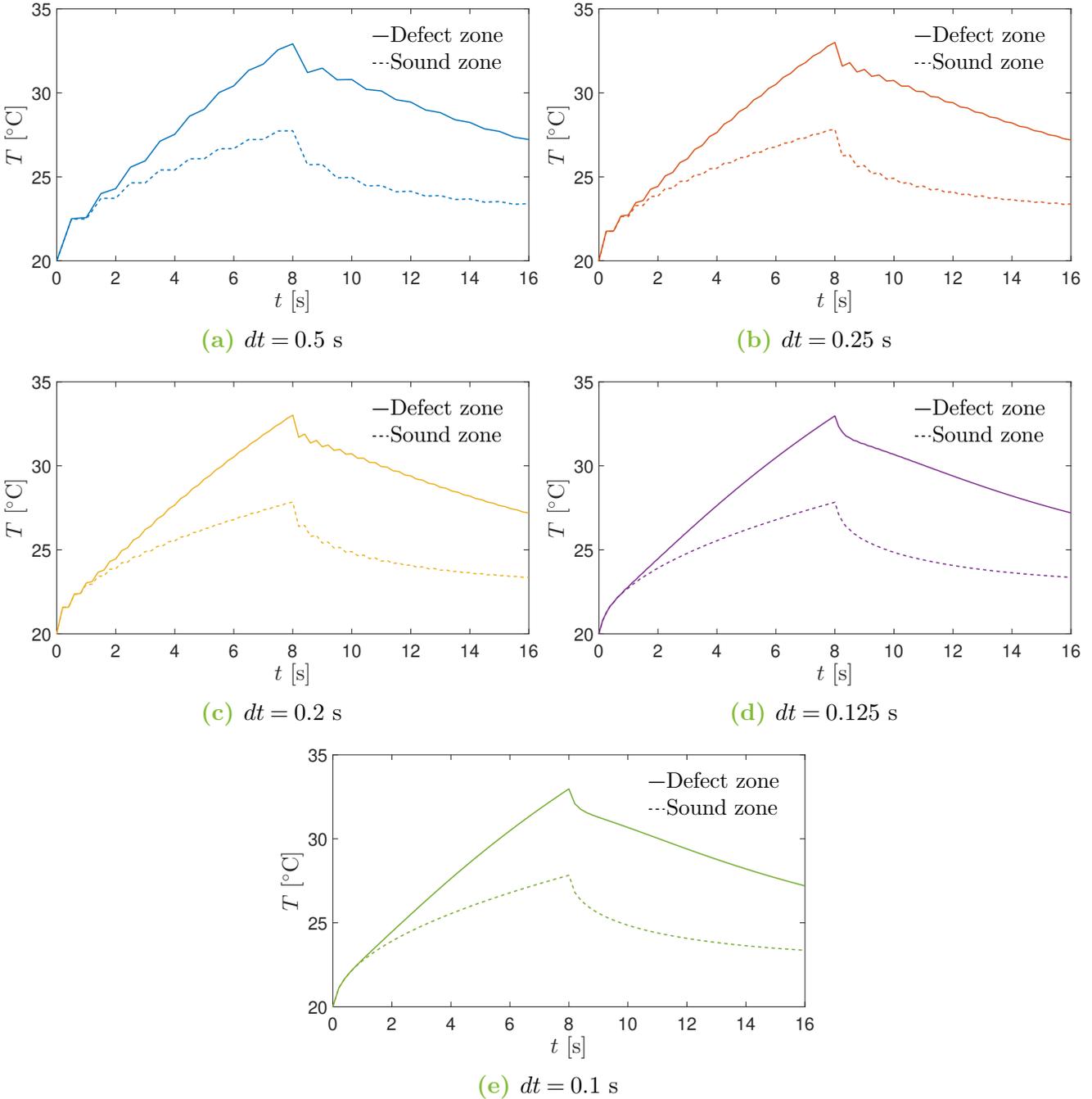
Figure A.1: Time evolution of the temperature computed with different time steps at two points, one above the defect and one in the sound zone. Fixed number of elements.

The effect of both the number of elements and the time step is highlighted in Fig. A.2. The number of elements does not influence the solution much, while the solution slightly changes with the time step. Finally, the time step has to be chosen to have a solution without oscillations.

Figure A.2: Convergence on the number of elements for different timesteps ($dt = 0.25$ is not shown for readability). The reference point is taken above the defect.
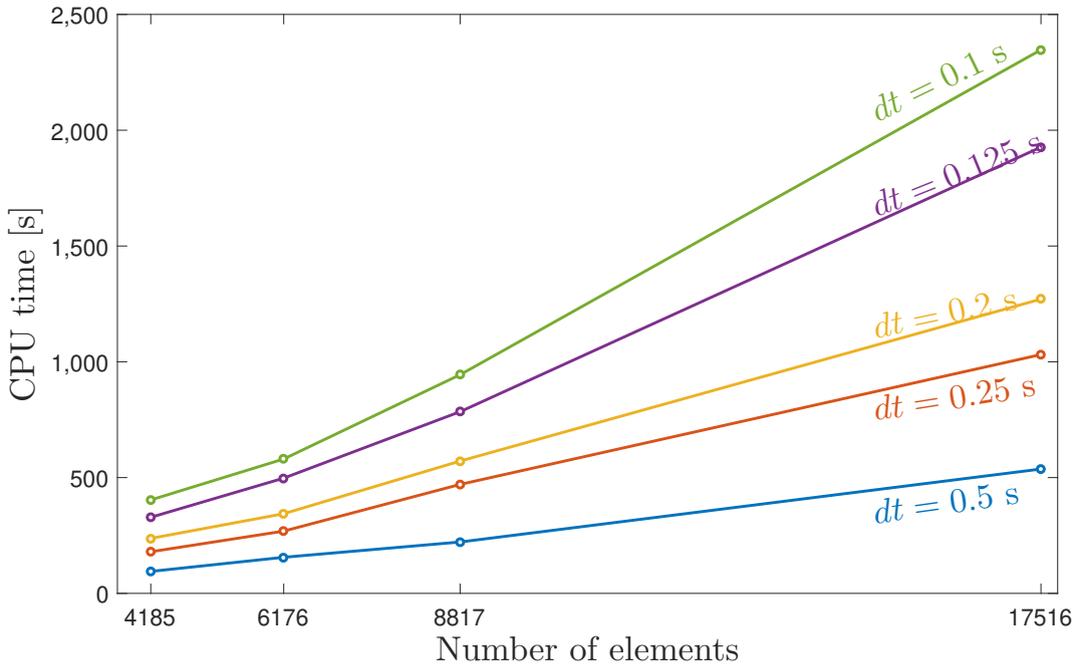
Figure A.3: CPU time needed for the thermal simulations.

A.2.1.1 Oscillation damping solutions

It is well known that Crank-Nicolson scheme may introduce oscillations for sharp initial conditions [39]. It is possible to damp these oscillations by rather reducing the time step as seen in Fig. A.1 or smoothing the initial conditions. The first solution may not be convenient as reducing the time step leads to very large computation time. On the other hand, the second solution is investigated to reduce these oscillations. The initial conditions are smoothed with third order

polynomials functions for the rise, p_1 and fall, p_2 described by

$$
\begin{cases}
p_1 & = -2 \cdot \frac{q_{max}}{t_u^3} \cdot t^3 + 3 \cdot \frac{q_{max}}{t_u^2} \cdot t^2 \\
p_2 & = 2\frac{q_{max}}{t_d^3} \cdot t^3 - 3q_{max}\frac{(t_d+2t_e)}{t_d^3} \cdot t^2 + 6 \cdot q_{max} \cdot t_e \frac{(t_e+t_d)}{t_d^3} \cdot t - q_{max}\frac{\left(2t_e^3 - t_d^3 + 3t_d t_e^2\right)}{t_d^3}
\end{cases}
\tag{A.9}
$$

where t is the variable representing the time, t_u, t_d and t_e are the parameters characterizing respectively the rise time, the fall time and the time at which the fall starts. Finally, q_{max} is the intensity of the step. Fig. A.4 compares the smooth and sharp step setting the rise and fall time to $t_u = t_d = 1$s, stopping the step at 8 seconds, $t_e = 8$s.

Solving the thermal problem imposing the smooth step with a time step of 0.2 s where normally oscillations are present leads to Fig. A.5. It can be seen that oscillations disappear, which shows that sharp initial conditions can lead to spurious solutions.
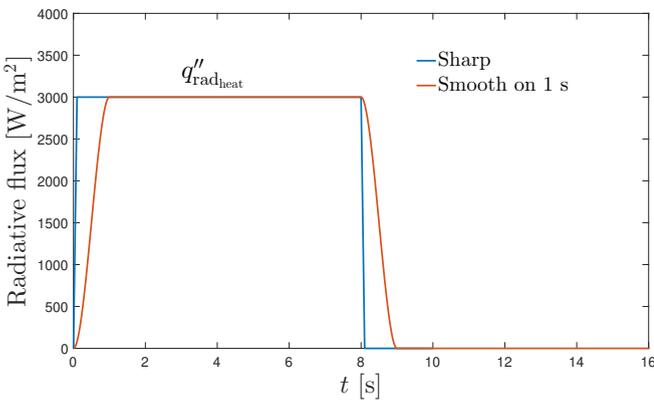
Figure A.4: Sharp and smooth step function for the heat flux.
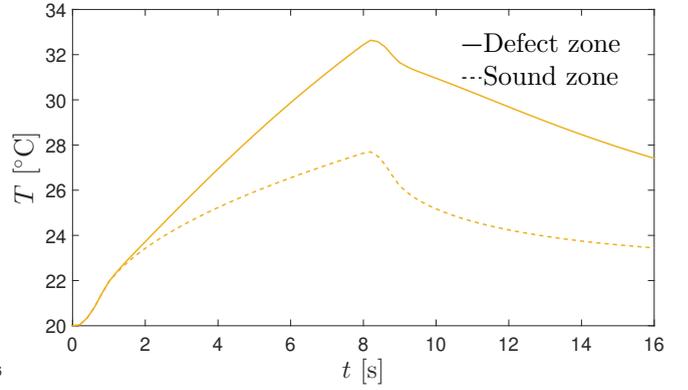
Figure A.5: Temperature time evolution with the smooth step function excitation (see Fig. A.4. $dt = 0.2$ s.

The problem is that in reality, the physics is nearer to the sharp step than the smooth excitation. Therefore another solution is investigated. This solution combines time step reduction and excitation smoothing. The step is smoothed with the same polynomials as in Eq. A.9 but this time with rise and fall time much lower, $t_u = t_d = 0.1$ s, this smoothed function is shown in Fig. A.6. Reducing the time step among all the time domains would be too costly, so it is reduced only around the rise and fall phase of the excitation. The Final solution is given in Fig. A.7 where the different timesteps are explicitly shown.

A.2.2 Mechanic

The mechanic problem is influenced by the temperature field but statically so that the timestep does not impact the mechanic solution. The time history of $d_x w$ at some points of the surface and the impact of the number of elements on the solution is shown in Fig. A.8.

The TPE is also shown as a reference variable for convergence, The TPE evolves with the same
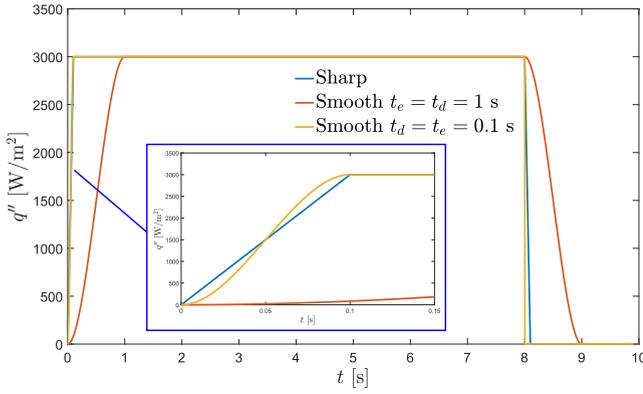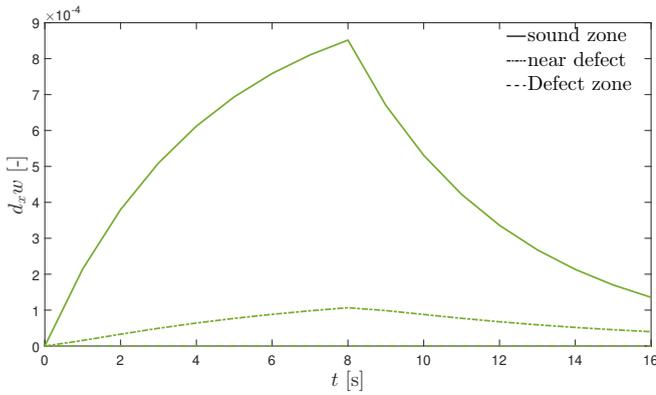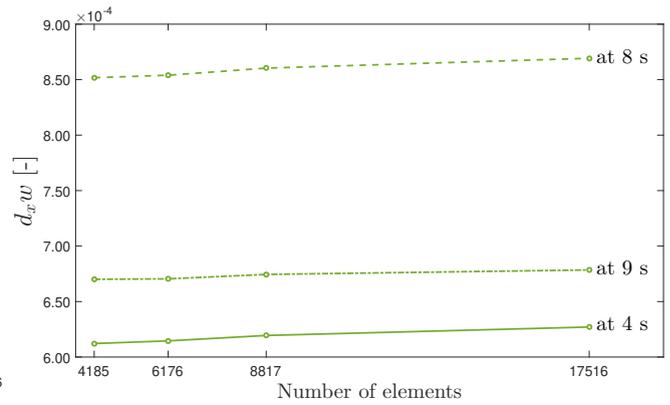
Figure A.6: Sharp shape and smooth shape with different parameters of heat flux excitation.
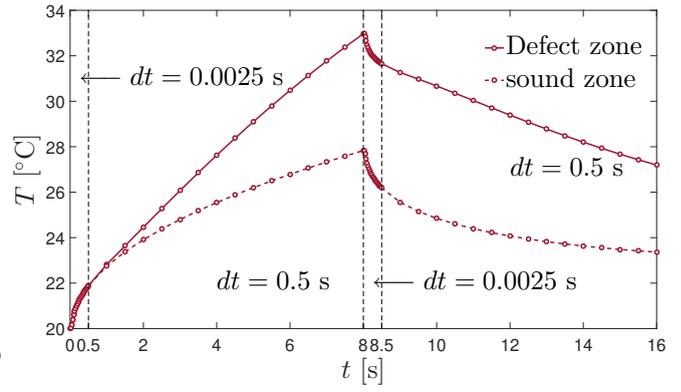
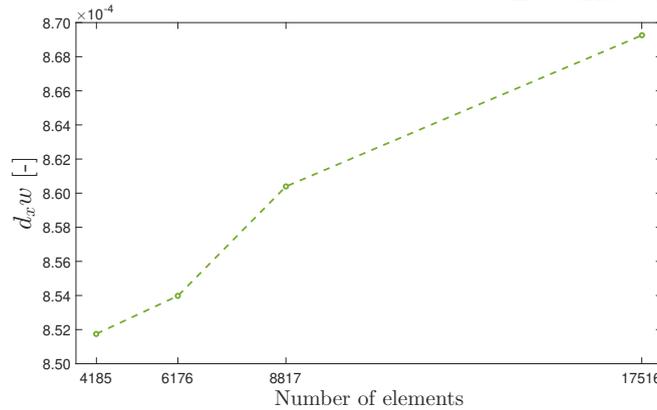**Figure A.7:** Temperature evolution with adaptive timestep and smoother initial conditions (see Fig. A.6 with $t_{\mathrm{u}} = t_{\mathrm{d}} = 0.1$ s).

(a) Time history of out-of-plane displacement derivative. Fixed number of elements.

(b) Number of elements convergence on $d_x w$ at three different time. Reference point taken at the sound surface (see Fig. A.8a).


(c) Zoom on $d_x w$ at 8s.

Figure A.8: Convergence on $d_x w$.

shape as $d_x w$ with time and the impact of the number of elements is shown in Fig. A.9.

The time needed for one iteration of the mechanical problem is depicted in Fig. A.10. Note that the mechanical problem must be solved at different times, so the time for all the iterations is much larger. For instance, if you solved the problem each second until 16 seconds, you need to multiply this time by 17, if you solve it for each half-second by 33, etc.
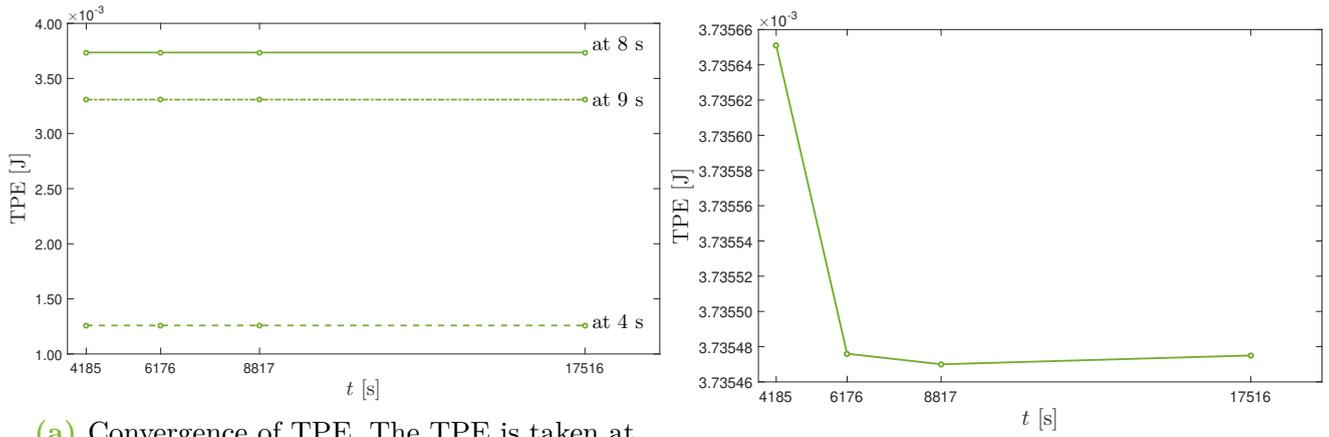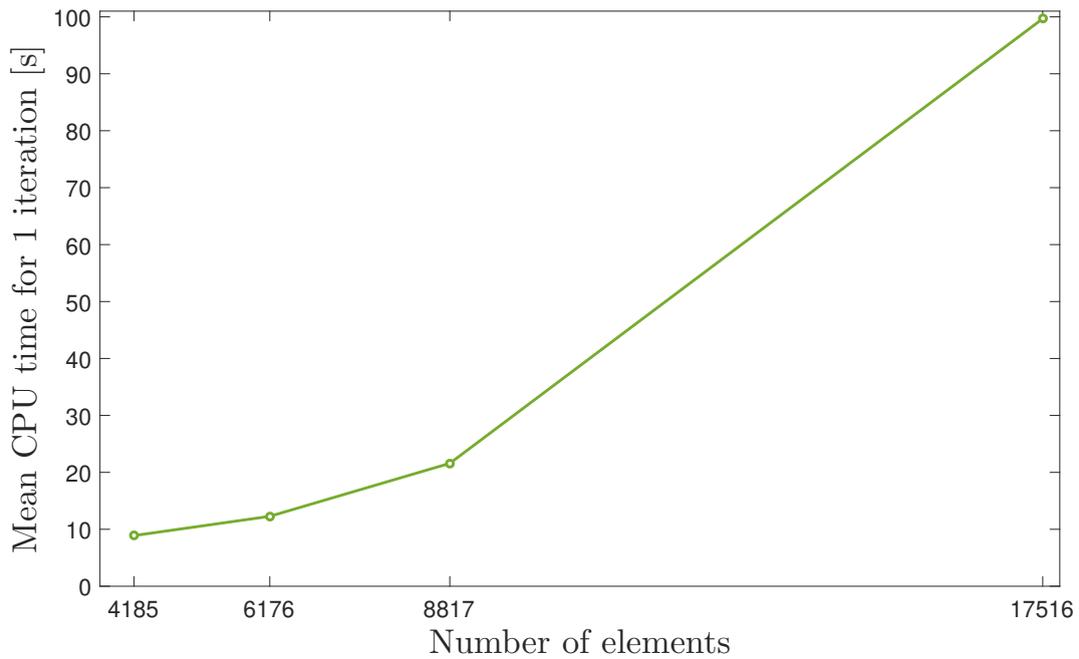
(a) Convergence of TPE. The TPE is taken at different time.

(b) Zoom on TPE at 8 s.

Figure A.9: Convergence of TPE.

Figure A.10: Mean CPU time needed to solve 1 iteration of the mechanical problem.

Bibliography

[1] D. Francis. "Non-destructive evaluation (NDE) of composites: introduction to shearography". In: *Non-Destructive Evaluation (NDE) of Polymer Matrix Composites*. Elsevier, 2013, pp. 56–83. DOI: 10.1533/9780857093554.1.56. URL: https://doi.org/10.1533/9780857093554.1.56.

[2] Y.Y. Hung, L.X. Yang, and Y.H. Huang. "Non-destructive evaluation (NDE) of composites: digital shearography". In: *Non-Destructive Evaluation (NDE) of Polymer Matrix Composites*. Elsevier, 2013, pp. 84–115. DOI: 10.1533/9780857093554.1.84. URL: https://doi.org/10.1533/9780857093554.1.84.

[3] Arthur LISMONDE. "Contrôle non-destructif par shearographie : simulations thermomécaniques de composites à renforts tissés." MA thesis. University of Liege, 2016.

[4] *WP9.2 : Modélisation CND par shearographie sur l'échantillon avec défaut de délamination*. Tech. rep. C.S.L., 2017.

[5] Jean-François VANDENRIJT et al. *Livrable L9.2.D Rapport de corrélation de la modélisation entre simulation et contrôle non destructif*. Tech. rep. C.S.L., 2017.

[6] M.Bruyneel & M.Volvert. *Mechanics of composites*. University of Liege. 2020.

[7] Andrew J. Jefferson, Vellayaraj Arumugam, and Hom Nath Dhakal. "Introduction and context". In: *Repair of Polymer Composites*. Elsevier, 2018, pp. 1–43. DOI: 10.1016/b978-0-08-102263-4.00001-6. URL: https://doi.org/10.1016/b978-0-08-102263-4.00001-6.

[8] Y. Liu, M. de Araujo, and H. Hu. "Advanced fibrous architectures for composites in aerospace engineering". In: *Advanced Composite Materials for Aerospace Engineering*. Elsevier, 2016, pp. 17–58. DOI: 10.1016/b978-0-08-100037-3.00002-x. URL: https://doi.org/10.1016/b978-0-08-100037-3.00002-x.

[9] S. Rana and R. Fangueiro. "Advanced composites in aerospace engineering". In: *Advanced Composite Materials for Aerospace Engineering*. Elsevier, 2016, pp. 1–15. DOI: 10.1016/b978-0-08-100037-3.00001-8. URL: https://doi.org/10.1016/b978-0-08-100037-3.00001-8.

[10] L.Z. Linganiso and R.D. Anandjiwala. "Fibre-reinforced laminates in aerospace engineering". In: *Advanced Composite Materials for Aerospace Engineering*. Elsevier, 2016, pp. 101–127. DOI: 10.1016/b978-0-08-100037-3.00004-3. URL: https://doi.org/10.1016/b978-0-08-100037-3.00004-3.

[11] J.P. Nunes and J.F. Silva. "Sandwiched composites in aerospace engineering". In: *Advanced Composite Materials for Aerospace Engineering*. Elsevier, 2016, pp. 129–174. DOI: 10.1016/b978-0-08-100037-3.00005-5. URL: https://doi.org/10.1016/b978-0-08-100037-3.00005-5.

[12] URL: https://www.fhwa.dot.gov/bridge/pubs/hif18041.pdf (visited on 05/10/2021).

[13] URL: https://www.researchgate.net/publication/267992407_A_meso-FE_voxel_model_of_an_interlock_woven_composite/figures (visited on 05/10/2021).

[14] Peter Sivák et al. "Analysis of Sandwich Structures by the FEM". In: *American Journal of Mechanical Engineering* 5.6 (2017).

[15] K. Senthil et al. "Defects in composite structures: Its effects and prediction methods – A comprehensive review". In: *Composite Structures* 106 (Dec. 2013), pp. 139–149. DOI: 10.1016/j.compstruct.2013.06.008. URL: https://doi.org/10.1016/j.compstruct.2013.06.008.

[16] R. Smith. "COMPOSITE DEFECTS AND THEIR DETECTION". In: 2011. URL: https://www.eolss.net/Sample-Chapters/C05/E6-36-04-03.pdf.

[17] Unni Santhosh et al. "Quantification of Porosity in Ceramic Matrix Composites Using Thermography". In: *Journal of Nondestructive Evaluation* 37.2 (May 2018). DOI: 10.1007/s10921-018-0487-z. URL: https://doi.org/10.1007/s10921-018-0487-z.

[18] D. Balageas et al. "Thermal (IR) and Other NDT Techniques for Improved Material Inspection". In: *Journal of Nondestructive Evaluation* 35.1 (Jan. 2016). DOI: 10.1007/s10921-015-0331-7. URL: https://doi.org/10.1007/s10921-015-0331-7.

[19] Mekhanika Kompozitnykh Materialov. "DELAMINATION BEHAVIOR IN COMPOSITE MATERIALS SUBJECTED TO THERMAL EFFECTS". In: *Plenum Publishing Corporation* 4 (May 1988), pp. 644–655. DOI: 10.1007/s10921-018-0487-z. URL: https://link.springer.com/content/pdf/10.1007%5C%2FBF00608131.pdf.

[20] Fabrice MICHEL. "Développement et première application d'une installation de shearographie." MA thesis. University of Liege, 2004.

[21] W Steinchen et al. "Non-destructive testing of aerospace composite materials using digital shearography". In: *Proceedings of the Institution of Mechanical Engineers, Part G: Journal of Aerospace Engineering* 212.1 (Jan. 1998), pp. 21–30. DOI: 10.1243/0954410981532108. URL: https://doi.org/10.1243/0954410981532108.

[22] Jonathan ROCHET. *Shearography: speckle shearing interferometry. Introduction and technical aspects.* Optrion. 2021.

[23] Y.H. Huang et al. "NDT&E using shearography with impulsive thermal stressing and clustering phase extraction". In: *Optics and Lasers in Engineering* 47.7-8 (July 2009), pp. 774–781. DOI: 10.1016/j.optlaseng.2009.02.011. URL: https://doi.org/10.1016/j.optlaseng.2009.02.011.

[24] Y.Y. Hung and H.P. Ho. "Shearography: An optical measurement technique and applications". In: *Materials Science and Engineering: R: Reports* 49.3 (Apr. 2005), pp. 61–87. DOI: 10.1016/j.mser.2005.04.001. URL: https://doi.org/10.1016/j.mser.2005.04.001.

[25] C. Ibarra-Castanedo et al. "Infrared image processing and data analysis". In: *Infrared Physics & Technology* 46.1-2 (Dec. 2004), pp. 75–83. DOI: 10.1016/j.infrared.2004.03.011. URL: https://doi.org/10.1016/j.infrared.2004.03.011.

[26] C. Ibarra-Castanedo, A. Bendada, and X. Maldague. "Thermographic Image Processing for NDT". In: *IV Conferencia Panamericana de END Buenos Aires* (Oct. 2007). URL: https://www.ndt.net/article/panndt2007/papers/55.pdf.

[27] N Rajic. "Principal component thermography for flaw contrast enhancement and flaw depth characterisation in composite structures". eng. In: *Composite structures* 58.4 (2002), pp. 521–528. ISSN: 0263-8223.

[28] X Maldague, F Galmiche, and A Ziadi. "Advances in pulsed phase thermography". In: *Infrared Physics & Technology* 43.3 (2002), pp. 175–181. ISSN: 1350-4495. DOI: https://doi.org/10.1016/S1350-4495(02)00138-X. URL: https://www.sciencedirect.com/science/article/pii/S135044950200138X.

[29] Richard B. Hetnarski and M. Reza Eslami. "Thermodynamics of Elastic Continuum". In: *Solid Mechanics and Its Applications*. Springer International Publishing, 2019, pp. 45–107. DOI: 10.1007/978-3-030-10436-8_2. URL: https://doi.org/10.1007/978-3-030-10436-8_2.

[30] Djaffar Boussa. "Shearography: An optical measurement technique and applications". In: *Journal of Thermal Stresses, Taylor & Francis, In* (Oct. 2019). URL: https://hal.archives-ouvertes.fr/hal-02332040/document.

[31] Richard B. Hetnarski and M. Reza Eslami. *Thermal Stresses—Advanced Theory and Applications*. Springer International Publishing, 2019. DOI: 10.1007/978-3-030-10436-8. URL: https://doi.org/10.1007/978-3-030-10436-8.

[32] S. M. Alipour, Y. Kiani, and M. R. Eslami. "Rapid heating of FGM rectangular plates". In: *Acta Mechanica* 227.2 (Sept. 2015), pp. 421–436. DOI: 10.1007/s00707-015-1461-9. URL: https://doi.org/10.1007/s00707-015-1461-9.

[33] B. A. BOLEY. "Approximate Analyses of Thermally Induced Vibrations of Beams and Plates1". In: *ASME* (Mar. 1972). URL: http://appliedmechanics.asmedigitalcollection.asme.org.

[34] Seiichi Nomura and A. Haji-Sheikh. *Heat Transfer in Composite Materials*. Nov. 2017. ISBN: 9781605954592.

[35] Frank P. Incropera et al. *Fundamentals of Heat and Mass Transfer*. Vol. sixth edition. International student version. Wiley, 2011.

[36] *A Guide to Calculate Convection Coefficients for Thermal Problems Application Note*. URL: https://www.mikrocontroller.net/attachment/2415/convection_coeff.pdf.

[37] *How to Calculate the Free Convection Coefficient for Vertical or Horizontal Isothermal Planes*. URL: https://www.coursehero.com/file/74689964/Part-6-How-to-Calculate-the-Free-Convection-Coefficientpdf/ (visited on 05/13/2021).

[38] *Simcenter Samcef® 2020.1*. URL: https://docs.plm.automation.siemens.com/data_services/resources/nx/1899/nx_help/custom/en_US/samcef_solver_documentation/index.html.

[39] D. Britz, O. Østerby, and J. Strutwolf. "Damping of Crank–Nicolson error oscillations". In: *Computational Biology and Chemistry* 27.3 (July 2003), pp. 253–263. DOI: 10.1016/s0097-8485(02)00075-x. URL: https://doi.org/10.1016/s0097-8485(02)00075-x.

[40] Viorel ANGHEL et al. "On the use of infrared thermography NDT of aerospace materials". In: *INCAS BULLETIN* 2.3 (2010). Department of Strength of Materials, the "POLITEHNICA" University of Bucharest.

[41] Engineering ToolBox. *Air, Thermophysical Properties*. 2003. URL: https://www.engineeringtoolbox.com/air-properties-d_156.html (visited on 05/24/2021).

[42] Dielectric Manufacturing. *Teflon® Characteristics*. May 2020. URL: https://dielectricmfg.com/knowledge-base/teflon/ (visited on 05/24/2021).

[43] Designer data. *PTFE Polytetrafluoroethylene (Teflon)*. URL: https://designerdata.nl/materials/plastics/thermo-plastics/polytetrafluoroethylene-(teflon)?cookie=YES (visited on 05/24/2021).

[44] Xenics. *Gobi 640 Series*. 2021. URL: https://www.xenics.com/long-wave-infrared-imagers/gobi-640-series/ (visited on 06/21/2021).